UNIVERSIDADE ESTADUAL PAULISTA "JÚLIO DE MESQUITA FILHO"
CAMPUS DE ILHA SOLTEIRA
PROGRAMA DE PÓS GRADUAÇÃO EM ENGENHARIA MECÂNICA

LUCAS RHEA ZANETTI

LUMPED PARAMETER AND MODAL MODELS TO SIMULATE GROUND REACTION FORCES DUE TO RUNNING

Ilha Solteira
2021

UNIVERSIDADE ESTAUAL PAULISTA “JÚLIO DE MESQUITA FILHO”
CAMPUS DE ILHA SOLTEIRA
PROGRAMA DE PÓS GRADUAÇÃO EM ENGENHARIA MECÂNICA

LUCAS RHEA ZANETTI

LUMPED PARAMETER AND MODAL MODELS TO SIMULATE GROUND REACTION FORCES DUE TO RUNNING

Tese apresentada à Faculdade de Engenharia do Campus de Ilha Solteira – UNESP como parte dos requisitos para obtenção do título de Doutor em Engenharia Mecânica. Especialidade: Sistemas dinâmicos e vibrações.

Prof. Dr. Michael John Brennan
Orientador

Ilha Solteira
2021

FICHA CATALOGRÁFICA
Desenvolvido pelo Serviço Técnico de Biblioteca e Documentação

Z28l Zanetti, Lucas Rhea.
Lumped prameter and modal models to simulate ground reaction forces due to running / Lucas Rhea Zanetti. -- Ilha Solteira: [s.n.], 2021
122 f. : il.

Tese (doutorado) - Universidade Estadual Paulista. Faculdade de Engenharia de Ilha Solteira. Área de conhecimento: Automação, 2021

Orientador: Michael Brennan
Inclui bibliografia

1. Forças de reação do solo. 2. Análise modal. 3. Corrida.

Raiane da Silva Santos
Raiane da Silva Santos
Supervisora Técnica de Seção
Seção Técnica de Referência, Atendimento ao usuário e Documentação
Diretoria Técnica de Biblioteca e Documentação
CRB/8 - 9999

Certificado de aprovação

UNIVERSIDADE ESTADUAL PAULISTA

Câmpus de Ilha Solteira

CERTIFICADO DE APROVAÇÃO

TÍTULO DA TESE: Lumped parameter and modal models to simulate ground reaction forces due to running

AUTOR: LUCAS RHEA ZANETTI

ORIENTADOR: MICHAEL JOHN BRENNAN

Aprovado como parte das exigências para obtenção do Título de Doutor em ENGENHARIA MECÂNICA, área: Mecânica dos Sólidos pela Comissão Examinadora:

Prof. Dr. MICHAEL JOHN BRENNAN (Participaçao Virtual)
Departamento de Engenharia Mecânica / Faculdade de Engenharia de Ilha Solteira - UNESP

Prof. Dr. JOAO ANTONIO PEREIRA (Participaçao Virtual)
Departamento de Engenharia Mecânica / Faculdade de Engenharia de Ilha Solteira - UNESP

Prof. Dr. PAULO JOSÉ PAUPITZ GONÇALVES (Participaçao Virtual)
Departamento de Engenharia Mecânica / Faculdade de Engenharia de Bauru - UNESP

Prof. Dr. GIANLUCA GATTI (Participaçao Virtual)
Department of Mechanical, Energy and Management Engineering / University of Calabria

Prof. Dr. JOHANNES PETRUS VERHEUL (Participaçao Virtual)
School of Sport, Exercise and Rehabilitation / University of Birmingham

Ilha Solteira, 27 de janeiro de 2021

To my parents Onilda and Mauricio for all the love and support,
To my brothers Fernando, Bernardo and Arthur

And to my love Glenda.

ACKNOWLEDGENENTS

I feel deeply grateful in being advised by such an amazing human being. I want to thank Dr. Mike Brennan for all the patience, all the advice, all the conversations and all the work done together in these past four years. I have grown personally and professionally under your supervision, and hopefully this is the first of many works done together. You deserve all the praise you get. It was a great pleasure to work with you.

My family deserves a special mention here. I cannot express how much I am grateful for being part of such a great family. My mom, Onilda, made all the effort possible to support me, even from distance. My dad, Mauricio, did everything he could so that I have all the focus needed in the research. My brothers, Bernardo and Fernando, helped me and supported me as well during my entire life and throughout these last years as well. Arthur, my brother, I hope you are proud of me, wherever you are.

Glenda, my love, thank you for being such an amazing partner and woman. Your friendship, your love, were fundamental for me to get to where I am today.

I want to thank all my friends that were especially important in many instances. Your support and friendship made all the difference.

Finally, I want to thank the Mechanical Engineering department at UNESP- Ilha Solteira for helping me through the PhD. I want to extend my acknowledgements to CAPES as well for all the financial support in these past years.

ABSTRACT

Running is an important physical activity in many people’s lives, whether to maintain the body’s health or as a high-performance sport. Because it is a physical activity, running involves the risk of injury. Since the beginning of the 20th century, the mechanisms involved in running and characteristics that may be related to the occurrence of injuries have been studied. One of the main characteristics related to injuries in running is the ground reaction force. In addition to experimental methodologies, mathematical models have been used as an important alternative to simulate ground reaction forces. This thesis seeks to study the ground reaction force during running using and comparing mathematical models, proposing a new lumped parameter model for the simulation of the foot/ground interface, and proposing a new model for the simulation of vertical ground reaction forces. A linear lumped parameter model for the contact between the foot and the ground was proposed and compared with a known non-linear model in the literature. The proposed model was able to closely simulate the behavior of the non-linear model in both soft and hard sole conditions. A general state-space modal analysis procedure was discussed and applied to two lumped parameter models to analyze the presence of dominant modes. The dominant modes were observed, and it was possible to conclude that three modes are sufficient to represent the dynamics involved in the vertical ground reaction forces. Based on the behavior of the dominant modes, a modal model was proposed for the simulation of the vertical ground reaction forces in running. The model was tested using six experimental data sets of vertical ground reaction forces from the literature. The model was able to reproduce the experimental profiles of ground reaction forces with a good precision, although there is some variability in the parameters obtained from the model’s modes in the simulation of each set of experimental data, which makes it a little difficult to physically interpret. each data set.

Keywords: Model. Ground reaction force. Modal analysis. Modes. Degrees-of-freedom.

RESUMO

A corrida é uma atividade física de destaque na vida de muitas pessoas, quer seja como um modo de se manter a saúde do corpo, quer seja como esporte de alto rendimento. Pelo fato de ser uma atividade física, a corrida envolve o risco de ocorrência de lesões. Desde o início do século XX tem se estudado os mecanismos envolvidos durante a corrida e características que possam estar relacionadas à ocorrência de lesões. Uma das principais características relacionadas a lesões durante uma corrida é a força de reação do solo. Além de metodologias experimentais, modelos matemáticos têm sido utilizados como uma alternativa importante para simular as forças de reação do solo. Esta tese busca estudar a força de reação do solo durante uma corrida utilizando e comparando modelos matemáticos, propondo um novo modelo de parâmetros concentrados para a simulação de contato na interface pé/solo e propondo um novo modelo para a simulação das forças verticais de reação do solo. Um modelo linear de parâmetros concentrados para o contato entre o pé e o solo foi proposto e comparado com um conhecido modelo não-linear da literatura. O modelo proposto foi capaz de simular com boa aproximação o comportamento do modelo não-linear em ambas as condições de solado macio e duro. Um procedimento geral de análise modal em espaço de estados foi discutido e aplicado a dois modelos de parâmetros concentrados diferentes a fim de se analisar a presença de modos dominantes. Os modos dominantes foram observados e foi possível concluir que três modos são suficientes para representar a dinâmica envolvida na força vertical de reação do solo. Com base no comportamento dos modos dominantes, um modelo modal foi proposto para a simulação das forças verticais de reação do solo durante a corrida. O modelo foi testado utilizando seis conjuntos de dados experimentais de forças verticais de reação do solo da literatura. O modelo foi capaz de reproduzir bom grau de precisão os perfis experimentais de forças de reação do solo, apesar de haver certa variabilidade nos parâmetros obtidos do modelo para os modos na simulação de cada conjunto de dados experimentais, o que torna um pouco difícil a interpretação física para cada conjunto de dados.

Palavras-chave: Modelo. Força de reação do solo. Análise modal. Modos. Graus de liberdade.

LIST OF FIGURES

LIST OF TABLES

LIST OF ABREVIATIONS

AD	*Anno Domini*
ANN	Artificial Neural Network
AZM	Adapted Zener Model
BC	Before Christ
DOF	Degree-of-freedom
GRF	Ground Reaction Force
LPM	Lumped Parameter Model
MLR	Multiple Linear Regression
NLM	Nigg and Liu’s Model
PDE	Partial Differential Equation
PhD	Philosophy Doctorate Degree
RMSE	Root Mean Square Error

LIST OF SYMBOLS

Roman symbols

$\mathbf{A}$	State-space matrix formed by matrices mass and damping matrices
a	Element of matrix $\mathbf{A}$
$acel$	Acceleration of the mass in the model from Verheul *et al*.
A	Constant formed by φ, q_0, h and υ
A_{cc}	Average contact area of the foot
$\mathbf{B}$	State-space matrix formed by mass and stiffness matrices
b	Element of matrix $\mathbf{B}$
B	Constant formed by φ, h and υ
BM	Body mass
$\mathbf{C}$	Damping matrix
c	Damping coefficient
C	Underdamped mode component constants formed by k_0, k_{01} and A
D	Underdamped mode component constants formed by k_0, k_{01} and A
E	Underdamped mode component constant formed by k_0, k_{01} and B
$\mathbf{f}$	Force vector
$f_{\max}$	Smaller force peak
$f_{\min}$	Force valley after the smaller peak
F	Modal component ground reaction force
F_g	Nonlinear ground reaction force
$F_{\max}$	Main force peak
F_T	Total force
F_{zen}	Ground reaction force in the Zener model
g	Gravity acceleration
G	Underdamped mode component force modulus
GRF	Ground reaction force
$\mathbf{h}$	Vector formed by the force vector after the system's diagonalization
$\mathbf{H}$	Matrix formed by the systems' equations of motion
h	Element of the vector $\mathbf{h}$
i	Mode counter
I	General coefficient in the superposition of the root solutions

j	Complex number ($\sqrt{-1}$)
jj	Physical coordinate counter
J	Impulse
$\mathbf{K}$	Stiffness matrix
k	Spring stiffness
K	Upper body stiffness
l	Spring length
$\mathbf{M}$	Mass matrix
m	Concentrated mass
M	Concentrated upper body mass
n	System of matrix order
N	Time to reach the peak in the bell-shaped impulse curve
O	Peak amplitude in the bell-shaped impulse curve
$\mathbf{p}$	State-space vector formed by the force vector
p , $\dot{p}$	Initial position and velocity of the mass in the model from Verheul *et al*.
P	Overdamped mode component constants formed by k_0 , k_{01} and A
$\mathbf{q}$	Modal coordinate vector
$\mathbf{q}_0$	Initial conditions of the modal coordinate vector
q	Element of the modal coordinates vector
q_0	Initial value of the element of the modal coordinates vector
Q	Half-width time interval in the bell-shaped impulse curve
r	Matrix line number
R	Overdamped mode component constants formed by k_0 , k_{01} and A
s	Matrix column number
S	Overdamped mode component constants formed by k_0 , k_{01} and A
t	Time
t_{aer}	Aerial time
t_{con}	Foot-contact time
t_{step}	Step time
T	Overdamped mode component constants formed by k_0 , k_{01} and A
u	Coefficients of the determinant of matrix $\mathbf{H}$
U	Overdamped mode component constant formed by k_0 , k_{01} and B
v	Velocity

v_{zlimb}	Vertical velocity of the lower limb
V	Upper body mass velocity
$\mathbf{x}, \dot{\mathbf{x}}, \ddot{\mathbf{x}}$	Displacement, velocity and acceleration vectors
$x, \dot{x}, \ddot{x}$	Displacement, velocity and acceleration of the mass
$\mathbf{y}, \dot{\mathbf{y}}$	State vector and its first order derivative
$\mathbf{y}_0$	Initial conditions of the state vector
$y, \dot{y}, \ddot{y}$	Vertical displacement, velocity and acceleration of the mass

Greek symbols

α	Eigenvalue of the system in state-space representation
β	Rate-independent work fraction
γ	Angle of contact
Δ	Variação
ζ	Damping ratio
θ	General system's eigenvalue
$\mathbf{\Lambda}$	Matrix formed by the diagonalization of $\mathbf{A}$
λ	Element of the diagonalized matrix $\mathbf{\Lambda}$
$\mathbf{\Upsilon}$	Matrix formed by the diagonalization of $\mathbf{B}$
υ	Element of the diagonalized matrix $\mathbf{\Upsilon}$
$\boldsymbol{\varphi}$	Eigenvector relative to the system in state-space representation
$\mathbf{\Phi}$	Modal matrix
$\mathbf{\Phi}_d$	Damped modal matrix
ϕ	Underdamped mode component phase
φ	Element of the state-space system's eigenvector
$\mathbf{\Psi}$	General system's eigenvector
ω	Damped natural frequency
ω_n	Natural frequency

List of subscripts

$3D$	Refers to the proposed three-degree-of-freedom model
$5D$	Refers to the proposed five-degree-of-freedom model

A	Refers to Alexander's model
AVG	Refers to average
$b1$	Refers to Blickhan's one-degree-of-freedom model
$b2$	Refers to Blickhan's two-degree-of-freedom model
CL	Refers to the model from Clark *et al*.
E	Refers t the model from Verheul *et al*.
gen	Refers to general
m	Refers to the modal model
N	Refers to the model from Nigg and Liu
sh	Refer to shoe

List of superscripts

$\mathrm{mod}1$	Refers to the first mode
$\mathrm{mod}2$	Refers to the second mode
$\mathrm{mod}3$	Refers to the third mode
ovd	Refers to the overdamped mode(s)

SUMMARY

1 INTRODUCTION

1.1. Historical Background

The understanding of mathematical modeling is important for a better comprehension of the work described in this thesis. Mathematical modeling is a very wide field and is related to all science areas, but specially in engineering and natural sciences (Medicine, Fluid Mechanics, Chemistry, Computer Science, Economics, etc.). The word ‘model’ comes from the vulgar Latin word *modellus*, which derives from the Latin word *modulus*, that can be defined as an object that serves as a parameter for the construction or creation of other objects (Japiassú and Marcondes, 2001). Models have been used since ancient times. Kallrath (2004) provides a brief historical background of mathematical models. According to his work, the first known use of models is dated from around 30,000 BC, through “counting” and writing numbers on bones. As time went by, civilizations like India, Egypt and Babylon acquired decent knowledge of mathematics and models to improve their peoples’ lives. The first documented use of mathematical theory dates from around 600 BC, when Thales of Miletus started using geometry to analyze reality and helping the development of mathematics. Pythagoras is considered to be the first pure mathematician, developing the theory of numbers and starting the use of proofs for already known theorems. Diophamus of Alexandria contributed to the development of modern models around 250 AD, when he developed the first ideas of algebra and the notion of variable. Building models to represent real problems from reality became a tendency for many eastern civilizations (India, China, Persia and some other Islamic countries). In the western world, mathematics and mathematical models came only around the 11th century, through surveying at first. Leonardo Fibonacci was a great mathematician from that time, using algebraic methods for merchandising. In later centuries more mathematical theories and models were developed, also being used in economics, physics and other science fields.

One of the aspects of mathematical modeling is modeling real world phenomena. For this purpose, differential equations have been fundamental. By definition, a differential equation is an equation that contains the derivatives of one or more dependent variables with respect to one or more independent variables (ZILL, 2009). A derivative is a fundamental property in mathematics. The derivative is defined as the instantaneous rate of change of a function with respect to an independent variable (NARAYAN, 1953). The derivative of a function can be also geometrically interpreted as the tangent of the function in a determined point with respect to the independent variable.

The following historical references concerning differential equations are presented in Archibald *et al*. (2005). The differential calculus emerged around 1700 AD, through the study of the so-called "Inverse tangent problems". The tangent of a given curve in determined points was a problem of classical mathematics, but to find curves that have a specific tangent property was a newer mathematical problem, called the inverse tangent problem. Translating this problem into a correct mathematical formulation gradually gave birth to differential equations in late 17th century. In 1752, Vincenzo Riccati published a paper in Latin called *De usu motus tractorii in constructione aequationum differentialium* (which means "the use of traction motion for differential equations construction"), demonstrating that any differential equation could be integrated in an exact way, using tractional motion. It is allegedly the only complete theoretical work about the use of tractional motion in geometry. At this point, Jean Le Rond d'Alembert had already studied a problem involving multiple pendulums, in which he obtains a system of linear second order differential equations with constant homogeneous multipliers that represents the equations of motion of the pendulum system (in 1743). Later, in a series of three memoirs (1745, 1747 and 1752) d'Alembert proposed a theory for the integration of a system of linear differential equations with constant coefficients, homogeneous or not. Using d'Alembert's studies as a reference, Augustin-Louis Cauchy extended d'Alembert's approach to nonlinear systems (around 1818) and also proposed what is called the classical theory of general differential equations, in which he demonstrates the solution of any 1st order differential equations and the solution for *n*-th order differential equations (the latter by reduction to a system of 1st order differential equations). Around the early1800s, the mathematicians' notion of functions was insufficient to comprehend the integration of higher transcendental functions, and Carl Friedrich Gauss defined a hypergeometric function as the limit of the partial sums of the hypergeometric series, also proposing that the convergence should be a preliminary condition when using a series. In the first half of the 19th century, Carl Gustav Jakob Jacobi and Willian Rowan Hamilton dedicated their efforts in using transformation of variables to find the solutions of differential equations. Their theorems served as a base for the work of mathematicians like Henri Poincaré and Rodolhpe Radau. In 1877, by analyzing Hermann von Helmholtz resonators, Lord Rayleigh, in his work *The Theory of Sound*, deduced Lagrange's equation for general coordinates and added a dissipation function *F*. Around the same time, Marius Sophus Lie observed, by studying tetrahedral line complexes, that their first order partial differential equation (PDE) can be transformed to a smaller PDE that could be integrated directly. Continuing his studies, Lie had big influence over the knowledge of transformations for ordinary and partial differential equations solutions. In 1915, Albert Einstein published his gravitational field equations of general relativity, which represent a generalization of the Poisson equation of Newtonian's mechanics. Einstein's search for reliable field equations persisted for a couple of years, with the inclusion of the called distant parallelism and the introduction of the tetrad field. In 1911 and 1912, Luitzen Egbertus Jan Brouwer proposed two theorems regarding continuous mappings between manifolds of the same dimension. The French mathematician Jacques-Louis Lions carried out some studies related to ordinary differential equations for control theory and applied it to industrial problems in the second half of the 20th century. In 1970, The French physicist David Ruelle and the Dutch mathematician Floris Takens published an article using dissipative differential equations to describe fluids with a very good precision, instead of the classical fluid equation proposed by Claude Louis Navier and George Gabriel Stokes. The historical facts described above do not include all the important differential equation references but are intended to give a brief historical background.

The focus of this thesis is the mathematical modelling of a runner to predict the ground reaction force (GRF) when the runner's foot is in contact with the ground. A schematic drawing of an example of ground reaction force for a runner whose rear part of the foot impacts the first (a rearfoot runner) is shown in Fig. 1.

Figure 1 - Schematic diagram showing a typical ground reaction force for rearfoot runner.

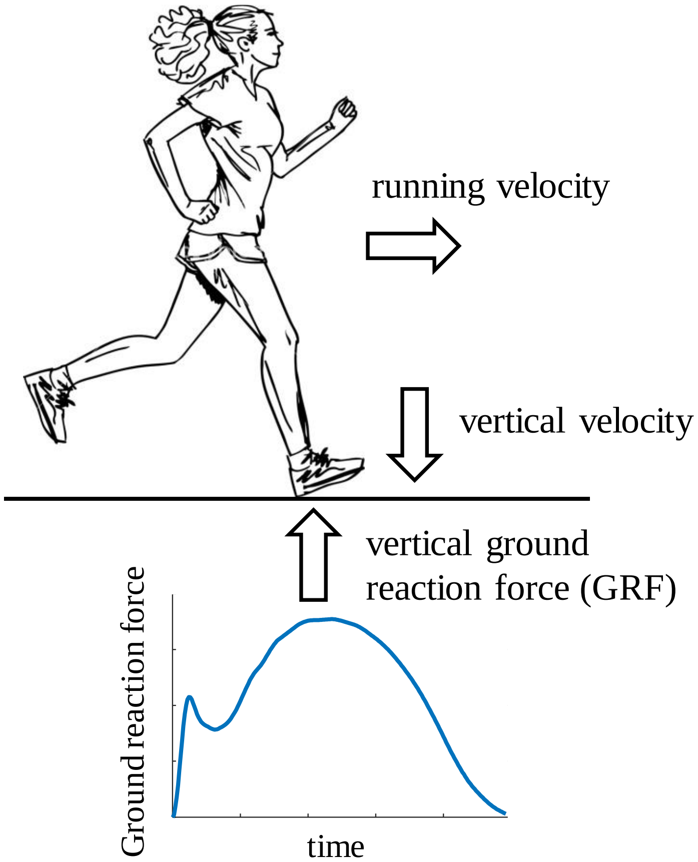

Source: elaborated by the author.

The interest in analyzing the forces related to the foot contact with the ground started in the 19th century. According to Sutherland (2005), the first researcher to investigate experimentally some kind of foot pressure was Carlet (1872). Carlet performed a gait analysis in human locomotion, in which a qualitative measure of foot force in walking was obtained using air reservoirs. Following Carlet, Beely (1882) used a different technique for foot pressure analysis, in which a thin bag with plaster was used to obtain a foot impression. This experiment was performed to test the assumption that parts of the foot bearing the most weight would lead to deepest impressions on the plaster sack. Elftman (1937) presents a brief historical background related to the experiments realized after Beely. Momburg (1908) did an experiment similar to the one carried out by Beely, using moistened garden soil instead of a plaster sack. More accurate methods were developed as time went by. Abrahamson used the same idea in an experiment in 1926 but used steel shot on a hard surface with a plate over the shoot. The subjects were asked to step on the plate and the depth of the shot on the plate was related to the weight supported by various parts of the foot. In 1925, Forstell put a wire net over an ink pad, with a paper foil over the net. The subjects were asked to stand on the paper over the net, and due to elastic properties of the net, the parts of the foot bearing larger weight caused the paper to have greater contact with the ink pad in those regions. Basler, in 1927, built a machine similar to a harp, with 10 strings, on which the subjects were asked to stand on. The strings were then plucked, and the pitch of the strings was compared with the pitch of piano strings, to have a measure of the weight of each of the foot parts. Morton was the first researcher to use rubber for foot pressure analysis. In his experiment, he used a rubber mat with longitudinal ridges placed on an inked ribbon and paper. When the subjects stood in his experiment, the ridges widened due to the elasticity of the rubber and the measure of the weight was related to how wide the impressions on the paper were. However, he mentioned that the experiments failed to analyze the change in the pressure dur to various parts of the foot over time, which is an important characteristic for understanding the physiology of the foot. With that in mind, Elftman (1937) proposed an experiment in which the momentary pressure distribution of the foot in normal progression could be studied. In his experiment, he put a heavy glass plate in a suspended frame between two tables. A rubber mat was put over the glass plate. The upper surface of the rubber mat was smooth, and the lower was studded with pyramidal projections. The apex of each pyramid was in contact with the glass and a white fluid was put between the rubber pyramid projections. As the subjects walked over the mat, the pyramid areas in contact with the glass increased proportionally the pressure from each part of the foot. After Elftman, other authors investigated ground reaction forces during walking, managing to gather experimental data, with the improvement of measurement systems and data collection (for example, accelerometers and force plates helped a lot in the capture of ground reaction force data in running and walking). Cunningham (1950) managed to successfully gather experimental ground reaction force data from subjects walking, and his data was used in several later works in the analysis of ground reaction forces due to walking. Andriachi *et al*. (1977) obtained and compared experimental walking ground reaction force data from normal subjects and subjects with knee pathologies. Yamashita and Katoh (1976) used a specially designed force plate do gather experimental vertical ground reaction force data from normal subjects when walking. Ground reaction force analysis due to walking is still being investigated for different situations up to the present. For example, Barela *et al*. (2014) studied the walking ground reaction force from normal subjects using body weight support. Shahabpoor and Pavic (2018) used a cost-effective method for analyzing the walking ground reaction force, through a single inertial measurement unit.

As to the analysis of running ground reaction forces, according to Cavanagh and La Fortune (1980), Amar (1916) was the first to obtain some form of running ground reaction force measurements, using an apparatus in which rubber bulbs were compressed due to the movement of a platform and its impressions were recorded on a drum by tambours with air transmission. This experiment uses the first ever force plate. By putting a runner to run behind a white wooden lattice work, Fenn (1930a), in the first part of his work, measured the work expended during acceleration and deceleration of the limbs using a moving picture method. In the second part of his work, Fenn (1930b) used a simple model to estimate the body center of mass and investigated the movement of the center of mass due to limb movements, using moving frames. Fenn (1930b) also recorded measurements of the pressure of the foot against the ground when the running velocity was changing, using a system similar to the one used by Amar. Cavagna (1964) used two different measurement systems to study the mechanical work involved in running. One method used accelerometers attached to the trunk and the second method used the moving frames method. As time went by, studies of running ground reaction forces gained more attention by the science community, and more studies were performed. Dickinson *et al*. (1985) studied the shock wave propagation on the impact of the foot in running using a treadmill and a force plate. De Wit *et al*. (1999) performed a biomechanical analysis of the stance phase from subjects in barefoot and shod conditions, at different velocities, using a force plate and a level treadmill. More recently, three-dimensional motion capture systems became an alternative for ground reaction force and kinetic analysis during running and walking, despite being a costly alternative. Hamill *et al*. (2014) used a three-dimensional motion capture system and a force plate to investigate the change in knee and ankle stiffness when running with different footfall patterns (rearfoot and forefoot running). Wojtusch and von Stryk (2015) used a more complex system to capture the motion and the forces in running, using markers for motion capture and two force plates with a treadmill. Gurchiek *et al*. (2017) managed to successfully measure three-dimensional running ground reaction forces when performing change in acceleration and direction experiments using a single inertial measurement unit. Leporace *et al*. (2018) used multilayer perceptron (MLP) neural networks to gather experimental data from running using force platforms and tri-axial accelerometers and simulated ground reaction forces in three directions.

Several different experimental studies of ground reaction forces due to running and walking concluded that the ground reaction forces were somehow linked to the possibility of injuries, and the interest in studying these ground reaction forces increased. At some point, with the knowledge of models and the possibility of avoiding complex experiments in controlled environments, researchers started testing models to simulate the ground reaction forces due to running and walking. Even though the human body is a complex system involving muscles, bones and other viscoelastic materials, the possibility of human body modelling with approximations was an alternative to investigating its main characteristics in different situations. Due to their simplicity, LPMs were the first ones to be implemented as human body and animal body models for dynamic and kinetic studies. In these models, the ground reaction force could be predicted from the motion of a LPM consisting of masses, springs and dampers that represents the human body. One of the first body models reported in the literature was the one described by Greene and McMahon (1979), in which a man standing on roughhewn spruce boards over a wooden beam was modelled as a two-mass lumped parameter system with springs and a damper, to study vibration. A two-mass lumped parameter system with two dampers and two springs was used by Mizrahi and Susak (1982) to model the body for the purpose of studying the transmission of the impact from the foot to the level of the greater trochanter (part of the femur). A simpler LPM was used by McMahon *et al*. (1987). They attached a single mass to a single spring, in which the mass represented the human body mass, and the spring represented the effective vertical stiffness of the body. In a comprehensive study, Cole (1995) presented several different properties of the lower extremity joints during impacts in running, including general models for muscle-tendon and bone units and a nonlinear ground contact model equation for vertical force simulation on impact. Making use of Cole's nonlinear ground contact relation, Nigg and Liu (1999) proposed a more elaborate LPM that included four masses connected through several springs and damper elements. His model was one of the first to model the vertical ground reaction force in the first half of the impact phase with reasonable accuracy. The model proposed by Nigg and Liu is a key paper in ground reaction force modelling and has been cited by many authors. Klute and Berge (2004) studied the gait from an amputee and proposed a slightly different five-mass LPM to simulate the ground reaction force, using Cole's ground contact model. Ly *et al*. (2010) also used the model proposed by Nigg and Liu, but also included a mass to represent the rigid shoe mass connected to the foot mass through a spring and a damper, also using a spring connecting the rigid shoe mass to the ground, representing the ground stiffness.

In the last two decades, different types of models have been mainly developed to simulate specifically the ground reaction forces due to running or walking. One of them is the model proposed by Clark *et al*. (2014), in which the human body is divided into two main masses, one being related to the leg in contact with the ground during impact and the other being the mass of the rest of the body. The total vertical ground reaction force due to running was then composed of the sum of the impulses of each mass on impact with the ground during time in which the foot is in contact with the ground. Wojtusch and von Stryk (2015) developed a forward kinematic model of the human body with thirteen body segments, twelve joints and twenty-eight degrees of freedom, to capture the motion of the body when running.

1.2. Literature Review

The historical background presented a historical evolution of the fields related to mathematical modelling, differential equations, and ground reaction force studies. In this section, the literature review focuses on the literature regarding GRF analysis, which is the central theme of this thesis. The literature review is divided into two main categories: Experimental GRF analysis and analytical GRF analysis. The experimental GRF analysis sub-section discusses important studies concerning experimental GRF data extraction, while the analytical GRF analysis sub-section discusses studies concerning GRF modelling techniques for GRF simulation.

1.2.1. Experimental GRF analysis

Experimental GRF analysis consists of using experimental apparatus to obtain some type of measure of the ground reaction forces or foot pressure. The experimental GRF analysis can be divided into three main subgroups: qualitative GRF and foot pressure analysis, GRF analysis and foot pressure distribution analysis. These concepts, involving each group, are discussed in the following subsections with the presentation of related studies.

1.2.1.1. Qualitative GRF and foot pressure analysis

In late 19th century, when the first attempts to understand the foot force and foot pressure were performed, there were no advanced technologies regarding experimental data extraction, so researchers used methods available at the time to perform these types of studies. Experiments analyzing foot impressions in different apparatus were the first attempts to study foot pressure or foot force. As mentioned in the historical background, Carlet (1872) was the first to attempt GRF investigation, using air reservoirs for human gait analysis, which led to a qualitative foot force profile. Beely (1882) introduced a different form of qualitative foot pressure analysis, in which a subject stood still over a thin plaster bag, and the foot impression in the bag was related to the foot pressure. Fischer (1907) was important to present a new method in analyzing kinematics and forces in running, which consists in using cameras and moving frames. In his work, a man was totally dressed in black clothes, with a series of Geissler tubes arranged symmetrically on his head and limbs. These tubes were then joined to the secondary of a Ruhmkorff coil whereas the primary was interrupted twenty-five times a second. The clothed man ran, and his movement was recorded photographically by cameras all around him and coordinated through networks of squares photographed at the same time. This was three-dimensional running movement analysis, despite still gathering only qualitative data with respect to ground reaction forces and foot pressure. Using the pneumatic principle from Carlet's work, Amar (1916) built an apparatus in which rubber bulbs were compressed due to movement in a platform and the bulb impressions were recorded by tambours with air transmission. Fenn (1930b) used the ideas from Fischer and Amar, to perform analysis of kinematics and foot pressure changes due to running. Elftman (1937) also had an important influence in GRF study due to his experiment, that consisted in generating partial foot impressions in small rubber pyramids. Although the impressions had only qualitative information, this experiment was the first mechanical force plate created.

1.2.1.2. GRF analysis

With the advance of technology (electronical force plates, accelerometers, sensors in general, etc) it became easier to gather qualitative information regarding running and walking, with respect to foot pressure and ground reaction forces. Since the ground reaction forces are related to injuries (NIGG and LIU, 1999; SATO *et al*., 2005; ZADPOOR *et al*., 2007; BATES *et al*., 2013; KHAJAH and HOU, 2015; VAN DER WOOP *et al*., 2015), many studies and experiments were developed in order to gather running and walking GRF data. The first methods to obtain quantitative GRF measurements involved attaching transducers to different regions of the foot. Bauman and Brand (1963) attached transducers to the great toe, 1^{st} metatarsal, 2^{nd} metatarsal, 5^{th} metatarsal and heel, observing pressure recordings through a preamplifier. Later works were able to make use of force plates, which can measure force directly using load cells. These force plates became standard for ground reaction force measurements. Yamashita and Katoh (1976) used a triangular shaped force plate with load cells in each of the three vertices to analyze vertical resultant force during level walking.

Another work using force plates was developed by Bryant *et al*. (1987), in which the ground reaction forces of galloping dogs were analyzed using two-sided force plates. De Wit *et al*. (1999) used a force plate to gather three-dimensional ground reaction force data from nine male runners, running at 3.5, 4.5 and 5.5 m/s to compare biomechanical aspects of shod and barefoot running. Many more similar studies using force plates to gather GRF data were developed in recent times (DUTTO and SMITH, 2002; SATO *et al*., 2005; STILES and DIXON, 2006; STERZING *et al*., 2013; MEURISSE *et al*., 2015; FLUIT *et al*. 2015; SINCLAIR *et al*., 2015; UDOFA *et al*. 2016).

1.2.1.3. Foot pressure distribution analysis

As mentioned previously, running or walking GRFs show important information related to injuries. However, researchers found out that GRF measurements do not give much information regarding force or pressure distribution on the foot-ground interface. The first study to give a quantitative measure of foot pressure distribution was from Arcan and Brull (1976). They developed and patented a complex apparatus consisting of a platform with several layers, an imaging system, and a loading device. When a subject stood on the platform using loading sandals, an image pattern of the foot-ground contact interface was generated. The contrast images displayed different point of pressure under the foot. These images could then be converted into numerical results. Following on from Arcan and Brull, more studies were developed focusing on foot pressure distribution. Manley and Solomon (1979) used a force plate coupled with a signal processing system to study the one-dimensional discrete vertical ground reaction force distribution of a human foot during locomotion. Their work was one of the first to give quantitative measures of the vertical ground reaction force distribution on the foot sole during contact. In a recent study, Castro *et al*. (2015) analyzed the foot plantar pressure distribution in subjects during low and high gait cadences, considering load carriage. The foot plantar region was divided into ten two-dimensional subregions and the plantar pressure of each region was obtained via force plate and then analyzed for loaded and unloaded conditions. Results showed that the foot plantar pressure changes quite significantly in both directions.

1.2.2. Analytical GRF analysis

Running and walking GRF modelling is another option for GRF analysis. It consists of developing a mathematical model that can simulate the running and walking GRF. These models became a viable alternative for GRF analysis due to some disadvantages of experimental GRF analysis. The main disadvantages are a) some quantities are difficult to be measured; b) isolated effects of parameters cannot be studied; c) experimental setups are expensive and must be built in controlled environments (Nikooyan and Zadpoor, 2011).

In this thesis, the focus is on GRF modelling, with comparisons between some models presented in the literature and the development of a new GRF model. Therefore, many works related to GRF modelling are presented in this section. The GRF modelling area can be divided into two main groups: LPMs and other models.

1.2.2.1. Lumped parameters models

The most frequently used model to simulate running and walking GRFs is the lumped parameter model (LPM) (also called the mass-spring-damper model). This model is used to simulate the whole body and the contact of the foot with the ground during locomotion. Despite the complexity of the human body, during the contact of the foot with the ground (stance phase) the dynamics of the body can be separated into portions through each mass in the model. The springs and dampers are used to represent the rigid and viscoelastic parts of the body. The models may include only vertical motion or vertical with horizontal motion. Some of the important works including running and walking GRF modelling through LPMs are presented in this section.

One of the first works to use LPM to measure and simulate impact forces was carried out by Greene and McMahon (1979). The authors used a LPM with two degrees of freedom (DOF) to simulate a subject doing knee-bends while carrying extra weights and carried out the simulation of its vibration considering the two modes of vibration (labelled in this case parallel and anti-parallel modes). Despite using the model to simulate impact forces of a subject standing still, the human body was successfully modelled using a LPM and so researchers started using it for running and walking analysis.

Following the modelling approach by Greene and McMahon, Mizrahi and Susak (1982) assembled a slightly different two-DOF LPM to analyze the impact forces at the greater trochanter level during a jump. Acceleration data was collected during a jump using an accelerometer attached to the great trochanter position of the subject. The model divided the body into two mass portions, one with respect to the region between the foot to the accelerometer level and other with respect to the rest of the body. The model simulation was then validated by comparing the acceleration gathered from the accelerometer and the acceleration of the model mass corresponding to the leg. The output from the model matched reasonably well with the acceleration obtained with the accelerometer.

Blickhan (1989) was the first work to use a one-DOF LPM to simulate running and hopping. In his work, Blickhan separated the movements of running and hopping into two phases: contact phase and aerial phase. In the contact phase, there is the presence of the ground reaction force. For hopping simulations there are two configurations in the work: hopping at zero speed and hopping at nonzero speed. For the first case, the mass only has vertical movement, and the ground reaction force can be calculated as the force through the spring in the contact phase. For hopping at nonzero speed, during the contact phase there is an angle of contact with the ground (with respect to the spring) and horizontal ground reaction force appears. The hopping at nonzero speed analysis is then extended for running.

In a wider study, McMahon and Cheng (1990) used a one-DOF LPM (single mass attached to a spring) to simulate ground reaction forces during running and during hopping. For hopping, only vertical motion is considered in the model. For the running condition, new parameters are included in the simulation. The simulations for both cases showed that the equivalent stiffness of the body changes when considering horizontal velocity (running) and that this stiffness is a function of horizontal and vertical velocities.

Another important work using one-DOF LPMs for impact force analysis in locomotion was performed by Alexander (1990). In his work, it was shown that the energy spent in legged locomotion from robots and animals can be smaller by making use of two features: the pogo stick principle and the return springs. According to the author, the pogo stick principle consists in applying a force to the ground that is in the same direction of the foot contact during contact time length. The work shows that using the pogo stick principle and a return spring attached to the body mass model increases energy saving during locomotion. The author also presents a two-DOF LPM separating the foot mass from the body mass in locomotion movement, showing that the inclusion of a foot pad (represented by a damper) can prevent an effect called “chatter” (vibrations in which the foot repeatedly leaves and returns to the ground before settling during the contact time). In this model, the ground reaction force is the combination of forces of the lower spring and damper in contact with the ground.

Cole (1995) performed an extensive study in his thesis, entitled “Loading of the Joints of the Lower Extremities During the Impact Phase in Running”. In this work, Cole developed models to represent the body, the muscles, the bones, and the involved forces during heel-strike running. One of the important parts of the work is the development of nonlinear ground reaction forces (vertical and horizontal) in discrete points of the foot-ground contact interface. The vertical GRF relation developed by Cole is a nonlinear force that depends on both displacement and velocity of the foot. This relation has been used by different authors in works in subsequent studies.

One of the most important studies regarding LPMs to simulate running ground reaction forces was developed by Nigg and Liu (1999). They proposed a four-DOF LPM and used the concepts of wobbling masses, which corresponds to the mass of the soft parts that shifts relative to the bony parts of the body during the movement (Gruber *et al*., 1998). The model consists in four masses (two wobbling and two rigid) representing the upper and lower portion of the body. The model has only vertical movement, and the ground reaction force is calculated using Cole's nonlinear model, considering hard and soft sole conditions. This model was the first to simulate reasonably well the transition between the first and second peaks in the vertical ground reaction force curve for rearfoot runners.

In a later study, Zadpoor *et al*. (2007) used a slightly different version of the four-DOF LPM proposed by Nigg and Liu, including the nonlinear ground contact relation proposed by Cole. The simulation of the vertical ground reaction force considered again hard and soft sole conditions. The model parameters were changing, to investigate the effect of each model parameter on the total GRF.

Ly *et al*. (2010) also used the basic model proposed by Nigg and Liu but included an extra mass element to represent the foot specifically and the connection to the ground. The difference between the models is that in the model proposed by Nigg and Liu the foot and ground properties are modelled together. In the model proposed Ly *et al*., the additional rigid mass representing the foot is connected to the lower body mass through a spring and a damper, while also being connected to the ground through a spring representing the ground stiffness. With this model, it was possible to analyze how the ground stiffness and shoe stiffness separately affects vertical ground reaction force in running.

Yukawa *et al*. (2011) proposed a complex four-DOF LPM to simulate the vertical and horizontal running GRF at steady running speed. The model included three masses connected through springs and dampers and with vertical motion while all of them rotating with the same angular movement. The model also includes rotational springs and dampers. A parameter search was used to find the best parameters values to match vertical and horizontal running ground reaction force data from runners at steady speed.

In one of the most recent works in the area, Verheul *et al*. (2019) used a two-DOF LPM to test the possibility of it modelling vertical ground reaction forces for different high-intensity tasks. The model proposed by Verheul *et al*. is slightly different from the two-DOF model proposed by Mizrahi and Susak (1982) and similar to the model proposed by Derrick *et al*. (2000), with only one damper and two springs, connecting the two masses and the ground. The work showed that the model could predict different experimental ground reaction forces reasonably well in general but could not predict the well the transition between impact and active peaks.

1.2.2.2. Other models

In the last two decades, new modelling techniques and new methods of parameter identification have been adopted for reaction force modelling for running and walking ground. Some of the important works using these techniques are presented in this section.

One of the first studies to use artificial neural network (ANN) and multiple linear regression (MLR) models for experimental ground reaction force data prediction was Billing *et al*. (2006). An ANN can be defined as “a machine that is designed to *model* the way in which the brain performs a particular task or function of interest” (Csàji, 2001). A Linear Regression (LR) is a modelling technique that predicts a response variable as a function of an explanatory variable (WEISBERG, 2013). When the response variable depends on two or more explanatory variables, the Linear Regression is then called Multiple Linear Regression (MLR). In this work, GRF data was collected using a modular wearable data acquisition system and using force plates. In both cases the data was collected in the laboratory with controlled conditions. The ANN and MLR models were then used to match the modular wearable system GRF data and the force plate GRF data.

Oh *et al*. (2013) also used ANN to match experimental GRF data. In their work, experimental data from subjects walking was gathered using motion capture systems and force plates. The movement was divided into two phases, one in which there is a single foot in contact with the ground (single support phase) and other considering both feet in contact with the ground (double support phase). For the double support phase, classical Newtonian mechanics was not able to describe the GRF since the system becomes statically indeterminate. The body is divided into mass segments, and values of trajectory, velocity and acceleration were used as inputs for the ANN. The ANN GRF results were validated using the experimental GRF data.

An interesting GRF modelling technique was developed by Clark *et al*. (2014), in which the vertical GRF was constructed by summing impulse curves. The model divides the human body into upper and lower body masses, with each having its own impulse component, and the total vertical GRF corresponds to the sum of the impulse curves. The impulse curves have bell-shaped form making use of a cosine function. The curve's parameters are based on the dynamic information from the body running during contact with the ground. The lower body impulse curve is mainly responsible for the first peak region of the GRF, while the upper body impulse curve is mainly responsible for the second and bigger peak region of the GRF. The model was used to match experimental running GRF trials with reasonably accuracy.

In a recent study, Wang *et al.* (2017) used a particle filter approach to estimate the parameters of a one-DOF lumped mass system. A particle filter approach consists of using many samples (or particles) to represent posterior probability distributions of a variable of interest (CRISAN; DOUCET 2002). The particle filter approach was used to identify the lumped mass model parameters to match experimental walking GRF measurements. The estimated natural frequency and damping ratio were compared to the values found in the literature.

Despite the focus on GRF modelling in the last forty years, most of the models lack numerical accuracy or physical interpretation. Therefore, the aim of this work is to develop a running GRF model able to accurately predict running GRF datasets for different running conditions as well as correlate its parameters physically, so that it can be analyzed with respect to human body characteristics during the movement. Also, with the help of modal analysis, the influence of dominant modes over the GRF is to be investigated, which can lead to model reduction.

1.3. Objectives of the thesis

The main goal of this thesis is to present a robust model for the GRF due to the impact of the runner's foot with the ground, including variables with more physical meaning. For this purpose, the objectives are to:

1. Propose a linear ground contact model to be used in lumped parameter ground reaction force models and verify its effectiveness.
2. Perform a modal analysis of some LPMs found in the literature together with the ground contact model proposed in objective 1, to determine the possibility of model reduction and hence greater physical insight.

3. Propose a new model for the vertical GRF due to running, using the information from the modal analysis carried out in objective 2, and to validate the model using different measured data sets from the literature.

1.4. Contributions to knowledge

- It has been shown that an adaptation of the linear Zener (1950) model can be used instead of the nonlinear model proposed by Cole (1995) as the ground reaction model for the purposes of predicting the ground reaction force.

- Modal analysis of a newly formulated linear LPM has identified that there are two dominant oscillating modes and one overdamped mode that contribute to the ground reaction force

- Using a modal approach, which decomposes a measured ground reaction force, it has been shown that it is possible to assemble a robust modal model to predict the ground reaction force that hitherto has not been possible with LPMs.

1.5. Thesis' outline

This thesis consists of 6 chapters and 2 appendixes. Chapter 1 introduces the topic presenting a brief historical background of mathematical modeling, differential equations, and ground reaction force analysis. In the literature review section, the most relevant studies regarding experimental and analytical approaches to GRF analysis are presented. Later in the chapter, the thesis objectives and contributions to knowledge are presented.

In chapter 2, some of the important GRF models from the literature are discussed with more detail, including model configurations, model equations, important relations, and conclusions from obtained through the models.

In chapter 3, the Zener (1950) model is presented. An adaptation to the Zener model is then proposed making the dynamic analysis easier. The adapted Zener model is then compared to a classical ground contact model from GRF LPMs in the literature. The adapted Zener model is then compared to the nonlinear ground contact model from Nigg and Liu

(2000) model through GRF profiles comparison for two conditions, using optimization for parameter searching.

In chapter 4, a general modal analysis procedure for non-proportional damped systems is proposed. The procedure is then applied to a five-DOF and a three-DOF LPMs that uses the adapted Zener model as ground contact model. The total vertical GRF obtained through the modal analysis in both models are compared to numerically obtained total vertical GRF from the same models. The modes of vibration from each model are displayed.

In chapter 5, a new model is proposed for running vertical GRF modelling. The model consists in dividing the total vertical running GRF into three components that are related to the modes of vibration of the movement. The model is then validated through six vertical running GRF data from the literature, using an optimization procedure to find the best parameters to compose the mode and match the total experimental GRFs.

In chapter 6, the summary and conclusions of the thesis are presented, including recommendations for future work.

In Appendix A, the three-DOF model used in the modal analysis is used to show that the model cannot replicate running GRF data with good precision.

In Appendix B, the damped modal matrices obtained in the modal analysis of both five-DOF and three-DOF models are displayed.

2 LUMPED PARAMETER MODELS IN THE LITERATURE USED TO PREDICT THE GRF

2.1. Introduction

In this chapter, the aim is to discuss in more depth some of the important works regarding GRF modelling, to provide familiarity with the GRF modeling process and analysis. The works are presented in the following chronological order: first, the work of Blickhan (1989) (section 2.1); next, the work of Alexander (1990) (section 2.2); later, the work of Nigg and Liu (1999) (section 2.3); next, the work of Clark *et al*. (2014) (section 2.4); Lastly, the work from Verheul *et al*. (2019) (section 2.5).

2.2. Blickhan models

One of the first mathematical models proposed that simulates the running ground reaction force is the one-DOF model proposed by Blickhan (1989). The model consists of a massless spring connected to a lumped mass and was studied for animal running and hopping. Since the interest is in ground reaction force modelling, only the stance phase of the movement is analyzed in the Blickhan model. The model considers two situations: hopping at zero horizontal speed and hopping forward (nonzero horizontal speed). The configuration of the model for hopping at zero speed is shown in Fig. 2.

Figure 2 - Blickhan one-DOF model considering the stance phase only and hopping at zero horizontal speed

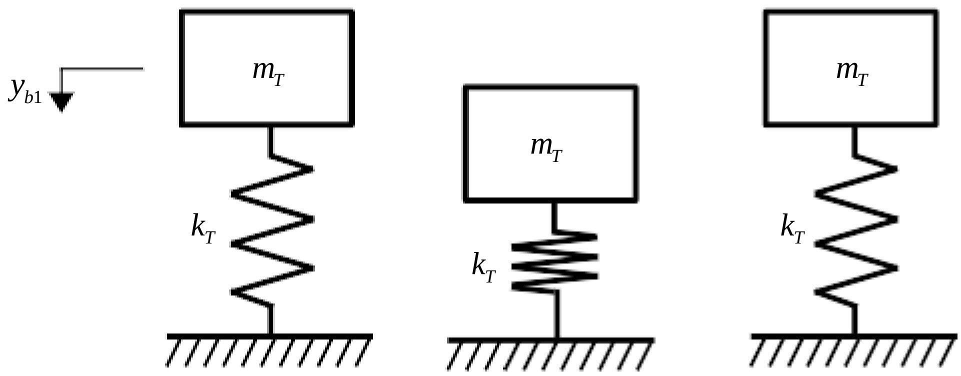

Source: elaborated by the author.

In Fig. 2 m_T is the concentrated body mass, k_T represents the stiffness of the legs, bones and tissues and *y* is the vertical displacement. The differential equation that represents the system is given by

$$m_T \ddot{y}_{b1} + k_T y_{b1} = m_T g \tag{1}$$

where *g* is the gravity acceleration (9.81 m/s²). Solving the differential equation for specific initial conditions ($y_{b1} = 0$ at $t = 0$) leads to

$$y_{b1} = \dot{y}_{b1,0} \left(\frac{m_T}{k_T} \right)^{1/2} \sin \omega_n t - \left(\frac{g m_T}{k_T} \right) \cos \omega_n t + \frac{g m_T}{k_T} \tag{2}$$

where $\dot{y}_{b1,0}$ is the landing velocity (initial vertical velocity) and ω_n is the natural frequency, which for this system is $(k_T / m_T)^{1/2}$. Since the force through the spring is given by $F_{spring} = k_T y_{b1}$, the ground reaction force for this condition can be defined as

$$F_{b1,T} = \dot{y}_{b1,0} (k_T m_T)^{1/2} \sin \omega_n t - g m_T \cos \omega_n t + g m_T \tag{3}$$

Considering a human with a 70 kg mass with a stiffness of 6 kN/m (Blickhan, 1989) and a landing velocity of 2 m/s (ZADPOOR *et al.*, 2007), the GRF using this model considering the stance phase for is presented in Fig. 3.

Figure 3 - Blickhan model's GRF considering the stance phase only and hopping at zero horizontal speed

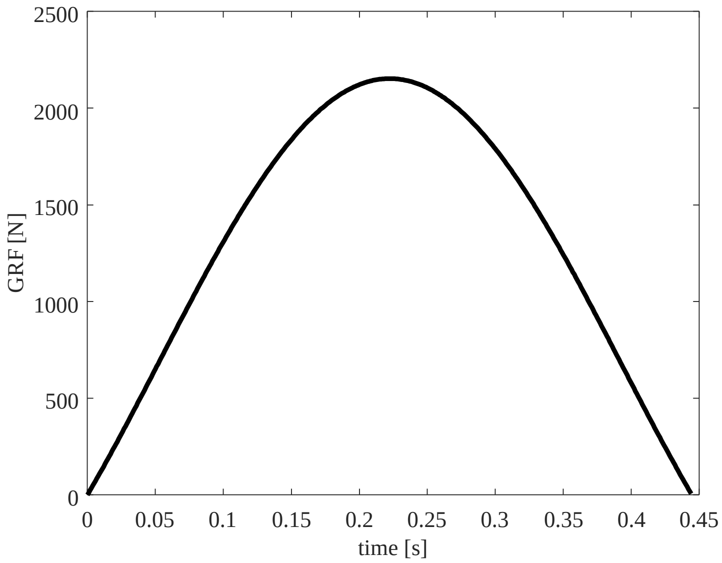

Source: elaborated by the author.

Now consider Blickhan's one-DOF model for hopping moving forward. The configuration of the one-DOF mode in this case is shown in Fig. 4.

Figure 4 - Blickhan's one-DOF model considering the stance phase only and hopping forward.

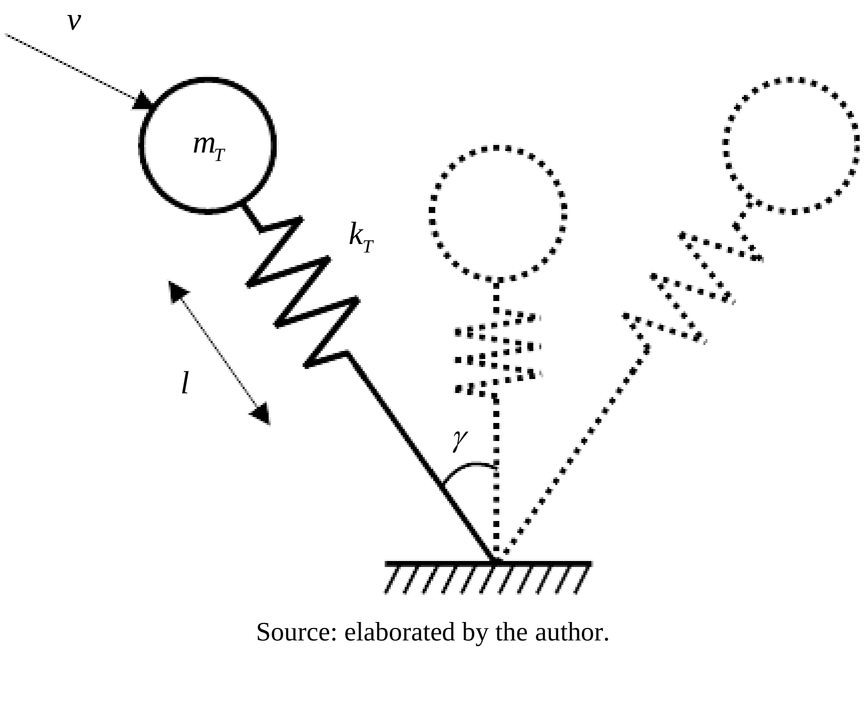

Source: elaborated by the author.

In this case, there are two differential equations that represent the movement of the mass attached to the massless spring. One is related to the vertical motion and another is related to the horizontal motion. The motion of the mass in the horizontal and vertical directions are respectively described by

$$\ddot{x}_{b2} = x_{b2}\omega_n{}^2\left[\frac{l}{(x_{b2}^2 + y_{b2}^2)^{1/2}} - 1\right] \tag{4}$$

$$\ddot{y}_{b2} = y_{b2}\omega_n{}^2\left[\frac{l}{(x_{b2}^2 + y_{b2}^2)^{1/2}} - 1\right] - g \tag{5}$$

where x_{b2} is the horizontal displacement, y_{b2} is the vertical displacement, *m* is the mass, *l* is the length of the spring which is equal to $\left(x_{b2,0}^2 + y_{b2,0}^2\right)^{1/2}$, $x_{b2,0}$ is the initial horizontal position of the mass and $y_{b2,0}$ is the initial vertical position of the mass. Eqs. (4) and (5) represent a set of nonlinear differential equations. In this case, besides the mass and the stiffness there are more parameters to be defined in the system. Specifically, the spring length *l*, the landing velocity *v* and the angle of contact γ. The solution of the equations is obtained numerically using the fourth order Runge-Kutta method, and the GRF is obtained by multiplying y_2 by k_T, in the way that was done for the previous case. The simulation uses again $k_T = 6$ kN/m and $m_T = 70$ kg. The landing velocity is divided into its *x* and *y* components, being $v_x = 4$ m/s and $v_y = 3$ m/s., the length *l* is defined to be 1.035m and the angle of contact γ is 15º. The GRF is plotted without considering the GRF offset due to the initial position of the mass m_T. The GRF as a function of time is displayed in Fig. 5.

Figure 5 - Blickhan's model GRF considering the stance phase only and hopping forward.

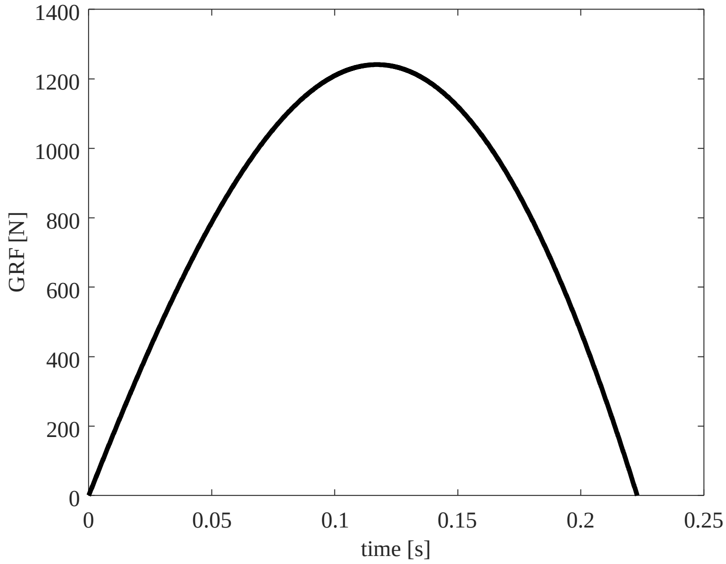

Source: elaborated by the author.

Despite the simplicity of the models, the author concluded that both models were able to represent running and hopping remarkably well. But the validity of such simple models should not be overstressed (for example, animals in general do not have similar take-off and landing velocity as assumed in the model. The success of the model is due to general features like the conservation of momentum during ground contact, coupling of horizontal traveling time to the elastic rebound of the spring and coupling between horizontal and vertical forces.

2.3. Alexander 2 DOF model

A study talking about the use of springs for legged locomotion was carried out by Alexander (1990). In this study, Alexander proposed a model to simulate the running behavior of an animal or robot with a padded foot. The addition of the foot pad is proposed to avoid excessive impact forces (Alexander, 1990). The model also separates the foot from the body using two lumped masses. The LPM from the paper is shown in Fig. 6.

Figure 6 - Alexander's two-DOF model with padded foot.

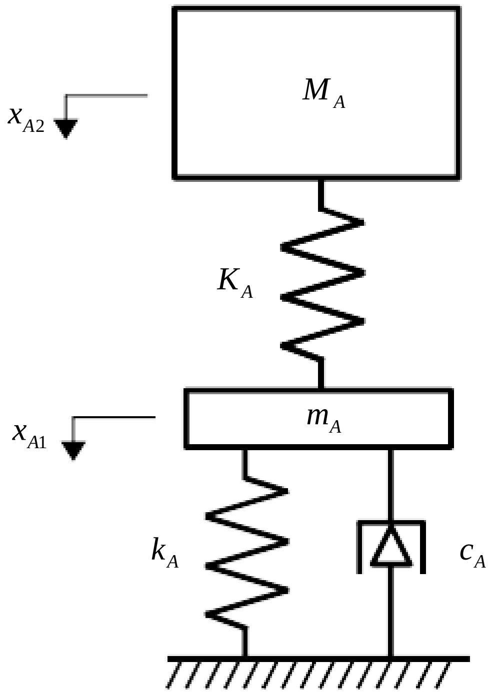

Source: elaborated by the author.

The model consists of a body mass M_A, a spring K_A connecting the body mass and the foot, a foot mass m_A, and a spring k_A in parallel with a rate-independent damper c_A. The rate-independent damper returns a fraction β of the work done in its elastic recoil. The choice of a rate-independent damper instead of a viscous damper is used for mathematical convenience and because it is more characteristic of rubber-like polymers such as usually used in pads (ALEXANDER, 1900). A Schematic drawing of the graph for the force of the foot against time, following the impact of the model with the ground is presented in Fig. 7.

Figure 7 - Schematic of Alexander's padded foot model simulating the GRF in respect to the foot in contact with ground.

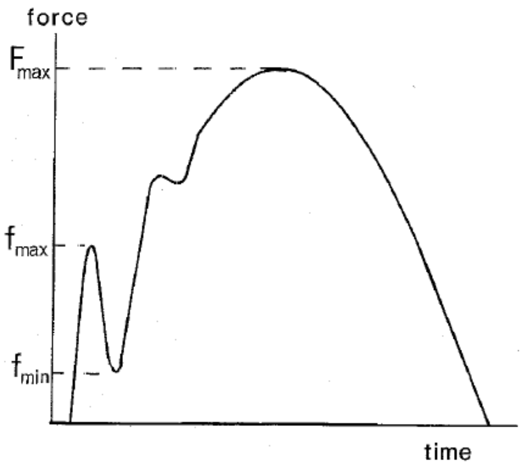

Source: Alexander (1990)

The first peak $f_{\max}$ occurs due to the effect of the foot mass m_A vibrating on the spring k_A. At the same time, the body mass M_A slowly start to vibrate through spring K_A, forming $F_{\max}$ (Alexander *et al.*, 1990). This pattern of the ground reaction force can be observed in animal and human running measured through force plates (Dickinson *et al.*, 1985; Bryant *et al.*, 1987; Wojtusch and von Stryk, 2015; Clark *et al.*, 2017).

Some important information can be extracted from this model, according to Alexander (1990). The foot mass m_A is presumably small compared to the body mass M_A. The stiffness k_A must be larger than stiffness K_A because despite both having a contribution to the force $F_{\max}$, the pad with reasonable thickness deforms much less than the leg. Still according to Alexander (1990), the mean forces $f_{\max}$ and $F_{\max}$ can be approximately estimated by looking at the momentum of the masses M_A and m_A. The two forces can be correlated as

$$\frac{f_{\max}}{F_{\max}} = \frac{v_A}{V_A}\left(\frac{m_A k_A}{M_A K_A}\right)^{1/2} \tag{6}$$

Where v_A is the velocity of the foot mass and V_A is the velocity of the body mass. So, to keep $f_{\max}$ small (which is desirable), m_A and k_A should be small, and the foot should go downwards with a small velocity.

Still according to Alexander (1990), a phenomenon called “chattering” should be avoided. This phenomenon consists in the foot leaving and returning to the ground repeatedly before settling on the ground. To avoid this, considering that before the impact with the ground the foot has momentum $m_A v_A$ and kinetic energy $(1/2)\beta m_A v_A{}^2$ and considering that the impulse delivered in spring K_A must be $\beta^{1/2} m_A v_A$ leads to

$$\frac{k_A}{K_A} < \frac{5V_A}{\beta^{1/2} v_A} \tag{7}$$

the foot should have a soft pad (low k_A) and a small downward velocity v_A. By isolating V_A / v_A in Eq. (7), Eqs. (6) and (7) can be combined in the form of

$$\frac{f_{\max}}{F_{\max}} = 5\left(\frac{m_A K_A}{\beta M_A k_A}\right)^{1/2} \tag{8}$$

As general conclusions, according to Alexander (1990), since the foot mass is small compared to the body mass, $f_{\max} / F_{\max}$ will not be large, and if the condition of no chattering is obtained, it is unlikely that the foot will suffer high impact forces. The spring constant k_A cannot be too low because it could reach maximum compression under the load $F_{\max}$ but also cannot be too high to avoid chattering.

2.4. Nigg and Liu four-DOF nonlinear model

A four-DOF nonlinear LPM was proposed by Nigg and Liu (1999), with the objective of observing the effect of muscle stiffness and damping on simulated running GRF’s. This work is a reference to running GRF modelling and has been studied and used in several different works afterwards (LIU and NIGG (2000); YUE and MESTER (2004); ZADPOOR *et al*. (2007); NIKOOYAN and ZADPOOR (2007); ZADPOOR and NIKOOYAN (2010); LY *et al*. (2010); NIKOOYAN and ZADPOOR (2011); etc). Nigg and Liu’s model (NLM) will be used later in the work as a comparison model for a proposed linear ground contact relation and for modal analysis. The model is illustrated in Fig. 8.

Figure 8 - Four-DOF nonlinear LPM proposed by Nigg and Liu.

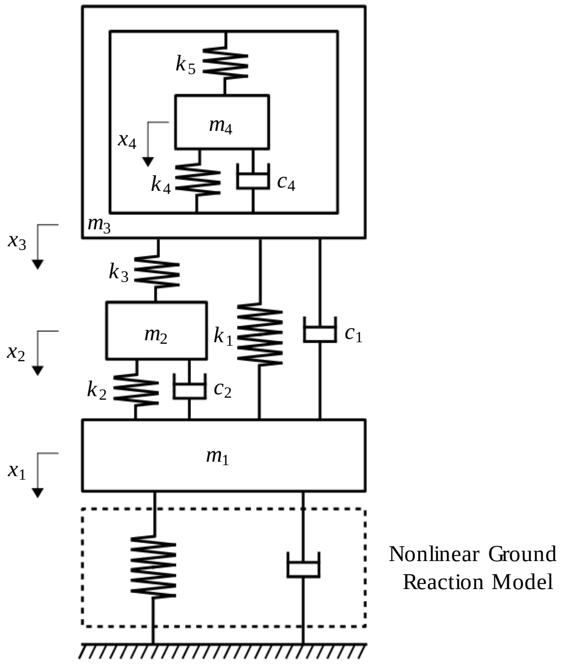

Source: elaborated by the author.

The model consists of four lumped masses; the upper body together with the leg that is not in contact with the ground are represented by a combination of a rigid mass (m_3) and a wobbling mass (m_4), which corresponds to the mass of the soft parts that shifts relative to the bony parts of the body during the movement (Gruber *et al*., 1998); the shank, leg and foot of the leg in contact with the ground are represented by a combination of a rigid mass (m_1) and a wobbling mass (m_2) (Nigg and Liu, 1999). The values of the parameters of the model (masses, stiffnesses and dampers) are defined based on Liu and Nigg (2000)[1]. The touchdown velocities are 0.6 m/s for all the masses. These parameters are presented in Table 1 next.

Table 1 - NLM's simulation parameters.

masses [kg]	springs [kN/m]	dampers [Ns/m]	touchdown velocities [m/s]
m_1 = 6.15	k_1 = 6	c_1 = 300	$v_1(0)$ = 0.6
m_2 = 6	k_2 = 6	c_2 = 650	$v_2(0)$ = 0.6
m_3 = 12.58	k_3 = 10	c_4 = 1900	$v_3(0)$ = 0.6
m_4 = 50.34	k_4 = 10		$v_4(0)$ = 0.6
	k_5 = 18		

Source: Liu and Nigg (2000).

[1] Estimated the parameters through the works done by Hörler (1972), Cole (1995), McMahon and Cheng (1990), Farley and González (1996).

The four masses are connected through springs and dampers; the upper wobbling mass m_4 is connected to the upper rigid mass m_3 through springs k_4, k_5 and damper c_4; the wobbling mass of the leg in contact with the ground is connected to the upper body rigid mass through a spring k_3, and to the lower rigid body mass through a spring k_2 and a damper c_2; the upper rigid body is connected to the lower rigid body through a compressive spring k_1 and a damper c_1.

The ground reaction model used in this model is a nonlinear viscoelastic force model with combined material properties of heel-pad, shoe and contact surface, similar to the one used by Cole (1995) (Liu and Nigg, 2000). This relation is defined as

$$\begin{aligned} F_g &= A_{cc}\left(a_{sh}x_1^{b_{sh}} + c_{sh}x_1^{d_{sh}}\dot{x}_1^{e_{sh}}\right) \quad \text{for } x_1 > 0 \\ F_g &= 0 \qquad\qquad\qquad\qquad \text{for } x_1 \le 0 \end{aligned} \tag{9}$$

The force F_g (ground reaction force) resultant of the ground contact model relation is a nonlinear function of the deformation of the lower rigid body (x_1) and the lower rigid body velocity ($\dot{x}_1$). Both velocity and displacement have linear and nonlinear relation with the parameters $a_{sh}, b_{sh}, c_{sh}, d_{sh}$ and e_{sh}, that are assumed to be shoe specific (Liu and Nigg, 2000). The parameter A_{cc} is equal to 2 and refers to the area of contact, which is twice the area reported in the pendulum tests done by Aerts and De Clercq (1993). Two types of foot-shoe models were simulated (hard and soft). The soft and hard sole conditions were simulated through the parameters of the nonlinear ground contact relation. They were also defined based on pendulum impact rests performed with two different shoes in the work done by Aerts and De Clercq (1993). Table 2 presents the parameters for the nonlinear ground contact relation.

Table 2 - Ground contact model parameters for the NLM.

	a_{sh}	b_{sh}	c_{sh}	d_{sh}	e_{sh}
soft sole	$2x10^6$	1.56	$1x10^4$	0.73	1
hard sole	$2x10^6$	1.38	$1x10^4$	0.75	1

Source: Adapted from Liu and Nigg (2000).

The equations of motion of the masses in the model are presented in Liu and Nigg (2000) and are shown in Eqs. (10a) to (10d).

$$m_1\ddot{x}_1 = m_1 g - F_g - k_1(x_1 - x_3) - k_2(x_1 - x_2) - c_1(\dot{x}_1 - \dot{x}_3) - c_2(\dot{x}_1 - \dot{x}_2) \quad (10a)$$

$$m_2\ddot{x}_2 = m_2 g - k_2(x_1 - x_2) - k_3(x_2 - x_3) + c_1(\dot{x}_1 - \dot{x}_2) \quad (10b)$$

$$m_3\ddot{x}_3 = m_3 g + k_1(x_1 - x_3) + k_3(x_2 - x_3) - (k_4 + k_5)(x_3 - x_4) + c_1(\dot{x}_1 - \dot{x}_3) - c_4(\dot{x}_3 - \dot{x}_4) \quad (10c)$$

$$m_4\ddot{x}_4 = m_4 g + (k_4 + k_5)(x_3 - x_4) + c_4(\dot{x}_3 - \dot{x}_4) \quad (10d)$$

Using the equations of motion and the parameters from Tables 1 and 2, the ground reaction force is simulated numerically using 4th-order Runge-Kutta method. The GRF's profiles for soft and hard sole conditions are presented in Fig. 9 next.

Figure 9 - NLM's GRF. a) soft sole (▬) condition; b) hard sole (——) condition.

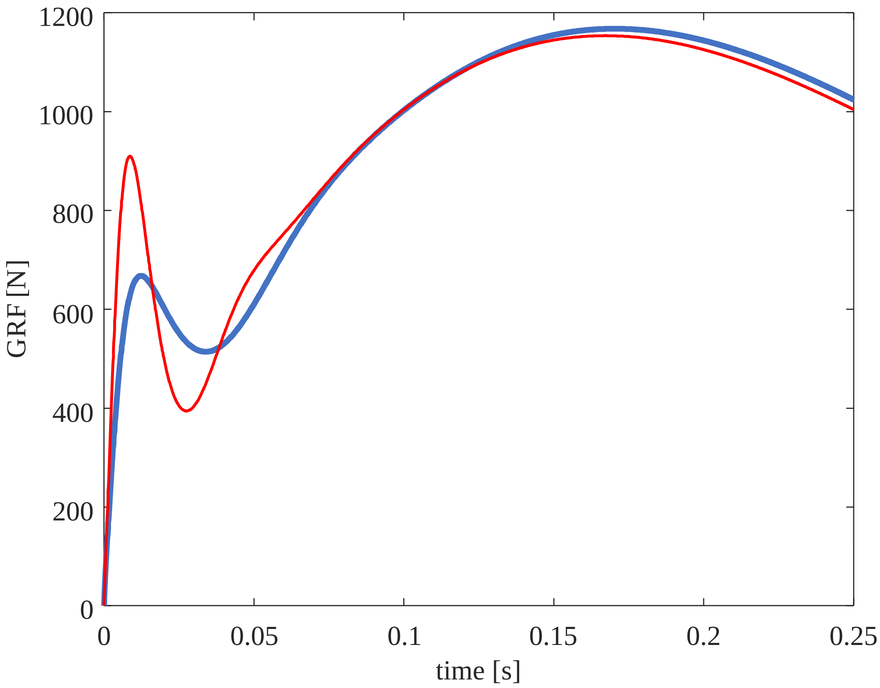

Source: Adapted from Nigg and Liu (1999)

According to Nigg and Liu (1999), the simulations of the model were able to match the range of vertical impact force peak and loading rate of experimentally measured results with human subjects (Nigg, 1986). It is clear that a hard sole lead to a higher first peak, which means that the body is receiving a higher force upon the foot impact, which is undesirable. The GRF prediction on the later part of the stance phase is not very accurate since the GRF should be zero when the foot leaves the ground. This is the main problem of the model.

2.5. Clark *et al*. model

A model consisting of two motions combined was proposed by Clark *et al*. (2014). The model theorizes that running vertical force-time waveforms consist of two components, each corresponding to the motion of a discrete portion of the body mass (Clark *et al*, 2014). The total body mass is divided in two portions: a mass m_{c1} corresponding to the impact of the lower limb to the running surface and a bigger mass m_{c2} corresponding to the rest of the body mass.

The GRF relation proposed consists in considering the impulses of the two masses ($m_{c1} = 0.08 m_T$ and $m_{c2} = 0.92 m_T$). According to Clark *et al*. (2014), since the net vertical displacement of the body over contact time during steady-speed running is zero, the time-averaged GRF must be equal to the body weight. So, the total stance-averaged vertical force F_{Tavg} can be determined by knowing foot-contact time t_c and aerial time t_a known, using the relation

$$F_{\text{Tavg}} = m_T g \frac{t_{\text{step}}}{t_{\text{con}}} \tag{11}$$

where the step time is $t_{\text{step}} = t_{\text{con}} + t_{\text{aer}}$, m_T is the body mass and g is the gravitational acceleration ($g = 9.8$ m/s²). The total ground reaction force due to running can be modelled as the impulse of the total body mass due to its instant acceleration or the impulse of the separated masses, as follows

$$J_{\text{T}} = J_1 + J_2 = F_{\text{Tavg}} t_{\text{con}} \tag{12}$$

where J_{T} is the total impulse, J_1 is the impulse resulting of the acceleration of the lower limb mass m_{CL1} and J_2 is the acceleration of the remainder of the body's mass m_{CL2}. Impulse J_1 can be evaluated from the deceleration of m_{c1} on impact

$$J_1 = F_{1\text{avg}}(2\Delta t_1) = m_{CL1}\left(\frac{\Delta v_1}{\Delta t_1} + g\right)(2\Delta t_1) \tag{13}$$

where Δt_1 is the time between contact and velocity of m_{CL1} going to zero, Δv_1 is the change in velocity during Δt_1 and $F_{1\text{avg}}$ is the average force during total time $(2\Delta t_1)$ of impulse J_1. After $(2\Delta t_1)$ ends, $F_{1avg} = 0$. J_2 is defined as the difference between J_{T} and J_1

$$J_2 = J_T - J_1 = F_{2\text{avg}} t_{\text{con}} \tag{14}$$

where $F_{2\text{avg}}$ is the average force of J_2 during t_{c}. Still according to Clark *et al*. (2014), The bell-shaped curves can be modelled using the raised cosine function

$$F_{CL}(t) = \begin{cases} \dfrac{O}{2}\left[1 + \cos\left(\dfrac{t - N}{P}\pi\right)\right] & \text{for } N - Q \leq t \leq N + Q \\ 0 & \text{for } t < N - Q \text{ and } t > N + Q \end{cases} \tag{15}$$

in which O is the peak amplitude, N is the time to reach the peak and Q is the half-width time interval. Since the function is symmetric, peak amplitude is $O = 2F_{\text{Tavg}}$ and the area under the curve is $J = O.Q$. The total force is defined as a sum of both impulses using Eq. (15)

$$F_{\text{CL,T}}(t) = \frac{O_1}{2}\left[1 + \cos\left(\frac{t - N_1}{Q_1}\pi\right)\right] + \frac{O_2}{2}\left[1 + \cos\left(\frac{t - N_2}{Q_2}\pi\right)\right] \tag{16}$$

The model is compared to different GRF datasets for validation. The parameters for the model function were obtained through manual iterative process with Δt_1 and Δv_1 as constraints, using values from available literature. The comparison of the model GRF with the GRF datasets is presented in Figs. 10 to 13.

Figure 10 - Model's GRF fit to experimental dataset. a) Lieberman *et al*. (2010) GRF dataset for a barefoot runner with forefoot strike at 3.5 m/s (----) compared to the total GRF from the model (——) after iterations; b) total model GRF (——), lower limb impulse (········) and upper body impulse (----).

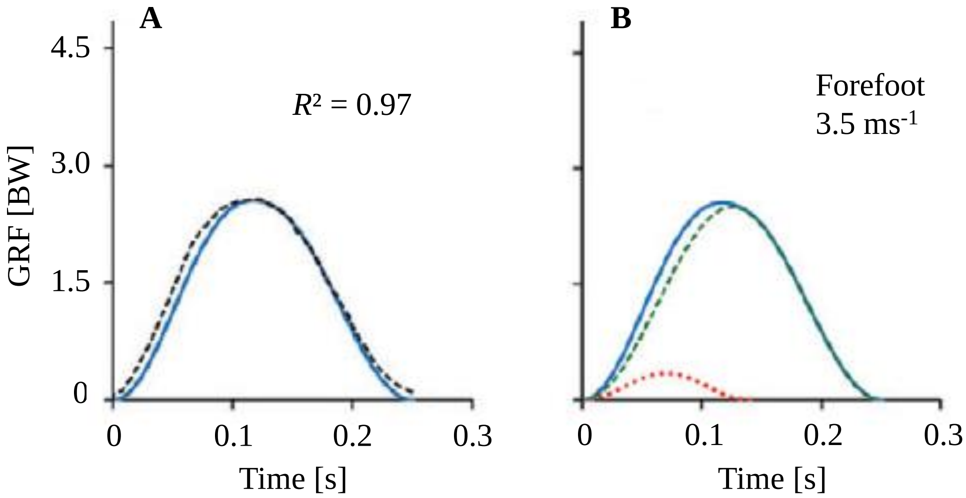

Source: Adapted from Clark *et al*. (2014)

Figure 11 - Model's GRF fit to experimental dataset. a) Weyand *et al*. (2000) GRF dataset for a shod runner with rearfoot strike at 5 m/s (----) compared to the total GRF from the model (——) after iterations; b) total model GRF (——), lower limb impulse (········) and upper body impulse (----).

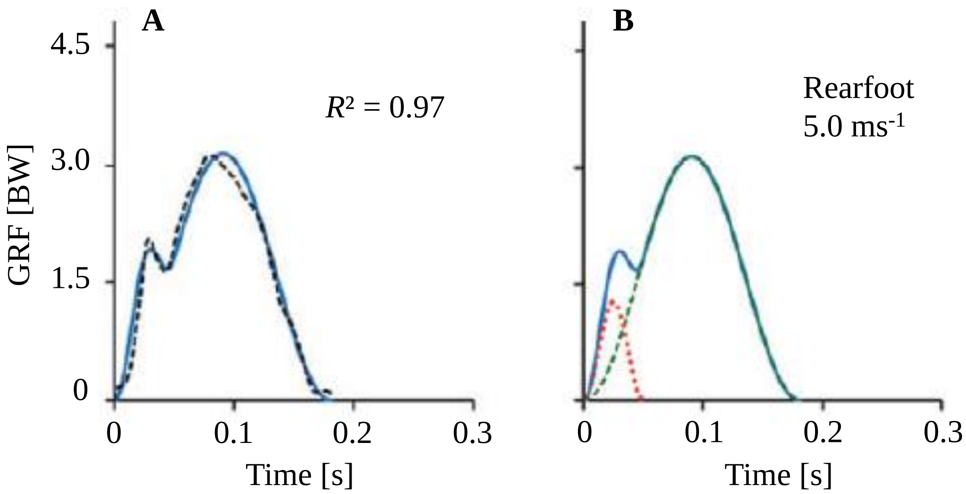

Source: Adapted from Clark *et al*. (2014)

Figure 12 - Model's GRF fit to experimental dataset. a) Weyand *et al*. (2010) GRF dataset for a shod runner with forefoot strike at 5 m/s (----) compared to the total GRF from the model (——) after iterations; b) total model GRF (——), lower limb impulse (·······) and upper body impulse (----).

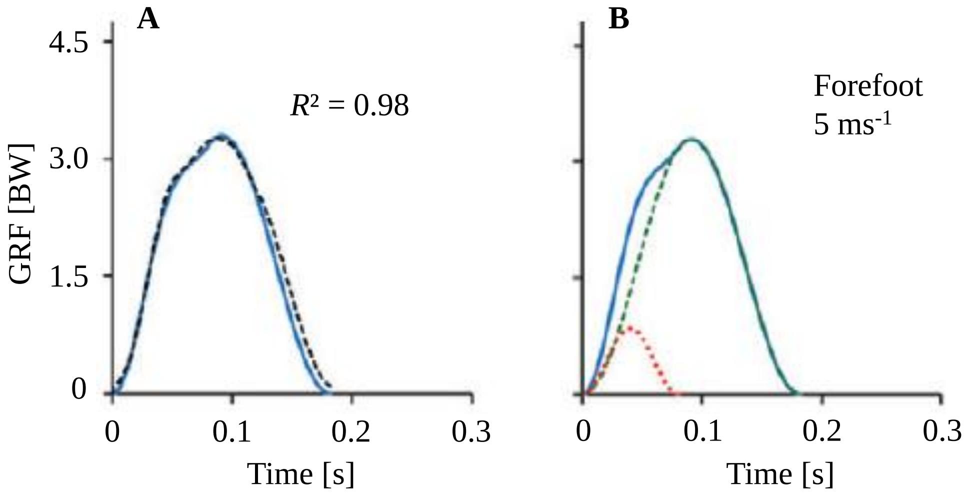

Source: Adapted from Clark *et al*. (2014)

Figure 13 - Model's GRF fit to experimental dataset. a) Weyand *et al*. (2009) GRF dataset for a shod runner with forefoot strike at 10.5 m/s (----) compared to the total GRF from the model (——) after iterations; b) total model GRF (——), lower limb impulse (·······) and upper body impulse (----).

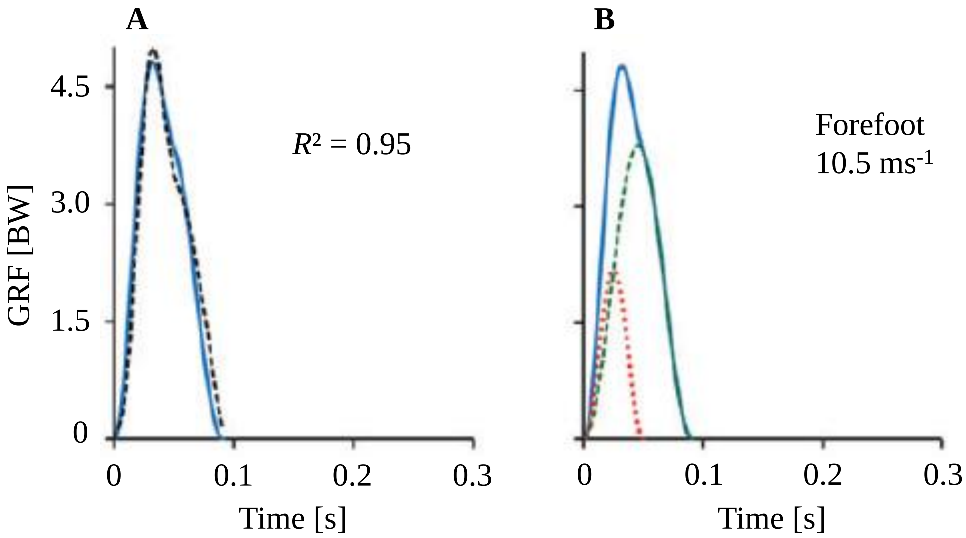

Source: Adapted from Clark *et al*. (2014)

Table 3 presents the mode function parameters for each case as well as information regarding the experimental datasets used for comparison.

Table 3 - Waveforms from Clark etl al. (2014); t_c is the contact time; t_a is the aerial time; Δt_1 is the time interval between touchdown and vertical velocity of component m_1 slowing to zero; v_{zlimb} is the vertical velocity of lower limb.

[a]Data from Nigg *et al*. (1987), table 1 in their appendix; listed value is -0.80 m/s at running speed of 3.0 m/s.
[b]Data from Nigg *et al*. (1987), table 1 in their appendix.
[c]Data derived from Mann and Herman (1985); listed value is a horizontal foot velocity of -7,93 m/s at running speed of 10.21 m/s.

								v_{zlimb} at touchdown [m/s]	
Reference	Speed [m/s]	Foot-strike	Shod condition	Total mass [kg]	t_c [s]	t_a [s]	Δt_1 [s]	model	published
Lieberman *et al*. (2010)	3.5	Fore-foot	Barefoot	70.00	0.251	0.087	0.070	-0.80	-0.80[a]
Weyand *et al*. (2000)	5.0	Rear-foot	Shod	72.06	0.181	0.136	0.025	-1.70	-1.60[b]
Weyand *et al*. (2010)	5.0	Fore-foot	Shod	69.21	0.182	0.152	0.040	-1.70	-1.60[b]
Weyand *et al*. (2009)	10.5	Fore-foot	Shod	69.21	0.091	0.136	0.025	-3.10	-3.00[c]

Source: Adapted from Clark *et al*. (2014)

The model fits for all four cases were reasonably good. A fit of more than 90% (i.e. $R^2 \geq 0.90$) for the model was hypothesized by the authors, which was successfully achieved.

2.6. Verheul *et al*. two-DOF model

A recent work developed by Verheul *et al*. (2019) used a two-DOF LPM to simulate ground reaction forces in high-intensity tasks. The model is similar to the model from Derrick *et al* (2000), having eight natural parameters. The schematic representation of the model is presented in Fig. 14.

Figure 14 - Schematic representation of the model proposed by Verheul *et al*.

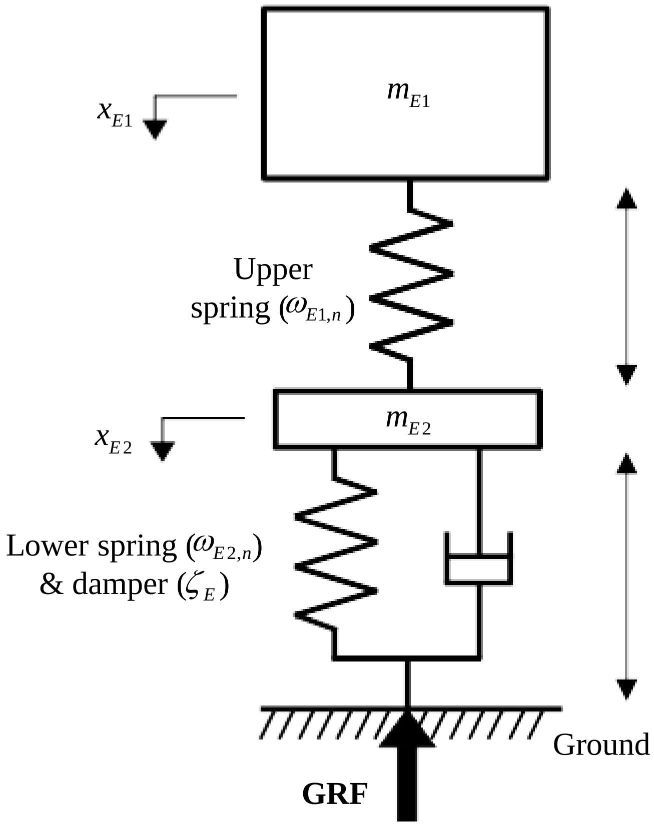

Source: Adapted from Verheul *et al*. (2019)

According to Verheul *et al*. (2019), the model consists of a smaller mass m_{E2} on a spring and a damper, representing the support leg, with a bigger mass m_{E1} on a spring on top, representing the rest of the body. The positions of the upper and lower masses without external forces applied is defined by x_{E1} and x_{E2}, while l_{E1} and l_{E2} are the natural lengths of the upper and lower springs, respectively. The linear spring constants from the upper and lower springs are defined as k_{E1} and k_{E2} respectively, while c_E is the damper's damping coefficient. From these nine parameters, eight natural parameters are defined. The models' motion is described by the accelerations of upper and lower masses ($acel_{E1}$ and $acel_{E2}$, respectively). The velocities and positions of the upper and lower masses are v_{E1}, v_{E2}, p_{E1} and p_{E2} respectively. The natural parameters, the equations of motion and the GRF equation are presented in Table 4 below where *BM* is the body mass and *g* is the gravitational acceleration (-9.81 m/s²).

Table 4 - Equations and natural parameters of the two-DOF LPM.

Initial position of the upper mass	$p_{E1} = x_{E1} - l_{E1} - l_{E2}$	Equation 17
Initial position of the lower mass	$p_{E2} = x_{E2} - l_{E2}$	Equation 18
Initial velocity of the upper mass	$v_{E1} = \dot{p}_{E1}$	Equation 19
Initial velocity of the lower mass	$v_{E2} = \dot{p}_{E2}$	Equation 20
Mass ratio	$\lambda_E = \dfrac{m_{E1}}{m_{E2}}$	Equation 21
Natural frequency of the upper spring	$\omega_{E1,n} = \sqrt{\dfrac{k_{E1}}{m_{E1}}} = \sqrt{\dfrac{(1-\lambda_E)\cdot k_{E1}}{\lambda_E \cdot BM}}$	Equation 22
Natural frequency of the lower spring	$\omega_{E2,n} = \sqrt{\dfrac{k_{E2}}{m_{E2}}} = \sqrt{\dfrac{(1-\lambda_E)\cdot k_{E2}}{BM}}$	Equation 23
Damping ratio of the damper	$\zeta_E = \dfrac{c_E}{2.\sqrt{k_{E2}.m_{E2}}}$	Equation 24
Acceleration of the upper mass	$acel_{E1} = -\omega_{E1}^2 \cdot (p_{E1} - p_{E2}) + g$	Equation 25
Acceleration of the lower mass	$acel_{E2} = -\omega_{E2}^2 \cdot p_{E2} + \omega_{E1}^2 \cdot \lambda_E \cdot (p_{E1} - p_{E2}) - 2\cdot\zeta_E \cdot \omega_{E2} \cdot v_{E2} + g$	Equation 26
Ground reaction force	$GRF_E = -\dfrac{BM \cdot \omega_{E2}}{1+\lambda_E} \cdot (\omega_{E2} \cdot p_{E2} \cdot 2 \cdot \zeta_E \cdot v_{E2})$	Equation 27

Source: Verheul *et al*. (2019)

To validate the simulated GRFs from the model, experimental GRF data was gathered. Fifteen team-sports athletes participated in the study. Subjects performed accelerations from standstill to sprinting, and decelerations from sprinting to standstill and running trials at constant speeds which varies from 2 to 9 m/s. For each trial, GRF data were collected at 3000 Hz with a force platform (9287B, Kister Holding AG, Winterhur, Switzerland), filtered using a 50 Hz second-order Butterworth low-pass filter normalized to body mass (Verheul *et al*., 2019). All three components of the GRF data were gathered.

A Python optimization script was used to fit the model simulated GRF data to the experimentally measured GRF data. Equations (25) and (26) were solved for each trial and a unique set of parameters was obtained for each case. The initial conditions for the model were defined in Derrick *et al*. (2000). After the optimization procedure, new optimized initial conditions were obtained. Both optimized and base conditions (from Derrick *et al*. (2000)) are presented in Table 5.

Table 5 - Model parameter's initial conditions.

	p_{E1} (*m*)	p_{E2} (*m*)	v_{E1} (*m/s*)	v_{E2} (*m/s*)	$\omega_{E1,n}$ (*N/m/kg*)	$\omega_{E2,n}$ (*N/m/kg*)	λ_E	ζ_E
Derrick *et al*. (2000)	0.015	0.0074	-0.73	-0.66	207.00	626.00	2.00	0.35
Optimized	-0.010	0.0000	-1.29	-0.19	18.33	58.32	2.81	0.31

Source: adapted from Verheul *et al*. (2019)

The model optimization fits for moderate-speed and high-speed running are presented in Figs. 15 and 16 next. The RMSE were calculated using the area under the GRF curves.

Figure 15 - Comparison between experimentally measured (——) and model simulated (······) ground reaction force for running with moderate speeds. a) one of the subjects at 4 m/s; b) another subject at 5 m/s.

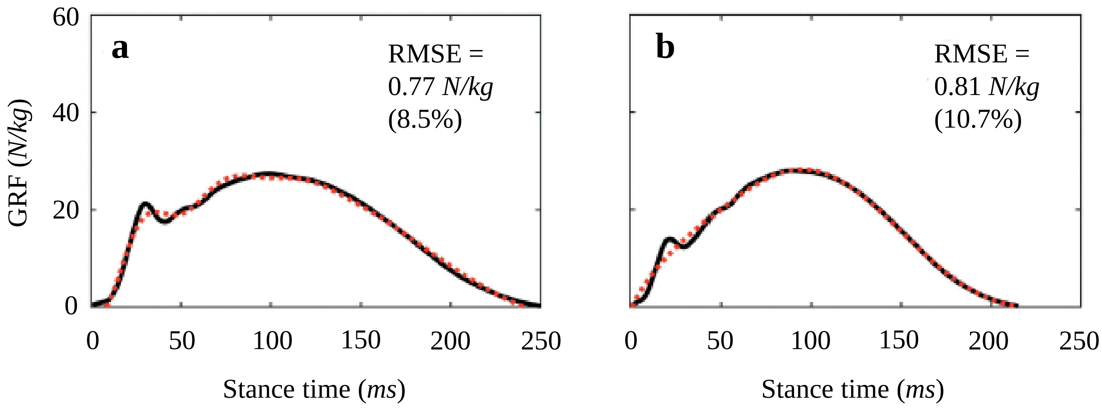

Source: adapted from Verheul *et al*. (2019)

Figure 16 - Comparison between experimentally measured (——) and model simulated (······) ground reaction force for running with moderate speeds. a) one of the subjects at speed > 6 m/s; b) another subject at speed > 6 m/s.

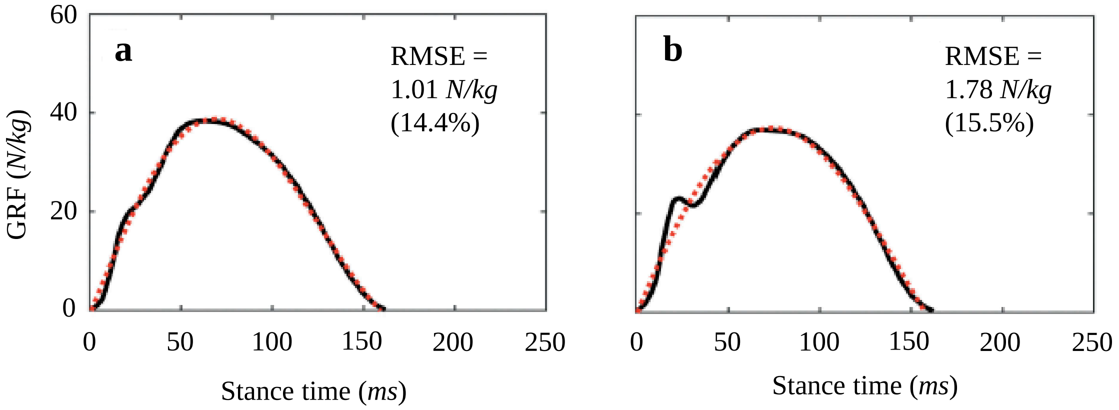

Source: adapted from Verheul *et al*. (2019)

Table 6 presents the means with standard deviations for the subjects running at moderate and high speeds after optimization.

Table 6 - Mean ± standard deviation values for the model's optimized parameters for constant speed running at moderate and high speeds.

	p_{E1} (m)	p_{E2} (m)	v_{E1} (m/s)	v_{E2} (m/s)	$\omega_{E1,n}$ ($N/m/kg$)	$\omega_{E2,n}$ ($N/m/kg$)	λ_E	ζ_E
Moderate speed (4-5 m/s)	0.91 ±5.20	0.09 ±0.80	12.67 ±137.00	-0.20 ±1.13	37±35	101±106	4.16 ±6.34	0.6 ±1.1
High speed (>6 m/s)	-2.21 ±13.37	-1.74 ±10.31	-1.83 ±115.00	0.98 ±12.62	34±35	134±148	1.93 ±4.99	1.9 ±7

Source: adapted from Verheul *et al*. (2019)

Verheul *et al* (2019) reported that the model could overall reproduce GRF curves with low to moderate errors. The larger errors were concentrated in the impact peak (first peak) regions, likely due to distinct GRF profiles. The model in general underestimated the impact peaks and loading rates but overestimated the active peaks (second peaks). The analysis and conclusions form Verheul *et al*. (2017) reported in this thesis include only the analysis in running and constant speed (moderate and high speeds), excluding the analysis for other tasks (acceleration, deceleration, running at low speed).

2.7. Conclusions

In this chapter, important GRF modelling works from the literature have been presented in more detail. First, the two LPMs developed by Blickhan (the first considering vertical motion only and the second including both vertical and horizontal motions) were discussed, including their equations of motion and GRF plots. The two-DOF LPM with a padded foot developed by Alexander was then discussed, showing some of the analysis involving energy and momentum equilibrium. Following this, the classic four-DOF nonlinear LPM proposed by Nigg and Liu was described, including the wobbling masses effect, presenting the equations of motion and GRF profiles for soft and hard sole conditions. The two-mass impulse model proposed by Clark *et al*. was then presented, including some of the considerations that led to the model development and comparison with experimental gathered vertical GRF data. Lastly, the two-DOF lumped mass model proposed by Verheul *et al*. with natural parameters was discussed, showing some results for experimental GRF data fitting through optimization.

3 LINEAR GROUND CONTACT MODEL PROPOSITION

3.1. Introduction

The aim of chapter 3 is to propose a new ground contact model for lumped parameter GRF models. In section 3.2 the general Zener model is presented. In section 3.3, an adaptation of the Zener model is proposed as a ground contact model for GRF modelling. In section 3.4, the adapted Zener model is then used in the NLM to simulate GRF and compared to the original NLM for both soft and hard sole conditions.

3.2. Zener Model

Zener (1948) proposed a model using a combination of springs and a damper (spring and damper in series, both in parallel with a spring), which can simulate the behavior of viscoelastic materials. The model is called Zener Model and its configuration is presented in Fig. 17.

Figure 17 - Zener Model schematic drawing.

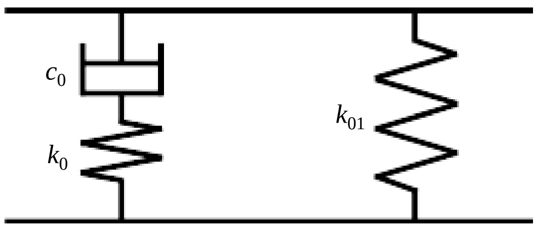

Source: elaborated by the author.

The springs k_0, and k_{01} are stiffness elements (N/m) and c_0 is a damper (kg/s). The idea is to use the Zener model as a ground contact model to simulate the ground reaction force through a LPM, since the shoe material has viscoelastic behavior. However, to avoid a third-order differential equation (BRENNAN *et al*., 2008) an adaptation to the Zener model is proposed.

3.3. Adaptation to the Zener model

To facilitate the mathematical formulation of the Zener model when inserted in a LPM, a very small mass (m_0) is inserted between the damper (c_0) and spring (k_0) that were connected in series. The mass is small enough so that its natural frequency is extremely high, with its mode being not excited during the run. Figure 18 shows the configuration Zener model with the proposed adaptation.

Figure 18 - Schematic drawing of the adaptation of the Zener model.

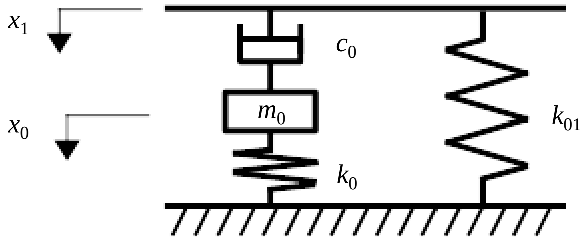

Source: elaborated by the author.

In Fig. 18, m_0 is a small concentrated mass (kg); x_0 represents the displacement of the small mass m_0; and x_1 represents the displacement of the lower body lumped mass of the MSD model attached to the Adapted Zener Model (AZM). This model is responsible for simulating the foot/shoe contact with the ground. It is connected to a lumped mass parameter model, which together with the AZM is responsible for simulating the body behavior during running. The ground reaction force (GRF) is generated when the foot/shoe is in contact with the ground, which is called stance phase. Using this model, the GRF is the force that comes from the ground and passes through both spring elements, and can be represented by

$$
\begin{aligned}
F_{Zen} &= k_0 x_0 + k_{01} x_1 \quad \text{for } x_0 \text{ and } x_1 > 0 \\
&= 0 \qquad\qquad\qquad \text{for } x_0 \text{ and } x_1 \leq 0
\end{aligned}
\tag{28}
$$

It is interesting to note that this configuration fixes one of the problems of using a common (spring in parallel with a damper) linear ground contact model to simulate the GRF. This configuration is exemplified in Fig. 19.

Figure 19 - Simple linear spring in parallel with a damper.

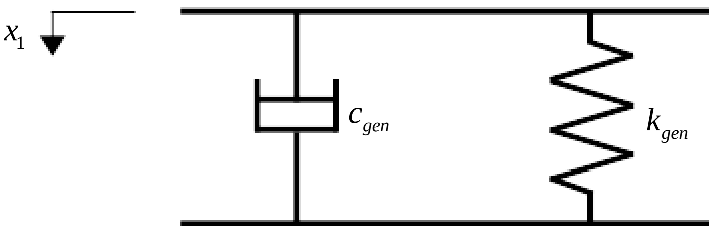

Source: elaborated by the author.

For this ground contact configuration, the GRF is evaluated as

$$\begin{aligned} F_{gen} &= k_{gen}x_1 + c_{gen}\dot{x}_1 \quad \text{for } x_1 > 0 \\ &= \ 0 \qquad\qquad\quad \text{for } x_1 \leq 0 \end{aligned} \tag{29}$$

Since the force of the foot/shoe moving towards the ground is translated into the model as impulsive forces in each of the lumped masses, it is known that the initial velocity ($\dot{x}(0)$) is non-zero right before the foot/shoe contacts the ground. This feature leads to a nonzero initial value for the GRF. However, it is known that the GRF is zero before the foot/shoe contacts the ground, which lead to an inconsistency when using this common linear ground contact relation. To verify the AZM effectiveness, it is compared to the nonlinear relation GRF relation defined Cole (1995) and applied to a four-DOF LPM by Nigg and Liu (1999).

3.4. Comparison of the nonlinear ground contact relation with a proposed linear ground contact relation

In this section, the NLM with a nonlinear ground contact relation is compared to a similar model, with a proposed linear ground contact relation, to verify its effectiveness in simulating the nonlinear behavior.

3.4.1. Nigg and Liu nonlinear model

In this section, the model from the work from Nigg and Liu (1999) is discussed again for convenience. Nigg and Liu proposed a four-DOF LPM and used Cole’s nonlinear ground contact model to study the effect of body properties over simulated running GRF. The nonlinear ground contact model used in Nigg and Liu (1999) solves the initial GRF value problem and has a good prediction of the loading rate and impact peak regions but does not model the GRF and the latter part of the stance phase. However, it is an important model for the GRF modelling literature and may be a good comparison model to validate the AZM.

The ground contact relation used in the model is defined in Eq. (9). Simplifying the equation leads to

$$F_g = a_{sh} x_1^{b_{sh}} + c_{sh} x_1^{d_{sh}} \dot{x}_1 \quad \text{for } x_1 > 0$$
$$= 0 \qquad\qquad \text{for } x_1 \le 0 \tag{30}$$

The parameters from Eq. (30) can represent soft and hard sole conditions. Table 7 presents the mentioned parameters.

Table 7 - Ground contact model parameters for the NLM.

	a_{sh}	b_{sh}	c_{sh}	c_{sh}
soft sole	2x10^6	1.56	2x10^4	0.73
hard sole	2x10^6	1.38	2x10^4	0.75

Source: elaborated by the author.

The NLM's equations of motion were presented in the previous chapter (Eqs. (10a) to (10d)). These equations can be represented in matrix form

$$\mathbf{M}_N \ddot{\mathbf{x}}_N + \mathbf{C}_N \dot{\mathbf{x}}_N + \mathbf{K}_N \mathbf{x}_N = \mathbf{f}_N \tag{31}$$

where the mass, stiffness and damping matrices are given by

$$\mathbf{M}_N = \begin{bmatrix} m_1 & 0 & 0 & 0 \\ 0 & m_2 & 0 & 0 \\ 0 & 0 & m_3 & 0 \\ 0 & 0 & 0 & m_4 \end{bmatrix}, \mathbf{C}_N = \begin{bmatrix} c_1 + c_2 & -c_2 & -c_1 & 0 \\ -c_2 & c_2 & 0 & 0 \\ -c_1 & 0 & c_1 + c_4 & -c_4 \\ 0 & 0 & -c_4 & c_4 \end{bmatrix} \text{ and}$$

$$\mathbf{K}_N = \begin{bmatrix} k_1 + k_2 & -k_2 & -k_1 & 0 \\ -k_2 & k_2 + k_3 & -k_3 & 0 \\ -k_1 & -k_3 & k_1 + k_3 + k_4 + k_5 & -k_4 - k_5 \\ 0 & 0 & -k_4 - k_5 & k_4 + k_5 \end{bmatrix}$$

The vector of responses $\mathbf{x}_N$ is given by $\mathbf{x}_N = \{x_1, \quad x_2, \quad x_3, \quad x_4\}^T$ where T denotes the transpose, and the vector of forces $\mathbf{f}_N$ is given by $\mathbf{f}_N = \{m_1 g - F, \quad m_2 g, \quad m_3 g, \quad m_4 g\}^T$.

3.4.2. Proposed model using the AZM

The model to be compared with the NLM is a similar model, with the only difference being the ground contact model. This proposed model uses the AZM as the ground contact model. The proposed model is displayed in Fig. 20.

Figure 20 - Proposed model configuration.

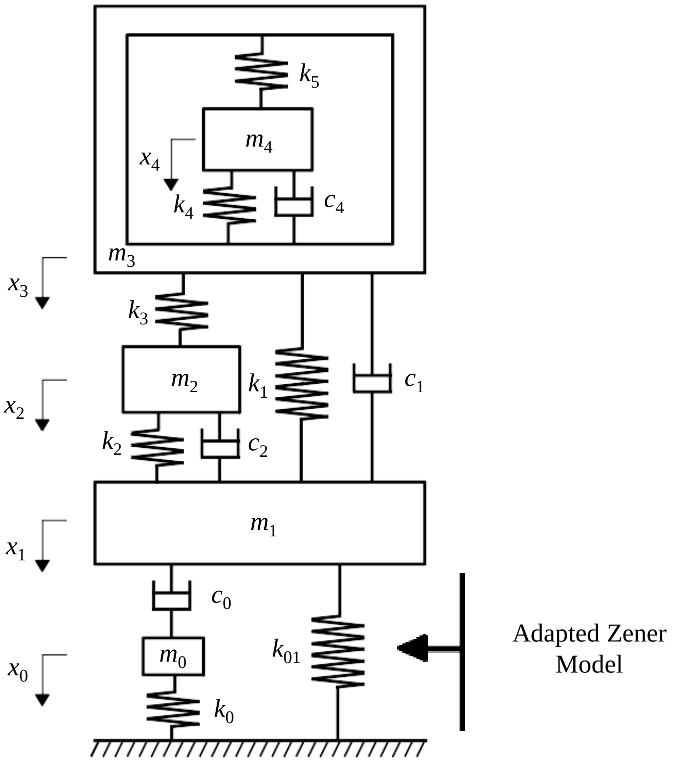

Source: elaborated by the author.

The ground reaction force simulated through this model is obtained through Eq. (28). The equations of motion that result from the proposed model in matrix form have the same configuration of Eq. (31), with the matrices being

$$\mathbf{M}_{5D} = \begin{bmatrix} m_0 & 0 & 0 & 0 & 0 \\ 0 & m_1 & 0 & 0 & 0 \\ 0 & 0 & m_2 & 0 & 0 \\ 0 & 0 & 0 & m_3 & 0 \\ 0 & 0 & 0 & 0 & m_4 \end{bmatrix}, \mathbf{C}_{5D} = \begin{bmatrix} c_0 & -c_0 & 0 & 0 & 0 \\ -c_0 & c_0+c_1+c_2 & -c_2 & -c_1 & 0 \\ 0 & -c_2 & c_2 & 0 & 0 \\ 0 & -c_1 & 0 & c_1+c_4 & -c_4 \\ 0 & 0 & 0 & -c_4 & c_4 \end{bmatrix} \text{ and}$$

$$\mathbf{K}_{5D} = \begin{bmatrix} k_0 & 0 & 0 & 0 & 0 \\ 0 & k_{01}+k_1+k_2 & -k_2 & -k_1 & 0 \\ 0 & -k_2 & k_2+k_3 & -k_3 & 0 \\ 0 & -k_1 & -k_3 & k_1+k_3+k_4+k_5 & -k_4-k_5 \\ 0 & 0 & 0 & -k_4-k_5 & k_4+k_5 \end{bmatrix}$$

The vector of responses $\mathbf{x}_{5D}$ is given by $\mathbf{x}_{5D} = \{x_0, \quad x_1, \quad x_2, \quad x_3, \quad x_4,\}^T$ where T denotes the transpose, and the vector of forces $\mathbf{f}_{5D}$ is given by $\mathbf{f}_{5D} = \{m_0 g, \quad m_1 g, \quad m_2 g, \quad m_3 g, \quad m_4 g,\}^T$.

The parameters of the proposed model have the same values of the parameters from the NLM, except for the ground contact parameters. The small mass m_0 is equal to 0.01kg. AZM (ground contact model) parameters k_0, k_{01} and c_0 are to be optimized to fit the NLM's behavior for soft and hard sole conditions.

3.4.3. Parameter optimization and model comparison

The objective of the comparison is to find the best k_0, k_{01} and c_0 to simulate the NLM's GRF for the soft and hard sole conditions. An optimization algorithm is defined for that task. The optimization algorithm chosen is the *patternsearch* algorithm in *MATLAB*. MATLAB is a software from MathWorks, Inc., originally wroten by Dr. Cleve Moler (Chief Scientist from MathWorks) for matrices analysis (**Mat**rix **Lab**oratory) and consists of in a scientific software package designed to provide integrated numeric computation and graphics visualization in a high-level programming language (Sivanandam and Deepa, 2008). The pattern search is an optimization algorithm from the class of the genetic algorithms and basically consists in spatially searching for a function tendency. This algorithm was chosen mainly because it does not need to analyze the gradient of the function and thus performs the optimization faster. The initial conditions for the small mass m_0 are $x_0(0) = 0\,\text{m}$ and $\dot{x}_0(0) = 0.96\,\text{m/s}$. The GRF resultant from NLM compared to the optimized proposed model's GRF is presented in Fig. 21 for soft and hard sole conditions.

Figure 21 - Comparison between NLM's GRF (▬▬) to the proposed model's GRF with the AZM (▪▪▪▪▪) for (a) soft sole and (b) hard sole condition.

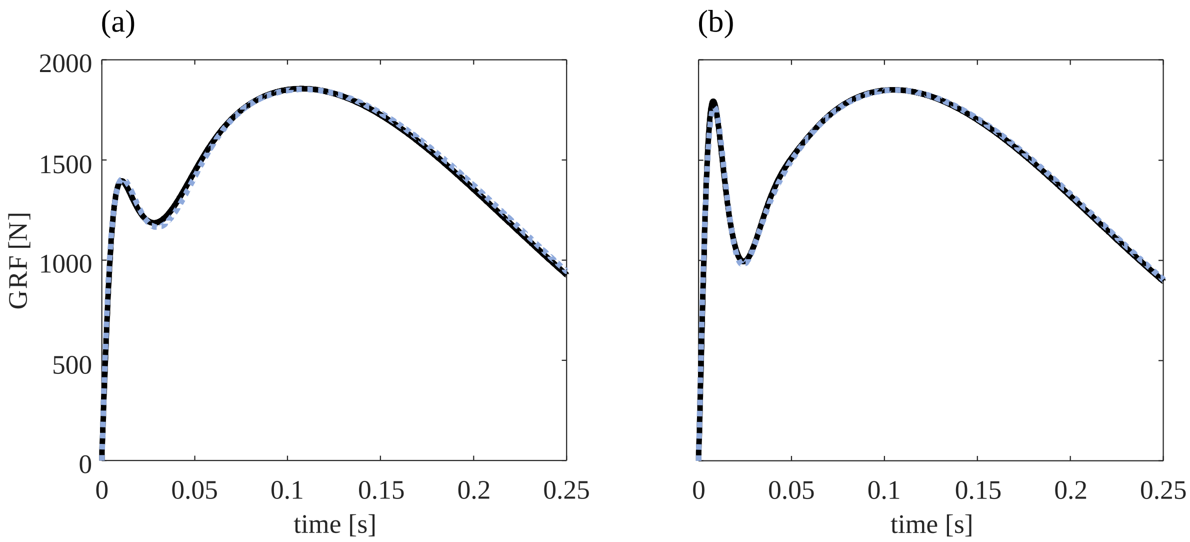

Source: elaborated by the author.

Table 8 presents the optimized parameters for the ground contact model (AZM) in the proposed model.

Table 8 - Proposed model ground contact optimized parameters.

	k_0 [kN/m]	k_{01} [kN/m]	c_0 [kg/s]
soft sole	211.26	144.52	595.17
hard sole	194.29	256.69	626.84

Source: elaborated by the author.

Figure 21 shows that for both soft and hard sole cases, the AZM could replicate the nonlinear ground contact model with good accuracy (RMSE = 1.11% for soft sole and RMSE = 0.75% for hard sole).

3.5. Conclusions

In this chapter, some of the literature on ground contact models has been discussed and compared, showing their characteristics. Using this information, a new linear ground contact model based on a well-known model has been proposed. To verify the effectiveness of the proposed ground contact model, it was applied to an important LPM from the literature, replacing the original nonlinear ground contact relation and then compared to the original model. Both models have been described in detail. A comparison between the models was made by optimizing the proposed ground contact model parameters to match the nonlinear ground contact behavior for soft and hard sole conditions. It was shown that the proposed linear model could replicate with high accuracy the behavior of the nonlinear model.

In the next chapter, a Modal Analysis procedure will be extensively described and applied to running GRF LPMs and important information will be extracted.

4 MODAL ANALYSIS

4.1. Introduction

In chapter 3 the AZM was proposed as a ground contact model for LPMs in the simulation of a GRF. It was able to simulate the nonlinear ground contact relation behavior from Nigg and Liu (1999). The aim of this chapter is to perform a modal analysis of proposed GRF LPMs, gathering important information regarding the modal behavior of the model. In section 4.2, a general modal analysis methodology is presented (using state-space representation). This methodology was chosen because the proposed GRF models have non-proportional damping. In section 4.3 the modal analysis procedure is performed on a five-DOF proposed model (model from NIGG and LIU (1999) with the AZM for the ground contact interface). In section 4.4 the modal analysis procedure is performed on a three-DOF proposed model (2 DOF LPM using the AZM for the ground contact interface).

4.2. Methodology

In this section, the modal analysis methodology for systems with non-proportional damping is discussed. This methodology is described in Tse *et al*. (1963) and Ginsberg (2001). The presented modal analysis methodology is then applied to two different proposed MSD models with non-proportional damping. A system with “non-proportional damping” is a system in which the damping and stiffness matrices are not proportional, and so the classic method to diagonalize the system (obtain uncoupled equations of motion) cannot be done. The first model is the five-DOF model presented earlier, adapted from Nigg and Liu (1999). The second is a three-DOF model adapted from Derrick *et al*. (2000) that also makes use of the AZM as a ground contact relation.

4.2.1. General Approach

The modal analysis presented is defined for a general *n*-th order system (system with *n* DOF’s). Consider a free vibration for a system with non-proportional damping. Equation (31) then becomes

$$\mathbf{M\ddot{x}} + \mathbf{C\dot{x}} + \mathbf{Kx} = \mathbf{0} \tag{32}$$

Assuming a solution of the form

$$\mathbf{x} = \boldsymbol{\psi} e^{\theta t} \tag{33}$$

Substituting Eq. (33) in Eq. (32) gives

$$(\mathbf{M}\theta^2 + \mathbf{C}\theta + \mathbf{K})\boldsymbol{\psi} e^{\theta t} = \mathbf{0} \tag{34}$$

which becomes

$$(\mathbf{M}\theta^2 + \mathbf{C}\theta + \mathbf{K})\boldsymbol{\psi} = \mathbf{H}\boldsymbol{\psi} = \mathbf{0} \tag{35}$$

where **H** is a $n \times n$ matrix. For the nontrivial solution,

$$\det(\mathbf{H}) = \mathbf{0} = u_0 + u_1\theta + u_2\theta^2 + ...u_{2n}\theta^{2n} \tag{36}$$

which is the characteristic equation of the system. The solution Eq. (33) can be then written as a superposition of the solution roots θ and its associated vectors $\boldsymbol{\psi}$ as

$$\mathbf{x} = \sum_{k=1}^{2n} I_k \boldsymbol{\psi}_k e^{\theta_k t} \tag{37}$$

where D_k is the constant related to the k-th solution ($e^{\theta_k t}$) of the homogeneous equation of motion. The relation between physical and modal coordinates is then

$$\mathbf{x}_{n\times 1} = \boldsymbol{\Phi}_{n\times 2n}\mathbf{q}_{2n\times 1} \tag{38}$$

where

$$\boldsymbol{\Phi}_{n\times 2n} = [\boldsymbol{\psi}_1 \ \boldsymbol{\psi}_2 \ ... \ \boldsymbol{\psi}_{2n}] \tag{39}$$

is the modal matrix. However, it is difficult to relate 2*n* modal coordinates with *n* physical coordinates. To overcome this difficulty, the system is defined using state-space representation.

4.2.2. State-space representation

A state vector of the form

$$\mathbf{y}_{2n\times1} = \begin{Bmatrix} \dot{\mathbf{x}}_{n\times1} \\ \mathbf{x}_{n\times1} \end{Bmatrix} = \left\{ \dot{x}_1\ \dot{x}_2\ \dot{x}_3\ \ldots\ \dot{x}_n\ x_1\ x_2\ x_3\ \ldots\ x_n \right\}^T \tag{40}$$

is assumed. Using this relation, Eq. (31) can be written as a matrix equation given by

$$\begin{bmatrix} \mathbf{0} & \mathbf{M} \\ \mathbf{M} & \mathbf{C} \end{bmatrix} \begin{Bmatrix} \ddot{\mathbf{x}} \\ \dot{\mathbf{x}} \end{Bmatrix} + \begin{bmatrix} \mathbf{-M} & \mathbf{0} \\ \mathbf{0} & \mathbf{K} \end{bmatrix} \begin{Bmatrix} \dot{\mathbf{x}} \\ \mathbf{x} \end{Bmatrix} = \begin{Bmatrix} \mathbf{0} \\ \mathbf{f} \end{Bmatrix} \tag{41}$$

where $\mathbf{f}$ is given by

$$\mathbf{f} = \{m_1 g\ m_2 g\ m_3 g\ \ldots\ m_n g\}^T \tag{42}$$

Equation (42) can be written as

$$\mathbf{A}\dot{\mathbf{y}} + \mathbf{B}\mathbf{y} = \mathbf{p} \tag{43}$$

where

$$\mathbf{A} = \begin{bmatrix} \mathbf{0} & \mathbf{M} \\ \mathbf{M} & \mathbf{C} \end{bmatrix}_{2n\times2n} \tag{44a}$$

$$\mathbf{B} = \begin{bmatrix} \mathbf{-M} & \mathbf{0} \\ \mathbf{0} & \mathbf{K} \end{bmatrix}_{2n\times2n} \tag{44b}$$

$$\mathbf{p} = \begin{Bmatrix} \mathbf{0} \\ \mathbf{f_g} \end{Bmatrix}_{2n\times1} \tag{44c}$$

For free vibrations ($\mathbf{p}$ = 0) and assuming harmonic behavior for the state response vector results in

$$\begin{Bmatrix} \dot{\mathbf{x}} \\ \mathbf{x} \end{Bmatrix} = \mathbf{y} = \boldsymbol{\varphi} e^{\alpha t} \tag{45}$$

where $\boldsymbol{\varphi}$ is related to the amplitude of the respective displacements and velocities (damped mode shape or eigenvector), and α is the eigenvalue of the new system. Substituting Eq. (45) into Eq. (43) gives

$$(\alpha \mathbf{A} + \mathbf{B})\boldsymbol{\varphi} e^{\alpha t} = \mathbf{0} \tag{46}$$

factoring out the $e^{\alpha t}$ term, Eq. (46) becomes

$$(\alpha \mathbf{A} + \mathbf{B})\boldsymbol{\varphi} = \mathbf{0} \tag{47}$$

which is a classic eigenvalue problem. The non-trivial solution ($\boldsymbol{\varphi} \neq \mathbf{0}$) gives

$$\det(\alpha \mathbf{A} + \mathbf{B}) = \mathbf{0} \tag{48}$$

Equation (48) leads to the characteristic equation of the system. The solution of Eq. (48) gives $2n$ eigenvalues α or n pairs of eigenvalues. The eigenvalue pairs give important information about the system and the modes:

- If real and negative ($\alpha < 0$), the corresponding mode is overdamped.
- If purely imaginary ($\alpha = \pm i\omega$), the corresponding mode is undamped.
- If complex conjugate, the corresponding mode is underdamped, and pair of eigenvalues have the form of

$$\alpha = -\zeta\omega_n \pm i\omega \tag{49}$$

- If any of the pairs have positive real values, the corresponding mode is unstable.

With the eigenvalues, is possible to obtain each respective eigenvector (damped mode shape) through Eq. (48). The linear combination of all the complex mode shapes forms the damped modal matrix

$$\mathbf{\Phi}_d = [\boldsymbol{\varphi}_1 \ \boldsymbol{\varphi}_2 \ \boldsymbol{\varphi}_3 \cdots \boldsymbol{\varphi}_{2n}] \tag{50}$$

4.2.3. Orthogonality property

The mode shapes (eigenvectors) are orthogonal relative to the matrices **A** and **B**. The proof is exemplified in Tse *et al*. (1964). Referring to Eq. (47), and substituting α_r and α_s for the *r*-th and *s*-th modes respectively gives

$$\alpha_r \mathbf{A} \boldsymbol{\varphi}_r + \mathbf{B} \boldsymbol{\varphi}_r = \mathbf{0} \tag{51a}$$

$$\alpha_s \mathbf{A} \boldsymbol{\varphi}_s + \mathbf{B} \boldsymbol{\varphi}_s = \mathbf{0} \tag{51b}$$

pre-multiplying Eq. (51a) by $\boldsymbol{\varphi}_s^T$, transposing the resultant equation and pre-multiplying Eq. (51b) by $\boldsymbol{\varphi}_r^T$ gives

$$\alpha_r \boldsymbol{\varphi}_r^T \mathbf{A} \boldsymbol{\varphi}_s + \boldsymbol{\varphi}_r^T \mathbf{B} \boldsymbol{\varphi}_s = \mathbf{0} \tag{52a}$$

$$\alpha_s \boldsymbol{\varphi}_r^T \mathbf{A} \boldsymbol{\varphi}_s + \boldsymbol{\varphi}_r^T \mathbf{B} \boldsymbol{\varphi}_s = \mathbf{0} \tag{52b}$$

subtracting Eq. (52b) from Eq. (52a) gives

$$(\alpha_r - \alpha_s) \boldsymbol{\varphi}_r^T \mathbf{A} \boldsymbol{\varphi}_s = \mathbf{0} \tag{53}$$

for $\alpha_r \neq \alpha_s$, implies

$$\boldsymbol{\varphi}_r^T \mathbf{A} \boldsymbol{\varphi}_s = \mathbf{0} \tag{54}$$

Similarly, it can be shown that

$$\boldsymbol{\varphi}_r^T \mathbf{B} \boldsymbol{\varphi}_s = \mathbf{0} \tag{55}$$

Equations (54) and (55) represent the orthogonal relations for systems with viscous damping (systems were A and B are symmetric). It is implicit that Eqs. (54) and (55) are not zero when $\alpha_r = \alpha_s$.

4.2.4. *Diagonalization and solutions*

By virtue of the property of orthogonality, matrices **A** and **B** can be diagonalized using the modal matrix $\mathbf{\Phi}_d$ by

$$\mathbf{\Phi}_d^T \mathbf{A} \mathbf{\Phi}_d = \begin{bmatrix} a_1 & & 0 \\ & \ddots & \\ 0 & & a_{2n} \end{bmatrix} = \mathbf{\Lambda} \tag{56a}$$

$$\mathbf{\Phi}_d^T \mathbf{B} \mathbf{\Phi}_d = \begin{bmatrix} b_1 & & 0 \\ & \ddots & \\ 0 & & b_{2n} \end{bmatrix} = \mathbf{\Upsilon} \tag{56b}$$

using Eqs. (56a) and (56b) in Eqs. (52a) and (52b), for $r = s = k$, gives

$$\alpha_k = -\frac{b_k}{a_k} \tag{57}$$

The relation between the physical and modal domains is given by

$$\mathbf{y} = \mathbf{\Phi}_d \mathbf{q} \tag{58}$$

where the vector of the modal coordinates **q** is given by

$$\mathbf{q} = [\dot{q}_1 \;\; \dot{q}_2 \;\; \dot{q}_3 \;\; \dots \;\; \dot{q}_n \;\; q_1 \;\; q_2 \;\; q_3 \;\; \dots \;\; q_n]^T \tag{59}$$

and the expansion of Eq. (58) is

$$\begin{Bmatrix} \dot{x}_1 \\ \dot{x}_2 \\ \vdots \\ \dot{x}_n \\ x_1 \\ x_2 \\ \vdots \\ x_n \end{Bmatrix}_{2n\times 1} = \begin{bmatrix} \varphi_{11} & \varphi_{12} & \cdots & \varphi_{1,n} & \varphi_{1,n+1} & \varphi_{1,n+2} & \cdots & \varphi_{1,2n} \\ \varphi_{21} & \varphi_{22} & & & & & & \varphi_{2,2n} \\ \vdots & & \ddots & & \vdots & & & \vdots \\ \varphi_{n,1} & & & \varphi_{n,n} & \varphi_{n,n+1} & \cdots & & \varphi_{n,2n} \\ \varphi_{n+1,1} & & \cdots & \varphi_{n+1,n} & \varphi_{n+1,n+1} & & & \varphi_{n+1,2n} \\ \varphi_{n+2,1} & & & \vdots & & \varphi_{n+2,n+2} & & \varphi_{n+2,2n} \\ \vdots & & & & & & \ddots & \vdots \\ \varphi_{2n,1} & \varphi_{2n,2} & \cdots & \varphi_{2n,n} & \varphi_{2n,n+1} & \varphi_{2n,n+2} & \cdots & \varphi_{2n,2n} \end{bmatrix}_{2n\times 2n} \bullet \begin{Bmatrix} \dot{q}_1 \\ \dot{q}_2 \\ \vdots \\ \dot{q}_n \\ q_1 \\ q_2 \\ \vdots \\ q_n \end{Bmatrix}_{2n\times 1} \tag{60}$$

It is important to note that unlike the normal damping matrix (for systems that does not require state-space representation) the damped modal matrix has units for some of its terms, due to the presence of both displacement and velocity in the modal and physical domains. This feature is shown in Fig. 22 next

Figure 22 - units of the terms in the damped modal matrix in a case where the system is in state-space representation with the physical vector having displacements and velocities.

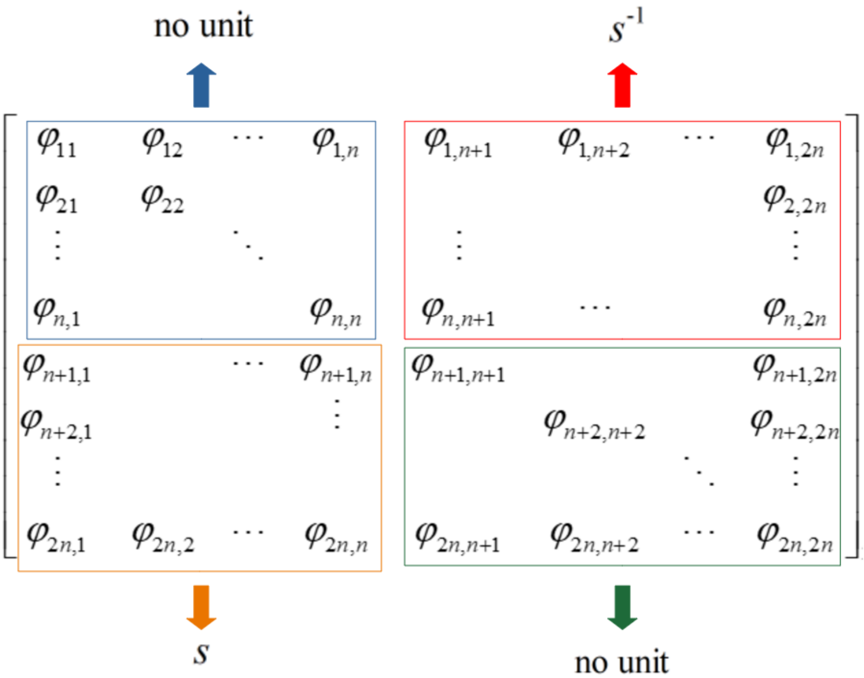

Source: elaborated by the author.

Referring to Eq. (43) and substituting the relation from Eq. (58) gives

$$\mathbf{A}\mathbf{\Phi}_d\dot{\mathbf{q}} + \mathbf{B}\mathbf{\Phi}_d\mathbf{q} = \mathbf{p} \tag{61}$$

Pre-multiplying both sides of Eq. (61) by $\mathbf{\Phi}_d^T$ gives

$$\mathbf{\Phi}_d^T \mathbf{A} \mathbf{\Phi}_d \dot{\mathbf{q}} + \mathbf{\Phi}_d^T \mathbf{B} \mathbf{\Phi}_d \mathbf{q} = \mathbf{\Phi}_d^T \mathbf{p} \tag{62}$$

using the relations from Eqs. (56a) and (56b), Eq. (62) can be rewritten as

$$\mathbf{\Lambda} \dot{\mathbf{q}} + \mathbf{\Upsilon} \mathbf{q} = \mathbf{\Phi}_d^T \mathbf{p} \tag{63}$$

where

$$\mathbf{\Lambda} = \begin{bmatrix} \lambda_1 & 0 & \cdots & 0 \\ 0 & \lambda_2 & & \vdots \\ \vdots & & \ddots & 0 \\ 0 & \cdots & 0 & \lambda_{2n} \end{bmatrix} \tag{64a}$$

$$\mathbf{\Upsilon} = \begin{bmatrix} \upsilon_1 & 0 & \cdots & 0 \\ 0 & \upsilon_2 & & \vdots \\ \vdots & & \ddots & 0 \\ 0 & \cdots & 0 & \upsilon_{2n} \end{bmatrix} \tag{64b}$$

$$\mathbf{\Phi}_d^T \mathbf{p} = \begin{Bmatrix} \varphi_{n+1,1} m_1 g + \varphi_{n+2,1} m_2 g + \varphi_{n+3,1} m_3 g + \ldots + \varphi_{2n,1} m_n g \\ \varphi_{n+1,2} m_1 g + \varphi_{n+2,2} m_2 g + \varphi_{n+3,2} m_3 g + \ldots + \varphi_{2n,2} m_n g \\ \varphi_{n+1,3} m_1 g + \varphi_{n+2,3} m_2 g + \varphi_{n+3,3} m_3 g + \ldots + \varphi_{2n,3} m_n g \\ \vdots \\ \varphi_{n+1,2n} m_1 g + \varphi_{n+2,2n} m_2 g + \varphi_{n+3,2n} m_3 g + \ldots + \varphi_{2n,2n} m_n g \end{Bmatrix} \tag{64c}$$

Eq. (63) represents a system of $2n$ uncoupled differential equations, where $q_1, q_2, q_3, \ldots, q_{2n}$ (modal coordinates) are the independent variables. The initial conditions for the modal coordinates vector can be obtained through

$$\mathbf{q}_0 = \mathbf{\Phi}_d^{-1} \mathbf{y}_0 \tag{65}$$

Defining

$$\mathbf{h} = \mathbf{\Phi}_d^T \mathbf{p} = \{h_1 \ h_2 \ h_3 \ \dots \ h_{2n}\}^T \tag{66}$$

The uncoupled differential equations resulting from the system in Eq. (63) can be represented as Eqs. (67) and (68):

$$\lambda_k \ddot{q}_k + \upsilon_k \dot{q}_k = h_k \qquad k = 1, 2, 3, \dots, n \tag{67}$$

$$\lambda_k \dot{q}_{k-n} + \upsilon_k q_{k-n} = h_k \qquad k = n+1, n+2, n+3, \dots, 2n \tag{68}$$

Note that Eqs. (67) and (68) are first order equations, where Eq. (67) is a first order equation in relation to velocity and Eq. (68) is a first order equation in relation to displacement. Solving for q_{k-n}. Solving Eqs. (67) and (68) gives

$$\dot{q}_k = \dot{q}_{0k} e^{\alpha_k t} + \left(1 - e^{\alpha_k t}\right) \frac{h_k}{\upsilon_k} \qquad k = 1, 2, 3, \dots, n \tag{69}$$

and

$$q_{k-n} = q_{0k-n} e^{\alpha_k t} + \left(1 - e^{\alpha_k t}\right) \frac{h_k}{\upsilon_k} \qquad k = n+1, n+2, n+3, \dots, 2n \tag{70}$$

or using a condensed matrix equation, Eqs. (69) and (70) can be rewritten as

$$\mathbf{q} = \mathbf{K}\mathbf{q}_0 + \mathbf{\Upsilon}^{-1}\left[\mathbf{I} - \mathbf{K}\right]\mathbf{h} \tag{71}$$

where $\mathbf{K} = \mathrm{diag}\left(e^{\alpha_i t}\right)$ and $\mathbf{q}_0 = \mathbf{\Phi}_d^{-1}\mathbf{y}_0$. After obtaining the modal displacements (q_k) and velocities ($\dot{q}_k$), the state vector **y** (physical coordinates) can be obtained through Eq. (58).

4.2.5. System simplification

It is important to note that using the expansion from Eq. (60), the physical displacements and velocities from vector **y** can be divided into the contributions of each mode of vibration. For underdamped modes, the contribution of the *i*-th over the *jj*-th physical displacement x_{jj} is given by

$$x_{jj,i} = \varphi_{n+1+jj,i} q_i + \varphi^*_{n+1+jj,i} q^*_i \tag{72}$$

where (*) denote the complex conjugate. If q_i is a velocity, q^*_i can be a velocity or a displacement, and if q_i is a displacement, q^*_i is a displacement as well. For overdamped modes, the contribution of the *i*-th to the *jj*-th physical displacement x_j is given by

$$x_{jj,i} = \varphi_{n+1+jj,m} q_m + \varphi_{n+1+jj,n} q_n \tag{73}$$

where *m* and *n* are the pair that forms the *i*-th mode, considering that the mode contributions are displayed separated by pairs of coordinates. Again, if q_m is a velocity, q_n can be a velocity or a displacement, and if q_m is a displacement, q_n is a displacement as well. Now considering a *i*-th underdamped mode has the form of Eq. (72), with $q_i = q_{0i} e^{\alpha_i t} + \left(1 - e^{\alpha_i t}\right)\left(h_i / \upsilon_i\right)$ and $q^*_i = q^*_{0i} e^{\alpha^*_i t} + \left(1 - e^{\alpha^*_i t}\right)\left(h^*_i / \upsilon^*_i\right)$. Equation (72) can then be written as

$$x_{jj,i} = A_{jj,i} e^{\alpha_i t} + B_{jj,i} + A^*_{jj,i} e^{\alpha^*_i t} + B^*_{jj,i} \tag{74}$$

where

$$A_{jj,i} = \varphi_{n+1+jj,i} \left(q_{0i} - \frac{h_i}{\upsilon_i} \right) \tag{75a}$$

$$B_{jj,i} = \varphi_{n+1+jj,i} \frac{h_i}{\upsilon_i} \tag{75b}$$

$$A^*_{jj,i} = \varphi^*_{n+1+jj,i} \left(q^*_{0i} - \frac{h^*_i}{\upsilon^*_i} \right) \tag{75c}$$

$$B^*_{jj,i} = \varphi^*_{n+1+jj,i} \frac{h^*_i}{\upsilon^*_i} \tag{75d}$$

Noting that $\alpha_i = \mathrm{Re}\{\alpha_i\} + j\mathrm{Im}\{\alpha_i\}$ for an underdamped mode ($\mathrm{Re}\{\alpha_i\}$ stands for the real part of α_i $\mathrm{Im}\{\alpha_i\}$ and stands for the imaginary part of α_i), Eq. (74) can also be written as

$$x_{jj,i} = e^{\mathrm{Re}\{\alpha_i\}t}\left(A_{jj,i}e^{\mathrm{jIm}\{\alpha_i\}t} + A^*_{jj,i}e^{-\mathrm{jIm}\{\alpha_i\}t}\right) + 2\,\mathrm{Re}\left\{B_{jj,i}\right\} \tag{76}$$

Using Euler's equation, Eq. (76) can be written in terms of trigonometric functions as

$$x_{jj,i} = 2e^{\mathrm{Re}\{\alpha_i\}t}\left(\mathrm{Re}\left\{A_{jj,i}\right\}\cos\omega_i t - \mathrm{Im}\left\{A_{jj,i}\right\}\sin\omega_i t\right) + 2\,\mathrm{Re}\left\{B_{jj,i}\right\} \tag{77}$$

The GRF is thus given by combining Eqs. (28) and (77) to give

$$F_i = e^{\mathrm{Re}\{\alpha_i\}t}\left(C_i\cos\omega_i t - D_i\sin\omega_i t\right) + E_i \quad \text{for } t \geq 0 \tag{78}$$

where

$$C_i = 2k_0\,\mathrm{Re}\left\{A_{0,i}\right\} + 2k_{01}\,\mathrm{Re}\left\{A_{1,i}\right\} \tag{79a}$$

$$D_i = 2k_0\,\mathrm{Im}\left\{A_{0,i}\right\} + 2k_{01}\,\mathrm{Im}\left\{A_{1,i}\right\} \tag{79b}$$

$$E_i = 2k_0\,\mathrm{Re}\left\{B_{0,i}\right\} + 2k_{01}\,\mathrm{Re}\left\{B_{1,i}\right\} \tag{79c}$$

Equation (78) can be further simplified to

$$F_i = G_i e^{\mathrm{Re}\{\alpha_i\}t}\sin\left(\omega_i t + \phi_i\right) + E_i \quad \text{for } t \geq 0 \tag{80}$$

where $G_i = 2\sqrt{C_i^2 + D_i^2}$ and $\phi_i = \tan^{-1}\left(C_i / D_i\right)$. Thus, a component of the GRF due to an oscillatory mode is given by a damped sinusoid with a time shift and an offset.

Now considering the *k*-th overdamped mode. The effect of the mode on the displacement x_{jj} is given by

$$x_{jj,k} = A_{jj,m}e^{\alpha_m t} + A_{jj,n}e^{\alpha_n t} + B_{jj,m} + B_{jj,n} \tag{81}$$

where the indices m and n correspond to the pair that forms the mode. The GRF due to the k-th mode is then obtained by combining Eqs. (28) and (81) to give

$$F_k = Se^{\alpha_m t} + Te^{\alpha_n t} + U \quad \text{for } t \geq 0 \tag{82a}$$

where

$$S = k_0 A_{i,m} + k_{01} A_{jj,m} \tag{82b}$$

$$T = k_0 A_{i,n} + k_{01} A_{jj,n} \tag{82c}$$

$$U = k_0 (B_{jj,m} + B_{jj,n}) + k_{01}(B_{jj,m} + B_{jj,n}) \tag{82d}$$

where the index jj refers to the x coordinates that forms the GRF in the model and i refers to the mode. The total ground reaction force can then be obtained by summing all the ground reaction force mode components (underdamped and overdamped) as follows

$$GRF_T = F_1 + F_2 + \cdots F_n \tag{83}$$

4.3. Five-DOF model application

The modal analysis procedure discussed in this chapter is applied to the five-DOF LPM discussed in chapter 3 (Fig. 20). The parameters from the ground contact portion of the model are the optimized parameters obtained the optimization in chapter 3 for the soft sole case. The model parameters are presented in Table 9.

Table 9 - Five-DOF model parameters for the modal analysis.

masses [kg]	springs [kN/m]	dampers [Ns/m]	touchdown velocities [m/s]
m_0 = 0.01	k_0 = 211.26	c_0 = 595.17	$v_0(0)$ = 0.96
m_1 = 6.15	k_{01} = 144.52	c_1 = 300	$v_1(0)$ = 0.96
m_2 = 6	k_1 = 6	c_2 = 650	$v_2(0)$ = 0.96
m_3 = 12.58	k_2 = 6	c_4 = 1900	$v_3(0)$ = 2
m_4 = 50.34	k_3 = 10		$v_4(0)$ = 2
	k_4 = 10		
	k_5 = 18		

Source: elaborated by the author.

The initial displacements are all zero. The system of equations of motion have then the form of

$$\mathbf{M}_{5D}\ddot{\mathbf{x}}_{5D} + \mathbf{C}_{5D}\dot{\mathbf{x}}_{5D} + \mathbf{K}_{5D}\mathbf{x}_{5D} = \mathbf{f}_{5D} \tag{84}$$

where

$$\mathbf{M}_{5D} = \begin{bmatrix} m_0 & 0 & 0 & 0 & 0 \\ 0 & m_1 & 0 & 0 & 0 \\ 0 & 0 & m_2 & 0 & 0 \\ 0 & 0 & 0 & m_3 & 0 \\ 0 & 0 & 0 & 0 & m_4 \end{bmatrix}, \mathbf{C}_{5D} = \begin{bmatrix} c_0 & -c_0 & 0 & 0 & 0 \\ -c_0 & c_0 + c_1 + c_2 & -c_2 & -c_1 & 0 \\ 0 & -c_2 & c_2 & 0 & 0 \\ 0 & -c_1 & 0 & c_1 + c_4 & -c_4 \\ 0 & 0 & 0 & -c_4 & c_4 \end{bmatrix} \text{ and}$$

$$\mathbf{K}_5 = \begin{bmatrix} k_0 & 0 & 0 & 0 & 0 \\ 0 & k_{01} + k_1 + k_2 & -k_2 & -k_1 & 0 \\ 0 & -k_2 & k_2 + k_3 & -k_3 & 0 \\ 0 & -k_1 & -k_3 & k_1 + k_3 + k_4 + k_5 & -k_4 - k_5 \\ 0 & 0 & 0 & -k_4 - k_5 & k_4 + k_5 \end{bmatrix}$$

The vector of responses $\mathbf{x}_{5D}$ is given by $\mathbf{x}_{5D} = \{x_0, \quad x_1, \quad x_2, \quad x_3, \quad x_4,\}^T$ where T denotes the transpose, and the vector of forces $\mathbf{f}_{5D}$ is given by $\mathbf{f}_{5D} = \{m_0 g, \quad m_1 g, \quad m_2 g, \quad m_3 g, \quad m_4 g,\}^T$. Following the modal analysis methodology, a state vector containing the displacements and velocities is defined as follows

$$\mathbf{y}_{5D} = \{\dot{x}_0 \ \dot{x}_1 \ \dot{x}_2 \ \dot{x}_3 \ \dot{x}_4 \ x_0 \ x_1 \ x_2 \ x_3 \ x_4\}^T \tag{85}$$

Rearranging the system in Eq. (84) using Eq. (85) gives a new first order system of equations in the form of

$$\mathbf{A}_{5D}\dot{\mathbf{y}}_{5D} + \mathbf{B}_{5D}\mathbf{y}_{5D} = \mathbf{p}_{5D} \tag{86a}$$

$$\mathbf{A}_{5D} = \begin{bmatrix} \mathbf{0} & \mathbf{M}_{5D} \\ \mathbf{M}_{5D} & \mathbf{C}_{5D} \end{bmatrix} \tag{86b}$$

$$\mathbf{B}_{5D} = \begin{bmatrix} \mathbf{-M}_{5D} & \mathbf{0} \\ \mathbf{0} & \mathbf{K}_{5D} \end{bmatrix} \tag{86c}$$

$$\mathbf{p}_{5D} = \begin{Bmatrix} \mathbf{0} \\ \mathbf{f}_{5D} \end{Bmatrix} \tag{86d}$$

the eigenvalues and eigenvectors of the new systems are then obtained in Matlab. The software presents the eigenvalues in crescent absolute value order. Since this is not a proper order, the eigenvalues and corresponding eigenvectors are reordered so that the first modes represent the underdamped oscillating modes and the last modes represent the overdamped modes, as follows

$$\alpha_{5D,1} = -3.5 + j10.95 \tag{87a}$$

$$\alpha_{5D,2} = -3.5 - j10.95 \tag{87b}$$

$$\alpha_{5D,3} = -62.39 + j80.45 \tag{87c}$$

$$\alpha_{5D,4} = -62.39 - j80.45 \tag{87d}$$

$$\alpha_{5D,5} = -235.48 + j144.74 \tag{87e}$$

$$\alpha_{5D,6} = -235.48 - j144.74 \tag{87f}$$

$$\alpha_{5D,7} = -59258 \tag{87g}$$

$$\alpha_{5D,8} = -179.37 \tag{87h}$$

$$\alpha_{5D,9} = -33.79 \tag{87i}$$

$$\alpha_{5D,10} = -15.19 \tag{87j}$$

the corresponding eigenvectors are presented in the modal matrix in Appendix B. The natural parameters for the modes can be obtained through Eq. (49) (in case of underdamped modes) and are presented in Table 10.

Table 10 - five-DOF model modes natural parameters.

mode	damping factor	nautral frequency	damped natural frequency
first	ζ_1 = 0.3044	ω_{n1} = 1.83 Hz	ω_1 = 1.74 Hz
second	ζ_2 = 0.6105	ω_{n2} = 16.27 Hz	ω_2 = 12.88 Hz
third	ζ_3 = 0.8591	ω_{n3} = 43.99 Hz	ω_3 = 23.04 Hz
fourth	ζ_4 > 1	X	ω_4 = 0 Hz
fifth	ζ_5 > 1	X	ω_5 = 0 Hz

Source: elaborated by the author.

By examining the eigenvalues, it can be seen that the system has three oscillatory underdamped modes (three complex conjugate pairs) and two non-oscillatory overdamped modes (four real different values). Now the relation between the physical and modal domain can be defined using Eq. (58)

$$\mathbf{y}_{5D} = \mathbf{\Phi}_{5D,d}\mathbf{q}_{5D} \tag{88}$$

where

$$\mathbf{q}_{5D} = \{\dot{q}_0\ \dot{q}_1\ \dot{q}_2\ \dot{q}_3\ \dot{q}_4\ q_0\ q_1\ q_2\ q_3\ q_4\}^T \tag{89}$$

applying Eq. (88) to Eq. (86a) and pre-multiplying by $\mathbf{\Phi}_{5D,d}^T$ results in

$$\mathbf{\Lambda}_{5D}\dot{\mathbf{q}}_{5D} + \mathbf{\Upsilon}_{5D}\mathbf{q}_{5D} = \mathbf{\Phi}_{5D,d}^T\mathbf{p}_{5D} = \mathbf{h}_{5D} \tag{90}$$

using the information gathered from the eigenvectors and eigenvalues, the modes are divided as: first mode, second mode, third mode and overdamped mode. The overdamped mode includes both overdamped modes from the system. Using Eqs. (72) and (73) and grouping the overdamped modes, x_0 and x_1 can be defined with respect to the modal coordinates as follows

$$\mathbf{q}_{5D} = \left\{\begin{matrix} 1^{st}\text{ mode} & 2^{nd}\text{ mode} & 3^{rd}\text{ mode} & 4^{th}\text{ mode} & 5^{th}\text{ mode} \\ \dot{q}_0\ \dot{q}_1 & \dot{q}_2\ \dot{q}_3 & \dot{q}_4\ q_0 & q_1\ q_2 & q_3\ q_4 \\ & & & & \end{matrix}\right\}^T \tag{91a}$$

$$x_0^{\text{mod}1} = \varphi_{61}\dot{q}_0 + \varphi_{62}\dot{q}_1 \tag{91b}$$

$$x_0^{\text{mod}2} = \varphi_{63}\dot{q}_2 + \varphi_{64}\dot{q}_3 \tag{91c}$$

$$x_0^{\text{mod}3} = \varphi_{65}\dot{q}_4 + \varphi_{66}q_0 \tag{91d}$$

$$x_0^{\text{ovd}} = \varphi_{67}q_1 + \varphi_{68}q_2 + \varphi_{69}q_3 + \varphi_{6,10}q_4 \tag{91e}$$

$$x_1^{\text{mod}1} = \varphi_{71}\dot{q}_0 + \varphi_{72}\dot{q}_1 \tag{91f}$$

$$x_1^{\mathrm{mod}\,2} = \varphi_{73}\dot{q}_2 + \varphi_{74}\dot{q}_3 \tag{91g}$$

$$x_1^{\mathrm{mod}\,3} = \varphi_{75}\dot{q}_4 + \varphi_{76}q_0 \tag{91h}$$

$$x_1^{\mathrm{ovd}} = \varphi_{77}q_1 + \varphi_{78}q_2 + \varphi_{79}q_3 + \varphi_{7,10}q_4 \tag{91i}$$

Note that time dependency is assumed but is not shown for simplicity. Now the expansion and simplification of Eqs. (91b) to (91i) is performed using the system simplification methodology discussed. The expansion is exemplified for the first mode, and then expanded to all the other underdamped modes for simplicity. First, using Eq. (74) to expand the first mode contribution of x_0 and x_1 as follows

$$x_0^{\mathrm{mod}1} = A_{0,1}e^{\alpha_{5D,1}t} + B_{0,1} + A_{0,1}^{*}e^{\alpha_{5D,2}t} + B_{0,1}^{*} \tag{92a}$$

$$x_1^{\mathrm{mod}1} = A_{1,1}e^{\alpha_{5D,1}t} + B_{1,1} + A_{1,1}^{*}e^{\alpha_{5D,2}t} + B_{1,1}^{*} \tag{92b}$$

where

$$A_{0,1} = \varphi_{61}\left(\dot{q}_0(0) - \frac{h_1}{\upsilon_1}\right) \tag{93a}$$

$$B_{0,1} = \frac{\varphi_{61}h_1}{\upsilon_1} \tag{93b}$$

$$A_{0,1}^{*} = \varphi_{62}\left(\dot{q}_1(0) - \frac{h_2}{\upsilon_2}\right) \tag{93c}$$

$$B_{0,1}^{*} = \frac{\varphi_{62}h_2}{\upsilon_2} \tag{93d}$$

$$A_{1,1} = \varphi_{71}\left(\dot{q}_0(0) - \frac{h_1}{\upsilon_1}\right) \tag{93e}$$

$$B_{1,1} = \frac{\varphi_{71}h_1}{\upsilon_1} \tag{93f}$$

$$A_{1,1}^{*} = \varphi_{72}\left(\dot{q}_1(0) - \frac{h_2}{\upsilon_2}\right) \tag{93g}$$

$$B_{1,1}^{*} = \frac{\varphi_{72}h_2}{\upsilon_2} \tag{93h}$$

and then the GRF component related to the first mode is given by

$$F_{5D}^{\mathrm{mod}1} = G_{5D,1} e^{\mathrm{Re}\{\alpha_{5D,1}\}t} \sin\left(\omega_{5D,1} t + \phi_{5D,1}\right) + E_{5D,1} \tag{94}$$

where

$$G_{5D,1} = 2\sqrt{C_{5D,1}^2 + D_{5D,1}^2} \tag{95a}$$

$$\phi_{5D,1} = \tan^{-1}\left(\frac{-C_{5D,1}}{D_{5D,1}}\right) \tag{95b}$$

$$E_{5D,1} = 2k_0 \,\mathrm{Re}\left\{B_{0,1}\right\} + 2k_{01} \,\mathrm{Re}\left\{B_{1,1}\right\} \tag{95c}$$

$$C_{5D,1} = 2k_0 \,\mathrm{Re}\left\{A_{0,1}\right\} + 2k_{01} \,\mathrm{Re}\left\{A_{1,1}\right\} \tag{95d}$$

$$D_{5D,1} = 2k_0 \,\mathrm{Im}\left\{A_{0,1}\right\} + 2k_{01} \,\mathrm{Im}\left\{A_{1,1}\right\} \tag{95e}$$

Similarly, the second mode component is given by

$$F_{5D}^{\mathrm{mod}2} = G_{5D,2} e^{\mathrm{Re}\{\alpha_{5D,2}\}t} \sin\left(\omega_{5D,2} t + \phi_{5D,2}\right) + E_{5D,2} \tag{96}$$

where

$$G_{5D,2} = 2\sqrt{C_{5D,2}^2 + D_{5D,2}^2} \tag{97a}$$

$$\phi_{5D,2} = \tan^{-1}\left(\frac{-C_{5D,2}}{D_{5D,2}}\right) \tag{97b}$$

$$E_{5D,2} = 2k_0 \,\mathrm{Re}\left\{B_{0,2}\right\} + 2k_{01} \,\mathrm{Re}\left\{B_{1,2}\right\} \tag{97c}$$

$$C_{5D,2} = 2k_0 \,\mathrm{Re}\left\{A_{0,2}\right\} + 2k_{01} \,\mathrm{Re}\left\{A_{1,2}\right\} \tag{97d}$$

$$D_{5D,2} = 2k_0 \,\mathrm{Im}\left\{A_{0,2}\right\} + 2k_{01} \,\mathrm{Im}\left\{A_{1,2}\right\} \tag{97e}$$

the third mode component is given by

$$F_{5D}^{\mathrm{mod}3} = G_{5D,3} e^{\mathrm{Re}\{\alpha_{5D,3}\}t} \sin\left(\omega_{5D,3} t + \phi_{5D,3}\right) + E_{5D,3} \tag{98}$$

where

$$G_{5D,3} = 2\sqrt{C_{5D,3}^2 + D_{5D,3}^2} \tag{99a}$$

$$\phi_{5D,3} = \tan^{-1}\left(\frac{-C_{5D,3}}{D_{5D,3}}\right) \tag{99b}$$

$$E_{5D,3} = 2k_0 \,\mathrm{Re}\left\{B_{0,3}\right\} + 2k_{01} \,\mathrm{Re}\left\{B_{1,3}\right\} \tag{99c}$$

$$C_{5D,3} = 2k_0 \,\mathrm{Re}\left\{A_{0,3}\right\} + 2k_{01} \,\mathrm{Re}\left\{A_{1,3}\right\} \tag{99d}$$

$$D_{5D,3} = 2k_0 \,\mathrm{Im}\left\{A_{0,3}\right\} + 2k_{01} \,\mathrm{Im}\left\{A_{1,3}\right\} \tag{99e}$$

Expanding the overdamped mode contribution of x_0 and x_1 as follows

$$x_0^{ovd} = A_{0,7} e^{\alpha_{5D,7}t} + B_{0,7} + A_{0,8} e^{\alpha_{5D,8}t} + B_{0,8} + A_{0,9} e^{\alpha_{5D,9}t} + B_{0,9} + A_{0,10} e^{\alpha_{5D,10}t} + B_{0,10} \tag{100a}$$

$$x_1^{ovd} = A_{1,7} e^{\alpha_{5D,7}t} + B_{1,7} + A_{1,8} e^{\alpha_{5D,8}t} + B_{1,8} + A_{1,9} e^{\alpha_{5D,9}t} + B_{1,9} + A_{1,10} e^{\alpha_{5D,10}t} + B_{1,10} \tag{100b}$$

where

$$A_{0,7} = \varphi_{67}\left(q_1(0) - \frac{h_7}{\upsilon_7}\right) \tag{101a}$$

$$B_{0,7} = \frac{\varphi_{67} h_7}{\upsilon_7} \tag{101b}$$

$$A_{0,8} = \varphi_{68}\left(q_2(0) - \frac{h_8}{\upsilon_8}\right) \tag{101c}$$

$$B_{0,8} = \frac{\varphi_{68} h_8}{\upsilon_8} \tag{101d}$$

$$A_{0,9} = \varphi_{69}\left(q_3(0) - \frac{h_9}{\upsilon_9}\right) \tag{101e}$$

$$B_{0,9} = \frac{\varphi_{69} h_9}{\upsilon_9} \tag{101f}$$

$$A_{0,10} = \varphi_{6,10}\left(q_4(0) - \frac{h_{10}}{\upsilon_{10}} \right) \tag{101g}$$

$$B_{0,10} = \frac{\varphi_{6,10} h_{10}}{\upsilon_{10}} \tag{101h}$$

$$A_{1,7} = \varphi_{77}\left(q_1(0) - \frac{h_7}{\upsilon_7} \right) \tag{101i}$$

$$B_{1,7} = \frac{\varphi_{77} h_7}{\upsilon_7} \tag{101j}$$

$$A_{1,8} = \varphi_{78}\left(q_2(0) - \frac{h_8}{\upsilon_8} \right) \tag{101k}$$

$$B_{1,8} = \frac{\varphi_{78} h_8}{\upsilon_8} \tag{101l}$$

$$A_{1,9} = \varphi_{79}\left(q_3(0) - \frac{h_9}{\upsilon_9} \right) \tag{101m}$$

$$B_{1,9} = \frac{\varphi_{79} h_9}{\upsilon_9} \tag{101n}$$

$$A_{1,10} = \varphi_{7,10}\left(q_4(0) - \frac{h_{10}}{\upsilon_{10}} \right) \tag{101o}$$

$$B_{1,10} = \frac{\varphi_{7,10} h_{10}}{\upsilon_{10}} \tag{101p}$$

combining Eqs. (30), (100a) and (100b) gives

$$F_{5D}^{ovd} = P_{5D} e^{\alpha_{5D,7} t} + R_{5D} e^{\alpha_{5D,8} t} + S_{5D} e^{\alpha_{5D,9} t} + T_{5D} e^{\alpha_{5D,10} t} + U_{5D} \tag{102}$$

where

$$P_{5D} = k_0 A_{0,7} + k_{01} A_{1,7} \tag{103a}$$

$$R_{5D} = k_0 A_{0,8} + k_{01} A_{1,8} \tag{103b}$$

$$S_{5D} = k_0 A_{0,9} + k_{01} A_{1,9} \tag{103c}$$

$$T_{5D} = k_0 A_{0,10} + k_{01} A_{1,10} \tag{103d}$$

$$U_{5D} = k_0(B_{0,7} + B_{0,8} + B_{0,9} + B_{0,10}) + k_{01}(B_{1,7} + B_{1,8} + B_{1,9} + B_{1,10}) \tag{103e}$$

The total GRF is obtained then by summing all the modal components:

$$GRF_{5D} = F_{5D}^{\mathrm{mod}1} + F_{5D}^{\mathrm{mod}2} + F_{5D}^{\mathrm{mod}3} + F_{5D}^{ovd} \tag{104}$$

Figure 23a shows the comparison between the GRF obtained through the modal analysis procedure and the GRF obtained numerically. The numerical solution was obtained by solving the first order system of equations of the model

$$\dot{\mathbf{y}}_{5D} = \mathbf{A}_{5D}^{-1}\mathbf{g}_{5D} - \mathbf{A}_{5D}^{-1}\mathbf{B}_{5D}\mathbf{y}_{5D} \tag{105}$$

The solution of Eq. (105) is obtained numerically through 4th order Runge-Kutta method. Figure 1a shows the comparison between the numerical GRF solution compared to the GRF through the modal analysis procedure. Figure 23b shows the GRF obtained through the modal analysis procedure and the all the modes components of the GRF.

Figure 23 - a) comparison between numerical (▬▬) and modal analysis' (······) GRF solutions; b) total GRF (▬▬) compared to the first (▬ ▬), second (▬▬▬), third (······) and overdamped (▬ · ▬) modes.

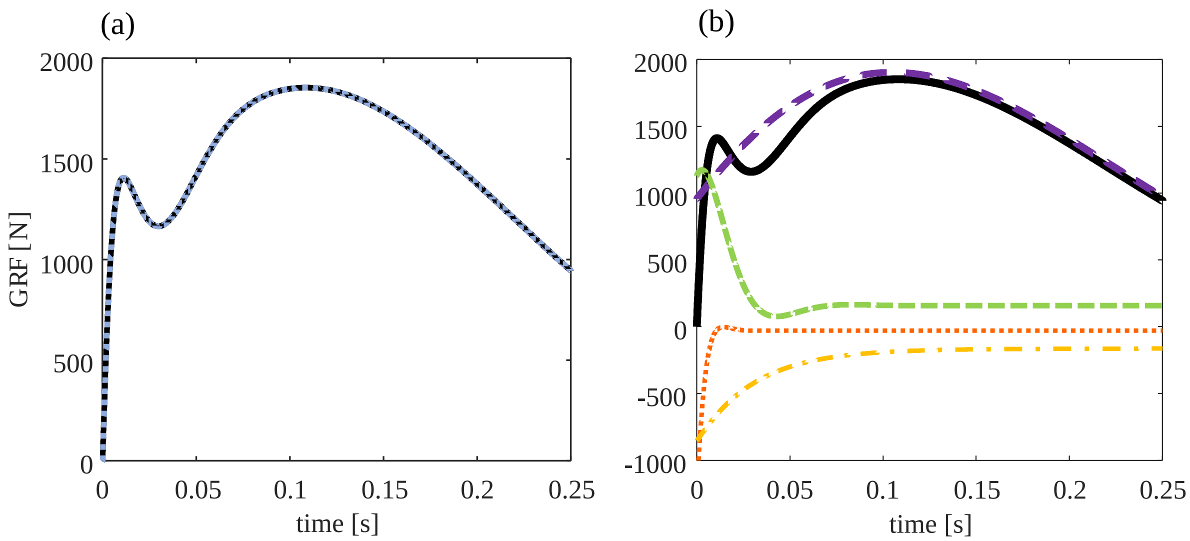

Source: elaborated by the author.

It is possible to see in Fig. 23a that the GRF solution obtained through the modal analysis matches the numerical solution and thus the modal analysis procedure is validated. The mode components in Fig. 23b show that the first mode has contribution over the whole stance phase and is mainly responsible for the active peak region of the GRF. The shape of the first mode GRF is similar to the upper body impulse forces presented in Clark *et al*. (2014) and Clark *et al*. (2017). The second mode also has influence over the entire stance phase, but mainly at the beginning (0 to 0.07s approximately) being mainly responsible for the impact peak and asymptotes to roughly 200N in the latter part. The shape of the second mode GRF is similar to the lower body impulse forces presented in Clark *et al*. (2014) and Clark *et al*. (2017). The third mode component has effect only in the very beginning of the stance phase (does not have a large effect over the total GRF). The summed overdamped modes have a greater effect at the beginning of the stance phase (0 to 0.1s roughly) and asymptotes to approximately -150N. The results from Fig. 1b show that two underdamped modes plus one overdamped mode may be enough to properly model a GRF, which suggests that a simpler model (three-DOF for example) may be used to simulate properly the running GRF.

4.4. Three-DOF model application

The general modal analysis procedure discussed in this chapter is now applied to a three-DOF proposed model.

4.4.1. Three-DOF model characterization

The proposed three-DOF model is an adaptation of the two-DOF model proposed by Derrick *et al*. (2000). The adaptation consists in using again the AZM as a ground contact model. Figure 24 shows the configuration of the three-DOF proposed LPM used to simulate the GRF.

Figure 24 - Configuration of the three-DOF proposed model.

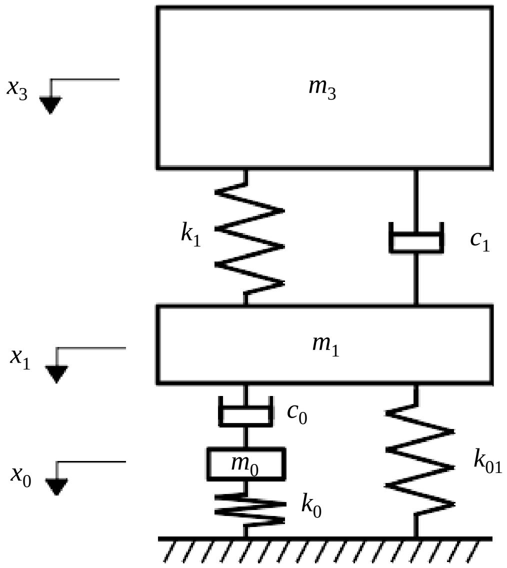

Source: elaborated by the author.

The three masses are connected through springs and dampers, which represent the viscoelastic elements of the human body. The rigid mass m_3 represents the upper body mass and is connected to the mass m_1 (lower body mass) through the spring k_1 and the damper c_1. The mass m_1 is connected to the ground through the spring k_{01} and connected to the small mass m_0 through the damper c_0. The mass m_0 is also connected to the ground through the spring k_0. To verify if the model can simulate the NLM's GRF, an optimization procedure is performed to find the best model parameters for that purpose.

4.4.2. Parameter optimization

The optimization procedure performed earlier (pattern search) is used now to find the best k_0, k_{01}, k_1, c_0, c_1 and m_1 / m_T for the model to match the NLM's GRF for soft and hard sole cases. The body total mass (m_T) is 75.08kg and the small mass (m_0) is 0.01kg. The initial conditions for the numerical solution of the equations of motions are $\dot{x}_0(0) = 0.96$, $\dot{x}_1(0) = 0.96$, $\dot{x}_3(0) = 2$ m/s for velocities and $x(0) = 0$ for all displacements. Figures 25a and 25b present the comparison between NLM and the proposed three-DOF model with optimized parameters for soft and hard sole conditions, respectively.

Figure 25 - Comparison between NLM's GRF (▬▬) to the three-DOF proposed GRF (▪▪▪▪▪) for (a) soft sole and (b) hard sole condition.

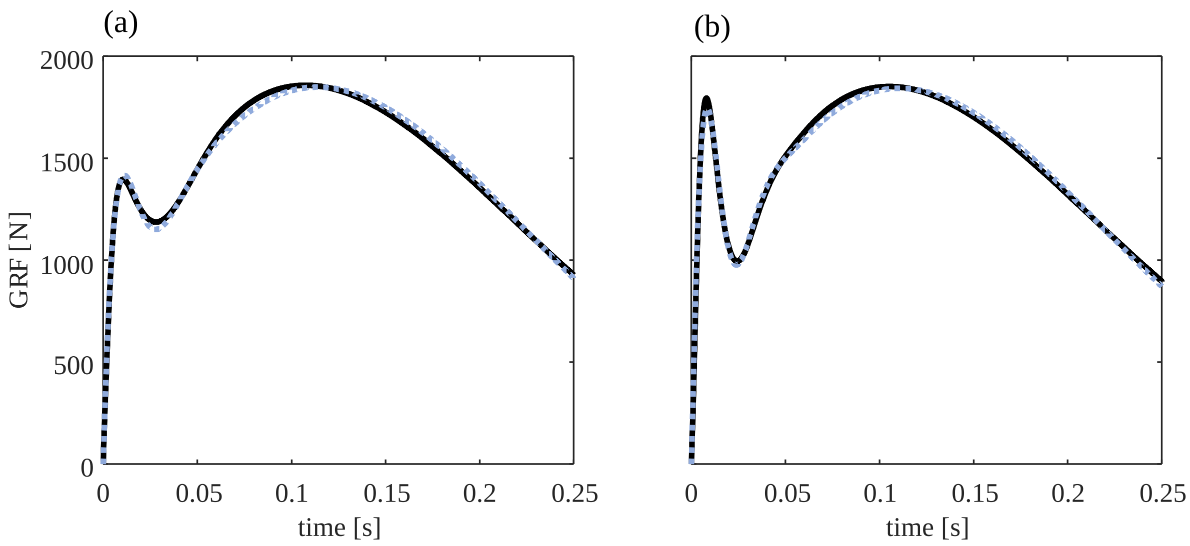

Source: elaborated by the author.

Figures 25a and 25b show that the three-DOF model with optimized parameters can replicate the NLM's GRF with good accuracy (RMSE = 1.43% for soft sole and RMSE = 1.43% for hard sole). Table 11 presents the optimized parameters for the proposed three-DOF model in soft and hard sole conditions.

Table 11 - optimized parameters for the three-DOF proposed model in soft and hard sole conditions.

	k_0 [kN/m]	k_{01} [kN/m]	k_1 [kN/m]	c_0 [Ns/m]	c_1 [kg/s]	m_1/m_T
soft sole	324.13	19.58	13.25	1628.5	369.02	0.2145
hard sole	474.03	19.88	12.41	2540.8	359.8	0.1866

Source: elaborated by the author.

The upper body mass m_3 is then obtained by subtraction of the total body mass

$$m_3 = m_T - m_0 - m_1 \tag{105}$$

Now the modal analysis procedure is applied to the proposed three-DOF model.

4.4.3. Modal Analysis

The modal analysis procedure is now applied to the proposed three-DOF model with optimized parameters for soft sole condition. The model parameters and initial conditions are presented in Table 12.

Table 12 - Three-DOF mode parameters used in the modal analysis.

masses [kg]	springs [kN/m]	dampers [kg/s]	touchdown velocities [m/s]
m_0 = 0.01	k_0 = 324.13	c_0 = 1628.50	$v_0(0)$ = 0.96
m_1 = 16.11	k_{01} = 19.58	c_1 = 369.02	$v_1(0)$ = 0.96
m_3 = 58.96	k_1 = 13.25		$v_3(0)$ = 2

Source: elaborated by the author.

The initial displacements are all zero. The model's system that contains equations of motion in matrix form can then be defined as

$$\mathbf{M}_{3D}\ddot{\mathbf{x}}_{3D} + \mathbf{C}_{3D}\dot{\mathbf{x}}_{3D} + \mathbf{K}_{3D}\mathbf{x}_{3D} = \mathbf{f}_{3D} \tag{106}$$

where

$$\mathbf{M}_{3D} = \begin{bmatrix} m_0 & 0 & 0 \\ 0 & m_1 & 0 \\ 0 & 0 & m_3 \end{bmatrix},\ \mathbf{C}_{3D} = \begin{bmatrix} c_0 & -c_0 & 0 \\ -c_0 & c_0 + c_1 & -c_1 \\ 0 & -c_1 & c_1 \end{bmatrix} \text{ and } \mathbf{K}_{3D} = \begin{bmatrix} k_0 & 0 & 0 \\ 0 & k_{01} + k_1 & -k_1 \\ 0 & -k_1 & k_1 \end{bmatrix}$$

The vector of responses $\mathbf{x}_{3D}$ is given by $\mathbf{x}_{3D} = \{x_0,\ x_1,\ x_3\}^T$ where T denotes the transpose and the vector of forces $\mathbf{f}_{3D}$ is given by $\mathbf{f}_{3D} = \{m_0 g,\ m_1 \mathrm{g},\ m_3 g\}^T$.

Following the modal analysis general procedure, a state vector is defined containing the displacements and velocities

$$\mathbf{y}_{3D} = \{\dot{x}_0\ \dot{x}_1\ \dot{x}_3\ x_0\ x_1\ x_3\}^T \tag{107}$$

Rearranging the system in Eq. (106) using Eq. (107) gives a new first order system in the form of

$$\mathbf{A}_{3D}\dot{\mathbf{y}}_{3D} + \mathbf{B}_{3D}\mathbf{y}_{3D} = \mathbf{p}_{3D} \tag{108a}$$

$$\mathbf{A}_{3D} = \begin{bmatrix} \mathbf{0} & \mathbf{M}_{3D} \\ \mathbf{M}_{3D} & \mathbf{C}_{3D} \end{bmatrix} \tag{108b}$$

$$\mathbf{B}_{3D} = \begin{bmatrix} \mathbf{-M}_{3D} & \mathbf{0} \\ \mathbf{0} & \mathbf{K}_{3D} \end{bmatrix} \tag{108c}$$

$$\mathbf{p}_{3D} = \begin{Bmatrix} \mathbf{0} \\ \mathbf{f}_{3D} \end{Bmatrix} \tag{108d}$$

the eigenvalues and eigenvectors of the new systems are then obtained in Matlab. The software presents the eigenvalues in crescent absolute value order. Since this is not a proper order, the eigenvalues and corresponding eigenvectors are reordered so that the first modes represent the underdamped oscillating modes and the last mode represent the overdamped mode, as follows

$$\alpha_{3D,1} = -3.28 + j11.54 \tag{109a}$$

$$\alpha_{3D,2} = -3.28 - j11.54 \tag{109b}$$

$$\alpha_{3D,3} = -102.70 + j112.83 \tag{109c}$$

$$\alpha_{3D,4} = -102.70 + j112.83 \tag{109d}$$

$$\alpha_{3D,5} = -162750 \tag{109e}$$

$$\alpha_{3D,6} = -16.22 \tag{109f}$$

the corresponding eigenvectors are presented in the modal matrix in Appendix B. The natural parameters for the modes can be obtained through Eq. (49) (in case of underdamped modes) and are presented in Table 13.

Table 13 - Three-DOF model modes natural parameters.

mode	damping factor	nautral frequency	damped natural frequency
first	ζ_1 = 0.2733	ω_{n1} = 1.91 Hz	ω_1 = 1.84 Hz
second	ζ_2 = 0.6577	ω_{n2} = 25.08 Hz	ω_2 = 17.96 Hz
third	ζ_3 > 1	X	ω_3 = 0 Hz

Source: elaborated by the author.

By examining the eigenvalues, it can be seen that the system has two oscillatory underdamped modes (two complex conjugate pairs) and a non-oscillatory overdamped mode (two real different values). Now the relation between the physical and modal domain can be defined using Eq. (58)

$$\mathbf{y}_{3D} = \mathbf{\Phi}_{3D,d}\mathbf{q}_{3D} \tag{110}$$

where

$$\mathbf{q}_{3D} = \left\{\dot{q}_0 \ \dot{q}_1 \ \dot{q}_3 \ q_0 \ q_1 \ q_3\right\}^T \tag{111}$$

applying Eq. (110) to Eq. (86a) and pre-multiplying by $\mathbf{\Phi}_{3D,d}^T$ results in

$$\mathbf{\Lambda}_{3D}\dot{\mathbf{q}}_{3D} + \mathbf{\Upsilon}_{3D}\mathbf{q}_{3D} = \mathbf{\Phi}_{3D,d}^T\mathbf{p}_{3D} = \mathbf{h}_{3D} \tag{112}$$

using the information gathered from the eigenvectors and eigenvalues, the modes are divided as: first mode, second mode and overdamped mode. Using Eqs. (72) and (73), x_0 and x_1 can be defined with respect to the modal coordinates as follows

$$\mathbf{q}_{3D} = \begin{Bmatrix} \overbrace{\dot{q}_0 \ \dot{q}_1}^{1^{\text{st}}\text{ mode}} & \overbrace{\dot{q}_3 \ q_0}^{2^{\text{nd}}\text{ mode}} & \overbrace{q_1 \ q_3}^{3^{\text{rd}}\text{ mode}} \end{Bmatrix}^T \tag{113a}$$

$$x_0^{\text{mod}1} = \varphi_{41}\dot{q}_0 + \varphi_{42}\dot{q}_1 \tag{113b}$$

$$x_0^{\text{mod}2} = \varphi_{43}\dot{q}_3 + \varphi_{44}q_0 \tag{113c}$$

$$x_0^{\text{ovd}} = \varphi_{45}q_1 + \varphi_{46}q_3 \tag{113d}$$

$$x_1^{\text{mod}1} = \varphi_{51}\dot{q}_0 + \varphi_{52}\dot{q}_1 \tag{113e}$$

$$x_1^{\text{mod}2} = \varphi_{53}\dot{q}_3 + \varphi_{54}q_0 \tag{113f}$$

$$x_1^{\text{ovd}} = \varphi_{55}q_1 + \varphi_{56}q_3 \tag{113g}$$

Note that time dependency is assumed but is not shown for simplicity. Now the expansion and simplification of Eqs. (113b) and (113e) is performed using the system simplification methodology discussed. The expansion is exemplified for the first mode, and then expanded to all the other underdamped modes for simplicity. First, using Eq. (74) to expand the first mode contribution of x_0 and x_1 as follows

$$x_0^{\mathrm{mod1}} = A_{0,1}e^{\alpha_{3D,1}t} + B_{0,1} + A_{0,1}^{*}e^{\alpha_{3D,2}t} + B_{0,1}^{*} \quad (114a)$$

$$x_1^{\mathrm{mod1}} = A_{1,1}e^{\alpha_{3D,1}t} + B_{1,1} + A_{1,1}^{*}e^{\alpha_{3D,2}t} + B_{1,1}^{*} \quad (114b)$$

where

$$A_{0,1} = \varphi_{41}\left(\dot{q}_0(0) - \frac{h_1}{\upsilon_1}\right) \quad (115a)$$

$$B_{0,1} = \frac{\varphi_{41}h_1}{\upsilon_1} \quad (115b)$$

$$A_{0,1}^{*} = \varphi_{42}\left(\dot{q}_1(0) - \frac{h_2}{\upsilon_2}\right) \quad (115c)$$

$$B_{0,1}^{*} = \frac{\varphi_{42}h_2}{\upsilon_2} \quad (115d)$$

$$A_{1,1} = \varphi_{51}\left(\dot{q}_0(0) - \frac{h_1}{\upsilon_1}\right) \quad (115e)$$

$$B_{1,1} = \frac{\varphi_{51}h_1}{\upsilon_1} \quad (115f)$$

$$A_{1,1}^{*} = \varphi_{52}\left(\dot{q}_1(0) - \frac{h_2}{\upsilon_2}\right) \quad (115g)$$

$$B_{1,1}^{*} = \frac{\varphi_{52}h_2}{\upsilon_2} \quad (115h)$$

and then the GRF component related to the first mode is given by

$$F_{3D}^{\mathrm{mod1}} = G_{3D,1}e^{\mathrm{Re}\{\alpha_{3D,1}\}t}\sin\left(\omega_{3D,1}t + \phi_{3D,1}\right) + E_{3D,1} \quad (116)$$

where

$$G_{3D,1} = 2\sqrt{C_{3D,1}^2 + D_{3D,1}^2} \tag{117a}$$

$$\phi_{3D,1} = \tan^{-1}\left(\frac{-C_{3D,1}}{D_{3D,1}}\right) \tag{117b}$$

$$E_{3D,1} = 2k_0 \operatorname{Re}\left\{B_{0,1}\right\} + 2k_{01} \operatorname{Re}\left\{B_{1,1}\right\} \tag{117c}$$

$$C_{3D,1} = 2k_0 \operatorname{Re}\left\{A_{0,1}\right\} + 2k_{01} \operatorname{Re}\left\{A_{1,1}\right\} \tag{117d}$$

$$D_{3D,1} = 2k_0 \operatorname{Im}\left\{A_{0,1}\right\} + 2k_{01} \operatorname{Im}\left\{A_{1,1}\right\} \tag{117e}$$

Similarly, the second mode component is given by

$$F_{3D}^{\mathrm{mod}\,2} = G_{3D,2} e^{\operatorname{Re}\left\{\alpha_{3D,2}\right\} t} \sin\left(\omega_{3D,2} t + \phi_{3D,2}\right) + E_{3D,2} \tag{118}$$

where

$$G_{3D,2} = 2\sqrt{C_{3D,2}^2 + D_{3D,2}^2} \tag{119a}$$

$$\phi_{3D,2} = \tan^{-1}\left(\frac{-C_{3D,2}}{D_{3D,2}}\right) \tag{119b}$$

$$E_{3D,2} = 2k_0 \operatorname{Re}\left\{B_{0,2}\right\} + 2k_{01} \operatorname{Re}\left\{B_{1,2}\right\} \tag{119c}$$

$$C_{3D,2} = 2k_0 \operatorname{Re}\left\{A_{0,2}\right\} + 2k_{01} \operatorname{Re}\left\{A_{1,2}\right\} \tag{119d}$$

$$D_{3D,2} = 2k_0 \operatorname{Im}\left\{A_{0,2}\right\} + 2k_{01} \operatorname{Im}\left\{A_{1,2}\right\} \tag{119e}$$

Expanding the overdamped mode contribution of x_0 and x_1 as follows

$$x_0^{ovd} = A_{0,5} e^{\alpha_{3D,5} t} + B_{0,5} + A_{0,6} e^{\alpha_{3D,6} t} + B_{0,6} \tag{120a}$$

$$x_1^{ovd} = A_{1,5} e^{\alpha_{3D,5} t} + B_{1,5} + A_{1,6} e^{\alpha_{3D,6} t} + B_{1,6} \tag{120b}$$

where

$$A_{0,5} = \varphi_{45}\left(q_1(0) - \frac{h_5}{\upsilon_5}\right) \quad (121a)$$

$$B_{0,5} = \frac{\varphi_{45}h_5}{\upsilon_5} \quad (121b)$$

$$A_{0,6} = \varphi_{46}\left(q_3(0) - \frac{h_6}{\upsilon_6}\right) \quad (121c)$$

$$B_{0,6} = \frac{\varphi_{46}h_6}{\upsilon_6} \quad (121d)$$

$$A_{1,5} = \varphi_{55}\left(q_1(0) - \frac{h_5}{\upsilon_5}\right) \quad (121e)$$

$$B_{1,5} = \frac{\varphi_{55}h_5}{\upsilon_5} \quad (121f)$$

$$A_{1,6} = \varphi_{56}\left(q_3(0) - \frac{h_6}{\upsilon_6}\right) \quad (121g)$$

$$B_{1,6} = \frac{\varphi_{56}h_6}{\upsilon_6} \quad (121h)$$

combining Eqs. (30), (120a) and (120b) gives

$$F_{3D}^{ovd} = S_{3D}e^{\alpha_{3D,5}t} + T_{3D}e^{\alpha_{3D,6}t} + U_{3D} \quad (122)$$

where

$$S_{3D} = k_0 A_{0,5} + k_{01} A_{1,5} \quad (123a)$$

$$T_{3D} = k_0 A_{0,6} + k_{01} A_{1,6} \quad (123b)$$

$$U_{3D} = k_0(B_{0,5} + B_{0,5}) + k_{01}(B_{1,5} + B_{1,6}) \quad (123c)$$

The total GRF is obtained then by summing all the modal components:

$$GRF_{3D} = F_{3D}^{\mathrm{mod}1} + F_{3D}^{\mathrm{mod}2} + F_{3D}^{ovd} \quad (124)$$

Figure 26a shows the comparison between the GRF obtained through the modal analysis procedure and the GRF obtained numerically. The numerical solution was obtained by solving the first order system of equations of the model

$$\dot{\mathbf{y}}_{3D} = \mathbf{A}_{3D}^{-1}\mathbf{g}_{3D} - \mathbf{A}_{3D}^{-1}\mathbf{B}_{3D}\mathbf{y}_{3D} \tag{125}$$

The solution of Eq. (125) is obtained numerically through 4th order Runge-Kutta method. Figure 26b shows the GRF obtained through the modal analysis procedure and the all the modes components of the GRF.

Figure 26 - a) comparison between numerical (▬▬) and modal analysis' (▪▪▪▪▪) GRF solutions; b) total GRF (▬▬) compared to the first (▬ ▬), second (▬▬▬) and overdamped (▬ · ▬) modes.

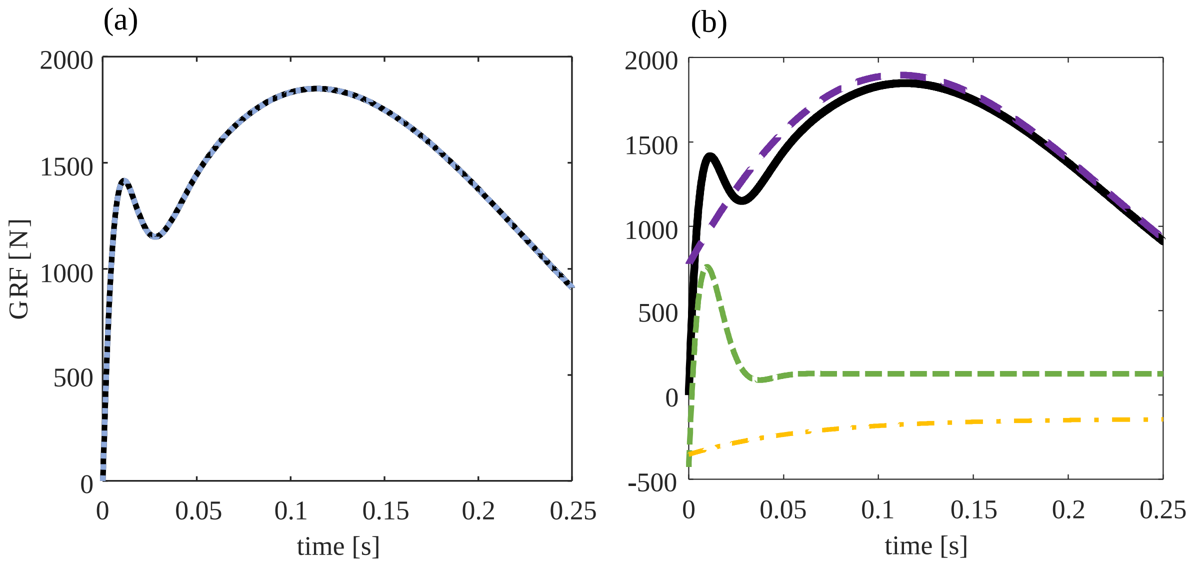

Source: elaborated by the author.

It is possible to see in Fig. 26a that the GRF solution obtained through the modal analysis matches the numerical solution and thus the modal analysis procedure is again validated. The mode components in Fig. 26b show that the first mode has contribution over the whole stance phase and is mainly responsible for the active peak region of the GRF. The shape of the first mode GRF is similar to the upper body impulse forces presented in Clark *et al*. (2014) and Clark *et al*. (2017). The second mode also has influence over the entire stance phase, but mainly at the beginning (0 to 0.05s approximately) being mainly responsible for the impact peak and asymptote roughly 100 N in the latter part. The shape of the second mode GRF is similar to the lower body impulse forces presented in Clark *et al*. (2014) and Clark *et al*. (2017). The overdamped mode starts approximately at -350N and slowly increases to an asymptote at about -150N. The results from Fig. 1b show that there are two main underdamped modes and a less dominant overdamped mode. The results confirm that the GRF can be modelled with three modes only.

4.5. Conclusions

In this chapter, the modal analysis of proposed LPMs (five-DOF and three-DOF) has been performed. The modal analysis was able to show the total GRF of each model and to show the modal components. The modal analysis of both models showed that there are dominant modes. In both cases, there are two underdamped modes that together are responsible for the majority of the dynamics in the GRF and there is an overdamped mode that acts at the beginning of the stance phase. The dominant modes have similar patterns in both models, suggesting the upper and lower body mass impact influence over the modes. The modal analysis of the five-DOF model shows that two of the modes have little influence over the total GRF, suggesting that three modes should be enough to represent the dynamic involved in running GRF.

In the next chapter, a modal model to simulate running GRF will be proposed using the modes information that was observed in the modal analysis of both five-DOF and three-DOF models.

5 MODEL VALIDATION AND ANALYSIS OF EXPERIMENTAL DATA

5.1. Introduction

In the previous chapter, the modal analysis of a five-DOF and a three-DOF model showed that the predominant modes have similar patterns in the GRF simulation (two underdamped modes representing the upper and lower body mass impact) and an overdamped mode acting at the first part of the stance phase. The aim of this chapter is to propose a modal model to simulate running GRF and validate it using different experimental GRF data. In section 5.2 the modal model is presented and explained. In section 5.3, the modal model is used to fit the vertical GRF data from Tongen and Wunderlich (2010). In section 5.4 the modal model is used to fit four different vertical GRF datasets from Wojtusch and von Stryk (2015). In section 5.5, the modal model is used to fit extracted vertical GRF data from Derrick *et al*. (2000).

5.2. Modal Model – Modal Decomposition Method

Despite providing important characteristics of locomotion and bouncing gaits (Bullimore and Burn, 2007), LPMs do not simulate accurately experimental GRF data. These models have problems in predicting the initial part and the two peaks of the GRF at the same time. This may be because these models in general only account for vertical motion, but in practice there is a significant amount of rotation in the movement. Other have found that it is difficult to directly relate the measured acceleration of human body parts to the GRF (Needergard *et al*., 2018), but Komaris *et al*. (2019) found that the body can be connected to the GRF using artificial neural networks. Thus, it is not surprising that LPMs with only vertical motion cannot accurately predict measured GRF datasets from a range of running conditions. Alternatively, more complex LPM could be proposed, but this would implicate in even more parameters to be determined, which may not be viable.

With that in mind, the modal analysis of both three-DOF and five-DOF models showed that the GRF is mainly composed by two main oscillatory motions (one related to the upper body and other related to the lower body) plus one or more non-oscillatory overdamped modes, which means that the GRF can be well represented by three modes. This means that a new GRF modelling method can be implemented using these modes information.

The new modelling method is called modal decomposition of the GRF data. It mainly consists in dividing the GRF dataset in three portions (three modes). Using Eqs. (116) and (118) for the underdamped mode contributions and Eq. (122) for the overdamped mode contribution, the relation GRF relation resultant from the modal decomposition method have the form

$$F_m = \underbrace{G_{m1}e^{a_{m1}t}\sin\left(\omega_{m1}t+\phi_{m1}\right)+E_{m1}}_{\text{first mode (underdamped)}} + \underbrace{G_{m2}e^{a_{m2}t}\sin\left(\omega_{m2}t+\phi_{m2}\right)+E_{m2}}_{\text{second mode (underdamped)}} + \underbrace{G_{m3}e^{a_{m3}t}}_{\text{third mode (overdamped)}} \tag{126}$$

Note that the first and second underdamped modes in Eq. (126) are similar to the cosine periodic force functions presented in Clark *et al*. (2017). However, in this new proposed model the damping is included, and there is a clear relationship with the dynamics of the runner based on the modal response. To obtain the parameters in Eq. (126) that best fit a GRF dataset, the *patternsearch* algorithm is used again due to its fast iteration procedures. In summary, the step-by-step of the modal decomposition method is defined as follows:

1) Fit the first mode equation parameters ($G_{m1}, a_{m1}\ \omega_{m1}, \phi_{m1}, E_{m1}$) for the largest peak region of the experimental GRF using the pattern search optimization routine in Matlab (from the dip between the two peaks until the end of the time history. If a dip does not exist use the complete time history).
2) Subtract the estimated response due to the first mode from the GRF to give a residual.
3) Simultaneously fit mode 2 and mode 3 parameters (G_{m2}, a_{m2}, ω_{m2}, ϕ_{m2}, E_{m2}, G_{m3}, a_{m3}) for the residual of the experimental GRF.
4) Sum the responses for modes 1, 2 and 3 to obtain the estimated total GRF.

In the next sections, the modal decomposition method is applied to six different datasets, available in the literature. Table 14 presents the details about the datasets used to test the model.

Table 14 - Details of the datasets used to test the modal decomposition method.

datasets	subject mass	running velocity	sampling frequerncy	trials	type of GRF
Tongen and Wunderlich	male 77.51 kg	-	2500 Hz	10	Vertical
Wojtusch and von Stryk 1	female 57.3 kg	2 m/s	1000 Hz	1	Vertical
Wojtusch and von Stryk 2	female 57.3 kg	4 m/s	1000 Hz	1	Vertical
Wojtusch and von Stryk 3	male 84.8 kg	2 m/s	1000 Hz	1	Vertical

Wojtusch and von Stryk	4 male 84.8 kg	4 m/s	1000 Hz	1	Vertical
Derrick *et al*.	male 76 kg	-	-	10	Vertical

Source: elaborated by the author.

5.3. Tongen and Wunderlich data fit

The first dataset in which the Modal decomposition method is applied is the open dataset obtained by Tongen and Wunderlich (2010)[2]. The data consists in 10 trials of a male subject (77,51kg) walking, speedwalking and running, obtained with a sample rate of 2500 Hz. The data obtained represents the running GRF in x, y and z directions. Since the focus of the research is in the vertical GRF, only the z force dataset was used in this work (an average of the 10 trials was used). Figure 27a shows the 10 GRF trials with the respective GRF average. The first step of the Modal decomposition method is to fit the active peak (bigger peak) region of the data (for this case, is the region between 0.05s and 0.25s of the time series, approximately). Using the optimization procedure, the first mode equation parameters from Eq. (126) are obtained and the comparison with the total GRF is shown in Fig. 27b. Next, the obtained first mode equation is subtracted from the total GRF dataset. The residual GRF is then is set as the objective function for the second and third mode equations fit (the sum of modes 2 and 3 simultaneously) in Eq. (126) and the optimization algorithm is used again. The residual GRF compared with the sum of second and third mode equations is presented in Fig. 27c. The first, second and third modes obtained through the optimization procedure in the Modal decomposition method is presented if Fig. 27d, compared with the sum of all modes combined (which forms the total model GRF). Table 15 shows the obtained parameters from Eq. (126) relative to all the modes for the Tongen and Wunderlich GRF dataset.

Table 15 - First, second and third mode equation parameters for the Tongen and Wunderlich data fit.

	G_m [N]	a_m [1/s]	$\frac{\omega_m}{2\pi}$ [Hz]	ϕ_m [rad]	E_m [N]
First mode	1195.2	-0.6033	3.59	-0.8784	1070.30
Second mode	999.43	-40.733	17.82	-2.1697	-3.92
Third mode	826.62	-46.256	X	X	X

Source: elaborated by the author.

[2] Available at http://www.math.jmu.edu/_tongen/TongenWunderlich.xls.

Figure 27 below shows each step and the comparison of the Modal decomposition results with the Tongen and Wunderlich GRF dataset.

Figure 27 - Steps and results from the application of the modal decomposition method to the Tongen and Wunderlich GRF dataset. a) GRF trials ( ), GRF trials average ( ) and model GRF ( ); b) first mode ( ) compared to the total experimental GRF ( ); c) second and third modes combined ( ) compared to the subtracted GRF dataset ( ); d) first ( ), second ( ) and third ( ) modes compared with the sum of the modes combined forming the model GRF ( ).

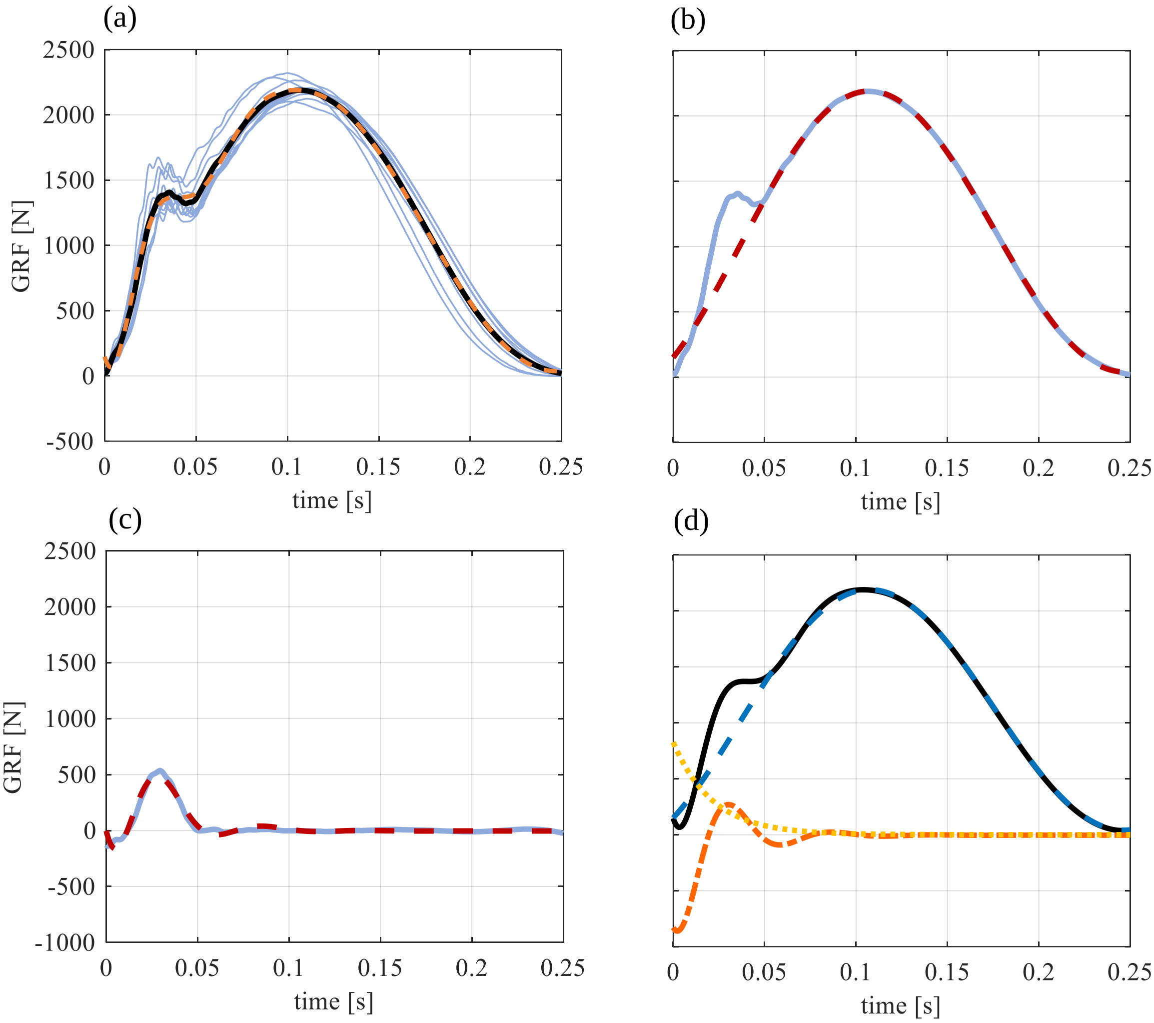

Source: elaborated by the author.

The results obtained with the modal decomposition method shows that the method worked well for this dataset. Figure 1a compared the GRF formed by the sum of all three modes (which is the GRF that results from the application of the method) and the GRF dataset (average). The fit between them is good (RMSE = 1.64%). The modes behaviors are similar to the GRF waveform curves for the discrete masses in the work done by Clark *et al*. (2017), which is expected since the modal decomposition method models the modes to represent the separated effects of the upper and lower body masses. The results also agree overall with the modal analysis of the three-DOF LPM, which was also expected.

5.4. Wojtusch and von Stryk data fit

The next analyzed datasets in which the Modal Composition method is applied is the openly available dataset supplied by Wojtusch and von Stryk (2015)[3]. The data consists in 60 seconds of a female (57.3kg) and a male (84.8kg) human subject running in 2, 3 and 4 m/s. From this dataset, only the middle region of the time frame (35 to 45 seconds) will be analyzed, for 2 and 4 m/s form both subjects. The sample rate (frame rate) is 1000 Hz. The resultant GRF profile for each subject in each velocity is an average of the vertical GRF profile generated by the left and right leg impact on the treadmill between 35 and 45 seconds in the time frame.

The first of the Wojtusch and von Stryk datasets fitted is the one related to the female subject running at 2 m/s. The dataset is presented in Fig. 28a. Following the procedure done for the previous dataset and applying the Modal decomposition method, the first step is to fit the active peak region of the data (for this case, it is the whole data series). The equation obtained after the optimization procedure (same optimization done in the previous dataset) represents the first mode from Eq. (126) and is shown in Fig. 28b compared with the total GRF dataset. The next step is to subtract the first mode equation from the total GRF dataset. Since the GRF dataset has a similar form compared to the first mode, only the residual is small. The second and third mode equations are then fitted to the residual of the GRF dataset, and the comparison is presented in Fig. 28c. The modes are the summed to form the total model GRF. The modes and the total model GRF are shown in Fig. 28d. The comparison between the dataset GRF and the total model GRF is shown in Fig. 28a. Table 16 shows the obtained parameters from Eq. (126) relative to all the modes for the dataset related to the woman running at 2 m/s.

Table 16 - First, second and third mode equation parameters for the Wojtusch and von Stryk dataset related to the woman running at 2 m/s.

	G_m [N]	a_m [1/s]	$\frac{\omega_m}{2\pi}$ [Hz]	ϕ_m [rad]	E_m [N]

[3] Available at https://www.sim.informatik.tu-darmstadt.de/res/ds/humod.

First mode	817.61	-1.9039	2.56	-0.6368	433.10
Second mode	25.98	-1.3680	8.69	3.0971	1.91
Third mode	0	0	X	X	X

Source: elaborated by the author.

Figure 28 below shows each step and the comparison of the Modal decomposition results with the Wojtusch and von Stryk dataset with respect to the woman running at 2 m/s.

Figure 28 - Steps and results from the application of the modal decomposition method to the Wojtusch and von Stryk GRF dataset with respect to the woman running at 2 m/s. a) GRF dataset ( ), model GRF ( ); b) first mode ( ) compared to the total experimental GRF ( ); c) second and third modes combined ( ) compared to the subtracted GRF dataset ( ); d) first ( ), second ( ) and third ( ) modes compared with the sum of the modes combined forming the model GRF ( ).

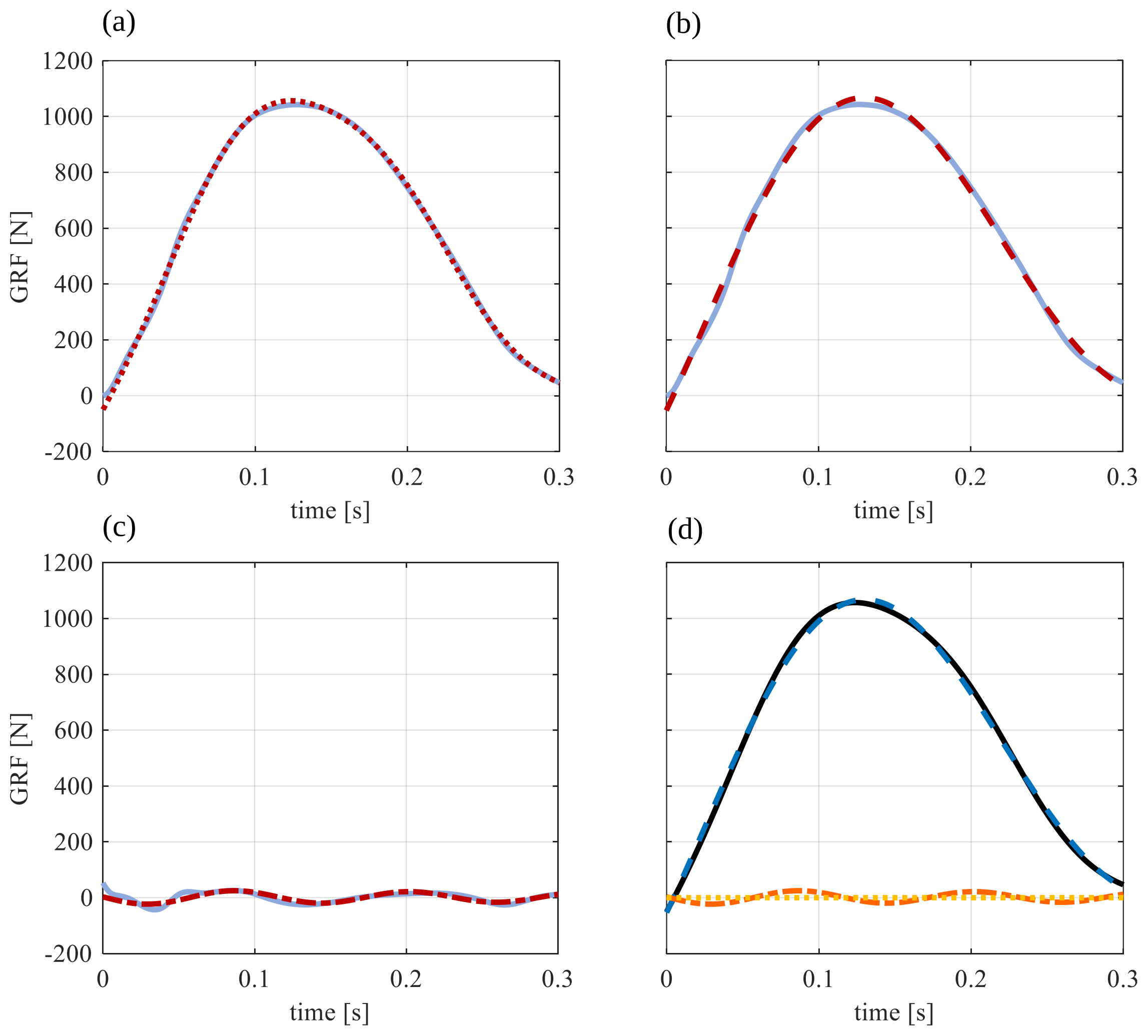

Source: elaborated by the author.

The results obtained with the modal decomposition method shows that the method worked well for this dataset. Figure 28a compared the model GRF formed by the sum of all three modes (which is the GRF that results from the application of the method) and the GRF dataset. The fit between them is good (RMSE = 1.52%). It is interesting to note that the third mode was not necessary in this case. This happens because the dataset has a form similar to the first mode (RMSE = 2.62% when comparing the dataset to the first mode alone), and the second mode was already enough to capture the residual of the dataset after subtracting the first mode. The modes behaviors are similar to the GRF waveform curves for the discrete masses in the work done by Clark *et al*. (2017), which was again expected.

The second dataset fitted in this section is the one related to the female subject running at 4 m/s. The dataset is presented in Fig. 28a. Following the procedure done for the previous dataset and applying the Modal decomposition method, the first step is to fit the active peak region of the data (for this case, it is the whole data series). The equation obtained after the optimization procedure (same optimization done in the previous dataset) represents the first mode from Eq. (126) and is shown in Fig. 28b compared with the total GRF dataset. The next step is to subtract the first mode equation from the total GRF dataset. Since the GRF dataset has a similar form compared to the first mode, only the residual is small. The second and third mode equations are then fitted to the residual of the GRF dataset, and the comparison is presented in Fig. 28c. The modes are the summed to form the total model GRF. The modes and the total model GRF are shown in Fig. 28d. The comparison between the dataset GRF and the total model GRF is shown in Fig. 28a. Table 17 shows the obtained parameters from Eq. (126) relative to all the modes for the dataset related to the woman running at 4 m/s.

Table 17 - First, second and third mode equation parameters for the Wojtusch and von Stryk dataset related to the woman running at 4 m/s.

	G_m [N]	a_m [1/s]	$\frac{\omega_m}{2\pi}$ [Hz]	ϕ_m [rad]	E_m [N]
First mode	716.09	-0.0027	4.29	-0.8547	653.79
Second mode	108.01	-8.9124	11.56	-1.6363	7.14
Third mode	0	0	X	X	X

Source: elaborated by the author.

Figure 29 below shows each step and the comparison of the Modal decomposition results with the Wojtusch and von Stryk dataset with respect to the woman running at 4 m/s.

Figure 29 - Steps and results from the application of the modal decomposition method to the Wojtusch and von Stryk GRF dataset with respect to the woman running at 4 m/s. a) GRF dataset ( ), model GRF ( ); b) first mode ( ) compared to the total experimental GRF ( ); c) second and third modes combined ( ) compared to the subtracted GRF dataset ( ); d) first ( ), second ( ) and third ( ) modes compared with the sum of the modes combined forming the model GRF ( ).

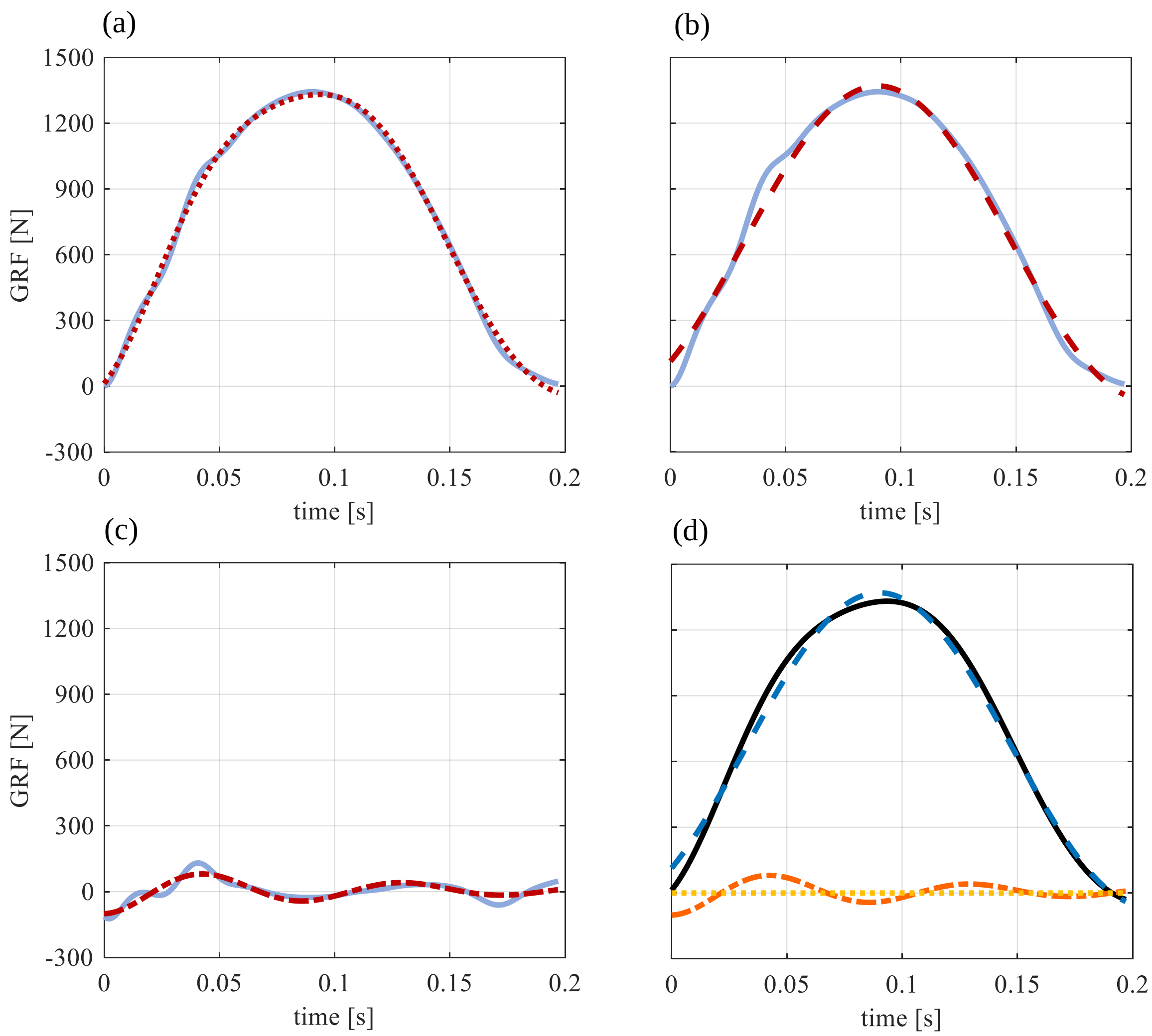

Source: elaborated by the author.

The results obtained with the modal decomposition method shows that the method obtained a good fit for this dataset. Figure 29a compared the model GRF and the GRF dataset. The fit between both is good (RMSE = 2.41%). The third mode was not necessary again in this case. This happens because the dataset has a form similar to the first mode (RMSE = 5.14% when comparing the dataset to the first mode alone), and the second mode was already enough to capture the residual of the dataset after subtracting the first mode. The modes behaviors are similar to the GRF waveform curves for the discrete masses in the work done by Clark *et al.* (2017), which was again expected.

The third dataset fitted in this section is the one related to the male subject running at 2 m/s. The dataset is presented in Fig. 29a. Following the procedure done for the previous dataset and applying the Modal decomposition method, the first step is to fit the active peak region of the data (for this case, between 0.05s to 0.37 approximately). The equation obtained after the optimization procedure represents the first mode from Eq. (126) and is shown in Fig.4b compared with the total GRF dataset. The next step is to subtract the first mode equation from the total GRF dataset. The second and third mode equations are then fitted to the residual of the GRF dataset, and the comparison is presented in Fig. 29c. The modes are the summed to form the total model GRF. The modes and the total model GRF are shown in Fig. 29d. The comparison between the dataset GRF and the total model GRF is shown in Fig. 29a. Table 18 shows the obtained parameters from Eq. (126) relative to all the modes for the dataset related to the man running at 2 m/s.

Table 18 - First, second and third mode equation parameters for the Wojtusch and von Stryk dataset related to the man running at 2 m/s.

	G_m [N]	a_m [1/s]	$\frac{\omega_m}{2\pi}$ [Hz]	ϕ_m [rad]	E_m [N]
First mode	1340.7	-2.1556	1.90	-0.4346	500.52
Second mode	1235.2	-49.795	9.50	-0.0556	2.42
Third mode	0	0	X	X	X

Source: elaborated by the author.

Figure 30 next shows each step and the comparison of the Modal decomposition results with the Wojtusch and von Stryk dataset with respect to the man running at 2 m/s.

Figure 30 - Steps and results from the application of the modal decomposition method to the Wojtusch and von Stryk GRF dataset with respect to the man running at 2 m/s. a) GRF dataset (▬▬), model GRF (▪▪▪▪); b) first mode (▬ ▪) compared to the total experimental GRF (▬▬); c) second and third modes combined (▬ ▪) compared to the subtracted GRF dataset (▬▬); d) first (▬ ▪), second (▬ ▬) and third (▪▪▪▪) modes compared with the sum of the modes combined forming the model GRF (▬▬).

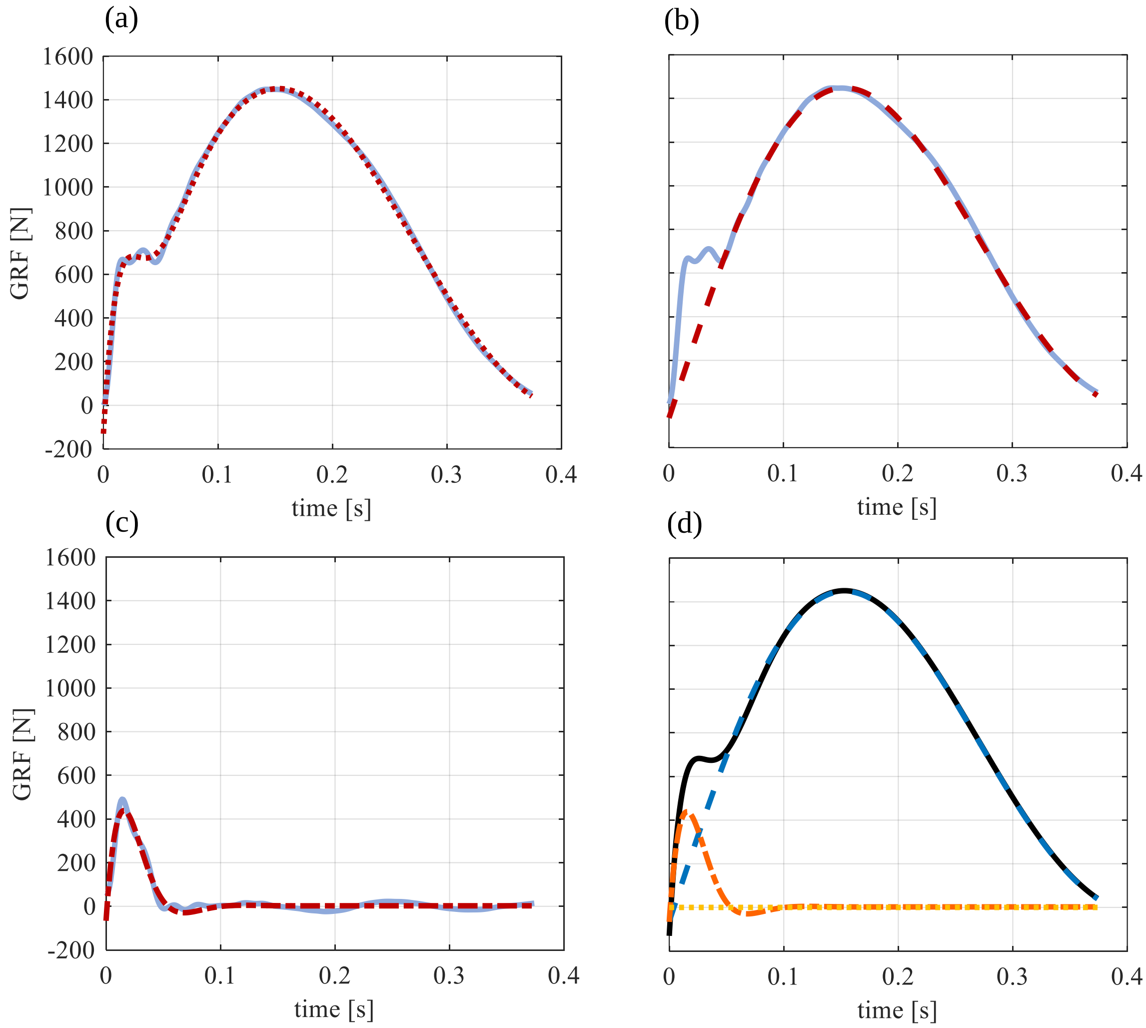

Source: elaborated by the author.

The results obtained with the modal decomposition method shows that the method obtained a good fit for this dataset. Figure 30a compared the model GRF and the GRF dataset. The fit between both is good (RMSE = 2.03%). The third mode was not necessary again in this case. This happens in this case because after subtracting the first mode from the dataset, the residual is similar to a decaying exponential, which can be well modelled by the equation of the second mode (see Eq. (126)). The modes behaviors are similar to the GRF waveform curves for the discrete masses in the work done by Clark *et al*. (2014), which was again expected due to the form of the mode equations.

The fourth dataset fitted in this section is the one related to the male subject running at 4 m/s. The dataset is presented in Fig. 30a. Following the procedure done for the previous dataset and applying the Modal decomposition method, the first step is to fit the active peak region of the data (for this case, between 0.03s to 0.25 approximately). The equation obtained after the optimization procedure represents the first mode from Eq. (126) and is shown in Fig. 30b compared with the total GRF dataset. The next step is to subtract the first mode equation from the total GRF dataset. The second and third mode equations are then fitted to the residual of the GRF dataset, and the comparison is presented in Fig. 30c. The modes are the summed to form the total model GRF. The modes and the total model GRF are shown in Fig. 30d. The comparison between the dataset GRF and the total model GRF is shown in Fig. 30a. Table 19 shows the obtained parameters from Eq. (126) relative to all the modes for the dataset related to the man running at 4 m/s.

Table 19 - First, second and third mode equation parameters for the Wojtusch and von Stryk dataset related to the man running at 4 m/s.

	G_m [N]	a_m [1/s]	$\frac{\omega_m}{2\pi}$ [Hz]	ϕ_m [rad]	E_m [N]
First mode	2575.90	-2.9200	2.12	-0.1431	-138.72
Second mode	3123.20	-72.503	11.00	0.0898	3.86
Third mode	0	0	X	X	X

Source: elaborated by the author.

Figure 31 next shows each step and the comparison of the Modal decomposition results with the Wojtusch and von Stryk dataset with respect to the man running at 4 m/s.

Figure 31 - Steps and results from the application of the modal decomposition method to the Wojtusch and von Stryk GRF dataset with respect to the man running at 4 m/s. a) GRF dataset ( ), model GRF ( ); b) first mode ( ) compared to the total experimental GRF ( ); c) second and third modes combined ( ) compared to the subtracted GRF dataset ( ); d) first ( ), second ( ) and third ( ) modes compared with the sum of the modes combined forming the model GRF ( ).

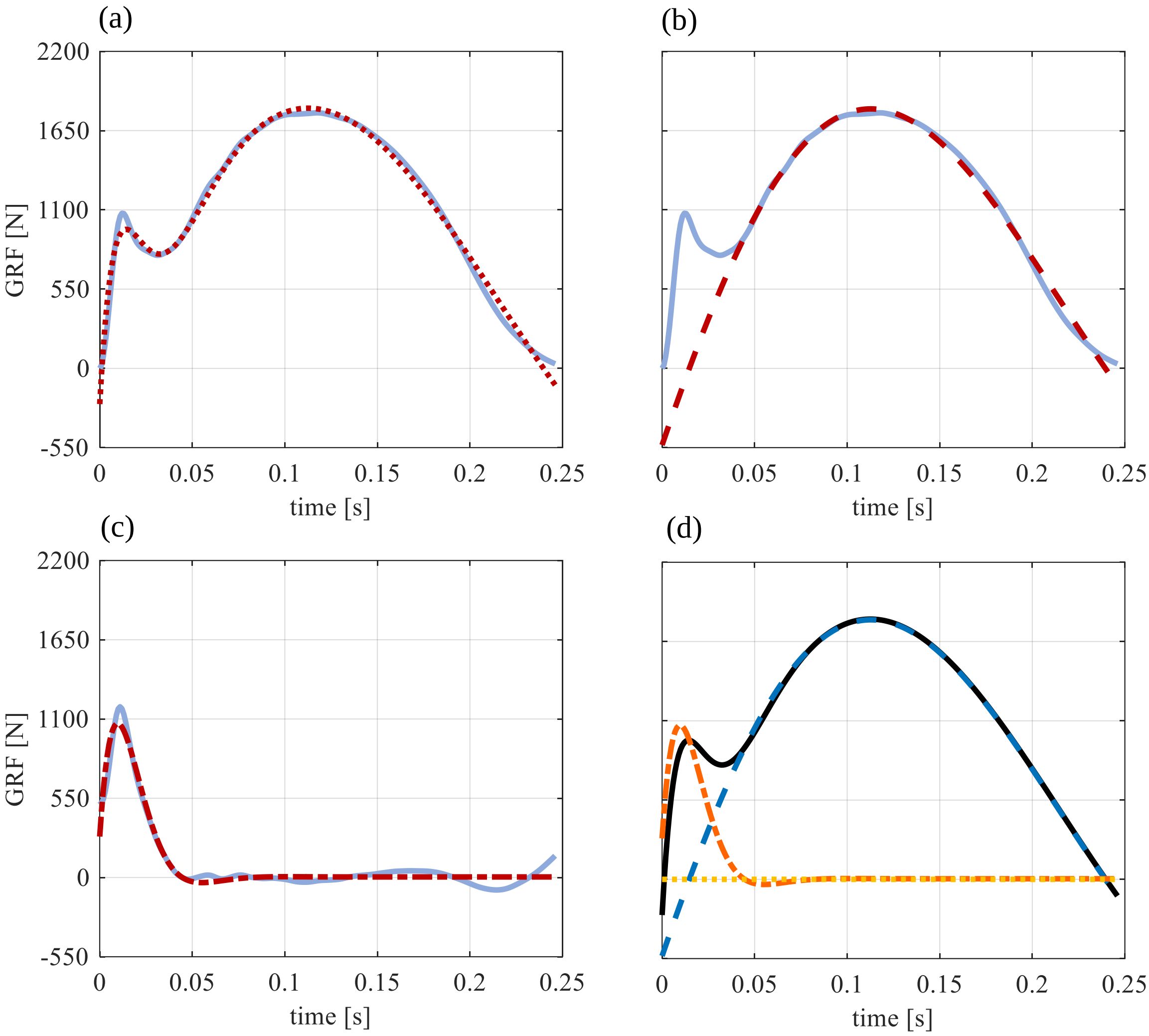

Source: elaborated by the author.

The results obtained with the modal decomposition method shows that the method obtained a good fit for this dataset. Figure 5a compared the model GRF and the GRF dataset. The fit between both is good (RMSE = 3.99%). The third mode was not necessary again in this case. This happens in again because after subtracting the first mode from the dataset, the residual is similar to a decaying exponential, which can be well modelled by the equation of the second mode (see Eq. (126)). The modes behaviors are similar to the GRF waveform curves for the discrete masses in the work done by Clark *et al*. (2017), which was again expected due to the form of the mode equations.

5.5. Derrick *et al*. data fit

The dataset used in this section was extracted from the work done in Derrick *et al*. (2000) for one single subject running in its preferred stride length. The dataset is used as last validation test for the Modal decomposition method, due to its features (high first peak or impact peak). The dataset is presented in Fig. 32a. Applying again the modal decomposition method, the first step is to fit the active peak region of the data (for this case, between 0.04s to 0.20 approximately). The equation obtained after the optimization procedure represents the first mode from Eq. (126) and is shown in Fig. 32b compared with the total GRF dataset. The next step is to subtract the first mode equation from the total GRF dataset. The second and third mode equations are then fitted to the residual of the GRF dataset, and the comparison is presented in Fig. 32c. The modes are the summed to form the total model GRF. The modes and the total model GRF are shown in Fig. 32d. The comparison between the dataset GRF and the total model GRF is shown in Fig. 32a. Table 20 shows the obtained parameters from Eq. (126) relative to all the modes for the Derrick *et al*. dataset.

Table 20 - First, second and third mode equation parameters for the Derrick *et al*. dataset.

	G_m [N]	a_m [1/s]	$\frac{\omega_m}{2\pi}$ [Hz]	ϕ_m [rad]	E_m [N]
First mode	12042	-7.701	1.14	0.1265	-2361.30
Second mode	1568.60	-49.551	23.10	-1.6626	-5.57
Third mode	2473.20	-43.292	X	X	X

Source: elaborated by the author.

Figure 32 next shows each step and the comparison of the Modal decomposition results with the Derrick *et al*. dataset.

Figure 32 - Steps and results from the application of the modal decomposition method to the Derrick *et al*. Dataset. a) GRF dataset ( ), model GRF ( ); b) first mode ( ) compared to the total experimental GRF ( ); c) second and third modes combined ( ) compared to the subtracted GRF dataset ( ); d) first ( ), second ( ) and third ( ) modes compared with the sum of the modes combined forming the model GRF ( ).

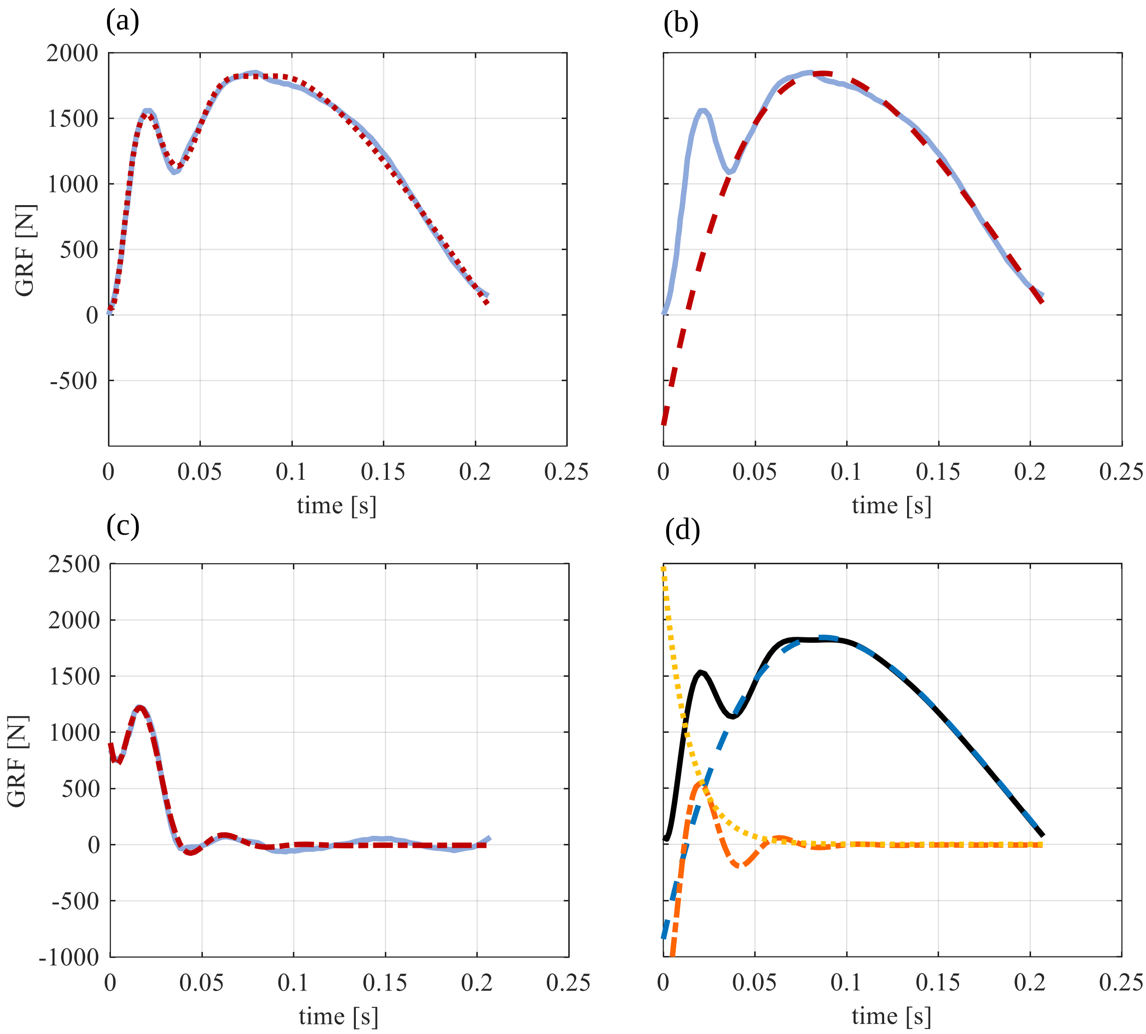

Source: elaborated by the author.

The Derrick *et al*. GRF dataset has a fast and considerably big impact peak (first peak) and decays fast after the first peak, including a small loading rate, which makes the GRF more difficult to fit. For this case, the third mode had a considerably effect over the total GRF, as we can see in Fig. 32d. The first mode is responsible for the active peak while the second and third modes acts more over the first peak. The fit between the mode GRF and the dataset was good (RMSE = 2.63%), which is a good result for the model since this GRF has difficult features to be modelled. In this case, the modes physical meaning is more difficult to be analyzed due to the bigger influence of the third mode (supposed to be smaller).

5.6. Conclusions

In this chapter, a modal model has proposed and validated to simulate running GRFs. The model consists in building the total GRF by adding three mode components, two of which are underdamped, and one is overdamped. The modal model has been validated through six different vertical GRF data with different characteristics. Overall, the RMSE error for all GRF model fits were small, which validates the model. It was observed the third mode was necessary only in datasets where the loading rate were smaller. The modal parameters varied a lot for each fit, and it is difficult with data sets used to interpret them physically.

6 CONCLUSIONS

6.1. Summary of the Thesis

The aim of this chapter is to present the main conclusions of the thesis and recommendations for future work. The work reported in each chapter is first summarized.

Chapter 1 described the historical background related to mathematical models, differential equations, and ground reaction force (GRF) analysis. Then, the literature review highlights some of the important works regarding experimental GRF measurement and GRF modelling. Lastly, the objectives, the contributions and the outline of the thesis are recorded.

Chapter 2 gives a more detailed report of five important studies regarding GRF modelling. First, the work done by Blickhan (1989) is described, in which a one-DOF LPM is proposed to simulate vertical GRF for hopping in place and a two-DOF LPM is proposed to simulate the GRF for running and hopping forward. Next, the two-DOF LPM used by Alexander (1990) to simulate running vertical GRF for animals or robots with a padded foot is presented, with some analysis regarding energy and momentum equilibrium. Later, the classic work from Nigg and Liu (1999) is discussed, in which a four-DOF nonlinear LPM is proposed to simulate running vertical GRF for soft and hard sole conditions. The model introduces the wobbling mass effect to GRF modelling. Next, the two-mass model proposed by Clark *et al*. (2014) is presented, which uses impulse sinusoidal curves to build the total vertical GRF from the impulses of the lower and upper body masses. Finally, the two-DOF LPM from Verheul *et al*. (2019) using natural parameters to simulate the vertical GRF in different tasks (only running was considered in the thesis).

Chapter 3 describes a new linear ground contact model for vertical GRF simulation through LPMs. First, the Zener model is explained, which is used to simulate the behavior of viscoelastic materials. An adaptation of the Zener model is then proposed to model the ground contact for lumped parameter GRF models. The adaptation simplifies the dynamics of the ground contact interface using a small mass in between the spring and damper connected in series. The AZM is then tested, replacing the nonlinear ground contact relation in the four-DOF model from Nigg and Liu (1999) and comparing the GRF simulation with the original four-DOF model for soft and hard sole conditions.

Chapter 4 presents the modal analysis of two different lumped parameter GRF models with the AZM. First, a general modal analysis methodology is described, using state-space representation. This method was chosen to accurately represent the eigenvalues (natural frequencies) and eigenvectors (modes) of the models in question, which have non-proportional damping. The modal analysis procedure is then applied to the NLM with the AZM (five-DOF linear model) for soft sole condition, showing that from the five modes, two underdamped and one overdamped are dominant (two underdamped modes are more dominant that the overdamped mode). This suggests three modes may be enough to represent running GRF. A three-DOF LPM using the AZM is then optimized to match the five-DOF model. Finally, the modal analysis procedure is applied to the three-DOF lumped mass GRF model.

Chapter 5 presents a new modal model to simulate running vertical GRF. The modal model (Modal Decomposition) is described at the beginning of the chapter. The approach consists of dividing the total vertical GRF into three mode components, two being underdamped (upper and lower body mass influences) and one overdamped. The approach is then validated using different vertical GRF data from the literature. For each data set, an optimization procedure was performed to find the model's best parameters to fit the different GRF datasets. The model was able to simulate the vertical GRF datasets with good accuracy (maximum of 3,99% RMSE was found).

6.2. Main conclusions

From the analysis of the proposed AZM as a ground contact model replacement for the nonlinear ground contact model in Nigg and Liu (1999), it can be concluded that:

- The AZM with optimized parameters was able to simulate the running GRF from the original model for both soft and hard sole conditions, which validates the model.

- The AZM is linear, which makes the parameter optimization more viable. As to the physical significance of the parameters, linear parameters have been investigated in the literature (Alexander *et al.*, 1986; Blickhan, 1989; Verheul *et al.*, 2019) and may be easier to correlate through experimental investigation.

From the modal analysis of the five-DOF and three-DOF LPMs, it can be concluded that:

- The modal analysis procedure adopted was able to successfully represent the modal components of the total GRF in both models.

- The overdamped modal components have little effect overall on the total GRF. Their influence is greater in the first part of the stance phase and mainly an offset on the later part (in both models).

- The GRF curves can be well modelled using two underdamped components (one slower and larger, related to the upper body mass; another faster and smaller, related to the lower body mass) and one overdamped component, which acts mostly in the beginning of the stance phase.

- The modal behavior of the model led to the proposition of a new GRF model, which consists of forming the total GRF using three main modal components.

From the application of the Modal Decomposition model to fit the literature GRF datasets, it can be concluded that:

- Overall, all the different vertical GRF data were fitted using the Modal Decomposition model, with a maximum RMSE of 3.99%.

- For most of the datasets, the two underdamped modes were sufficient to obtain a good fit. It was observed that profiles with faster loading rates and smoother transitions from impact peak to active peak do not require the overdamped mode.

- It may be difficult to correlate the modes physically with human body running since the parameters from the modal model vary significantly.

6.3. Recommendations for future work

In this work, vertical GRF data from the literature was used to validate a proposed modal GRF model. Further work might include:

- To experimentally obtain our own GRF datasets, in order to control parameters like running speed, foot sole conditions, body mass, etc.

- To investigate the Modal Decomposition model fit with more experimental GRF datasets, to correlate physically the model parameters to human body properties.

- Investigate when the third mode is needed in the Modal Decomposition model to simulate running GRF (also using more experimental GRF datasets).

REFERENCES

AERTS, P., DE CLERCQ, D. Deformation characteristics of the heel region of the shod foot during a simulated heel strike: The effect of varying midsole hardness. **Journal of Sports Sciences**, London, v. 11, n. 5, p. 449-461, 1993.

ALEXANDER, R. McN. Three Uses for Springs in Legged Locomotion. **The International Journal of Robotics Research**, London, v. 9, n. 2, p. 53-61, 1990.

ALEXANDER, R. McN. BENNETT, M. B. KER, R. F. Mechanical properties and function of the paw pads of some mammals. **Journal of Zoology**, London, v. 209, n. 3, p. 405-419, 1986.

AMAR, J. Trottoir dynamographique. **Comptes rendus hebdomadaires des séances de l'Académie des Sciences**, Paris, v. 163, n. 1, p. 130-133, 1916.

ANDRIACCHI, T. P. OGLE, J. A. GALANTE, J. O. Walking speed as a basis for normal and abnormal gait measurements. **Journal of Biomechanics,** New York, v. 10, n. 4, p. 261-268, 1977.

ARCAN, M. BRULL, M. A. A fundamental characteristic of the human body and foot, the foot-ground pressure pattern. **Journal of Biomechanics,** New York, v. 9, n. 7, p. 453-457, 1976.

ARCHIBALD, T. FRASER, G. GRATTAN-GUINNESS, I. The History of Differential Equations, 1670-1950. **Oberwolfach Reports**, Oberwolfach, v. 1, n. 4, p. 2729-2794, 2005.

BARELA, A. M. DE FREITAS, P. B. CELESTINO, M. L. CAMARGO, M. R. BARELA, J. A. Ground reaction forces during level ground walking with body weight unloading. **Brazilian Journal of Physical Therapy**, São Carlos, v. 18, n. 6, p. 572-579, 2014.

BATES, N. A. FORD, K. R. MYER, G. D. HEWETT, T. E. Impact differences in ground reaction force and center of mass between the first and second landing phases of a drop vertical jump and their implications for injury risk assessment. **Journal of Biomechanics**, New York, v. 46, n. 7, p. 1237-1241, 2013.

BAUMAN, J. H. BRAND, P. W. Measurement of pressure between foot and shoe. **The Lancet**, London, v. 281, n. 7282, p. 629-632, 1963.

BEELY, F. Zur Mechanik des Stehens. Uber die Beddeutung des Fussgewolbes beim Stehen. **Langenbecks Archive fur klinische chirurgie**, Berlin, v. 27, n. 1, p. 457-471, 1882.

BILLING, D. C. NAGARAJAH, C. R. HAYES, J. P. BAKER, J. Predicting ground reaction forces in running using micro-sensors and neural networks. **Sports Engineering**, New York, v. 9, n. 1, p. 15-27, 2006.

BLICKHAN, R. The spring-mass model for running and hopping. **Journal of Biomechanics**, New York, v. 22, n. 11-12, p. 1217-1227, 1989.

BRENNAN, M. J. CARRELLA, A. WATERS, T. P. JUNIOR, V. L. On the dynamic behavior of a mass supported by a parallel combination of a spring and an elastically connected damper. **Journal of Sound and Vibration**, London, n. 3-5, v. 309, p. 823-837, 2008.

BRYANT, J. D. BENNETT, M. B. BRUST, J. ALEXANDER, R. McN. Forces exerted on the ground by galloping dogs (*canis familiaris*). **Journal of Zoology**, London, v. 213, n. 2, p. 193-203, 1987.

BULLIMORE, S. BURN, J. G. Ability of the planar spring-mass model to predict mechanical parameters in running humans. **Journal of Theoretical Biology**, London, v. 248, n. 4, p. 686-695, 2007.

CARLET, G. **Essai experimental sur la locomotion humaine: étude de la marche**. Paris: Université de Paris, 1872.

CASTRO, M. P. FIGUEIREDO, M. C. ABREU, S. SOUSA, H. MACHADO, L. SANTOS, R. VILAS-BOAS, J. P. The influence of gait cadence on the ground reaction forces and plantar pressures during load carriage of young adults. **Applied Ergonomics**, Guildford, v. 49, n. 1, p. 41-46, 2015.

CAVAGNA, G. A. SAIBENE, F. P. MARGARIA, R. Mechanical work in running. **Journal of Applied Physiology**, Washington, v. 19, n. 2, p. 249-256, 1964.

CAVANAGH, P. R. LAFORTUNE, M. A. Ground reaction forces in distance running. **Journal of Biomechanics**, New York, v. 13, n. 5, p. 397-406, 1980.

CLARK, K. P. RYAN, L. J. WEYAND, P. G. Foot speed, foot-strike and footwear: linking gait mechanics and running ground reaction forces. **Journal of Experimental Biology**, Cambridge, v. 217, n. 12, p. 2037-2040, 2014.

CLARK, K. P. RYNA, L. J. WEYAND, P. G. A general relationship links gait mechanics and running ground reaction forces. **Journal of Experimental Biology**, Cambridge, v. 220, n. 2, p. 247-258, 2017.

COLE, G. K. **Loading of the joints of the lower extremities during the impact phase in running**. Calgary, University of Calgary, 1995.

CRISAN, D. DOUCET, A. A Survey of Convergence Results on Particle Filtering Methods for Practitioners. **IEEE Transactions on signal processing**, v. 50, n. 3, p. 736-746, 2002.

CSÀJI, B. C. **Approximation with Artificial Neural Networks**. Budapest, Eötvös Loránd University, 2001.

CUNNINGHAM, D. M. Components of floor reaction during walking. **Devices Research Project I.E.R. report**, Berkeley, University of California, Series 11, n. 14, 1950.

DE WIT, B. DE CLERCQ, D. AERTS, P. Biomechanical analysis of the stance phase during barefoot and shod running. **Journal of Biomechanics**, New York, v. 33, n. 3, p. 269-278, 1999.

DERRICK, T. R. CALDWELL, G. E. HAMILL, J. Modeling the Stiffness Characteristics of the Human Body While Running With Various Stride Lengths. **Journal of Applied Biomechanics**, Champaign, v. 16, n. 1, p. 36-51, 2000.

DICKINSON, J. A. COOK, S. D. LEINHARDT, T. M. The measurements of shock waves following heel strike while running. **Journal of Biomechanics**, New York, v. 18, n. 6, p. 415-422, 1985.

DUTTO, D. J. SMITH, G. A. Changes in spring-mass characteristics during treadmill running to exhaustion. **Medicine & Science in Sports & Exercise**, Hagerstown, v. 34, n. 8, p. 1324-1331, 2002.

ELFTMAN, H. A cinematic study of the distribution of pressure in the human foot. **The Anatomical Record**, Philadelphia, v. 59, n. 4, p. 481-491, 1934.

FARLEY, C. T. GONZALEZ, O. Leg stiffness and stride frequency in human running. **Journal of Biomechanics**, New York, v. 29, n. 2, p. 181-186, 1996.

[a]FENN, W. O. Frictional and kinetic factors in the work of sprint running. **American Journal of Physiology**, Baltimore, v. 92, n. 3, p. 583-611, 1930.

[b]FENN, W. O. Work against gravity and work due to velocity changes in running: Movements of the center of gravity within the body and foot pressure on the ground. **American Journal of Physiology**, Baltimore, v. 93, n. 2, p. 433-462, 1930.

FISCHER, O. Kinematik organischer Gelenke. **Vieweg & Sohn**, Braunschweig, v. 165, n. 76, p. 489-490, 1907.

FLUIT, R. ANDERSEN, M. S. KOLK, S. VERDONSCHOT, N. KOOPMAN, H. F. J. M. Prediction of ground reaction forces and moments during various activities of daily living. **Journal of Biomechanics**, New York, v. 47, n. 10, p. 2321-2329, 2015.

GINSBERG, J. H. **Mechanical and structural vibrations: theory and applications**. New York: Wiley, 2001.

GREENE, P. R. MCMAHON, T. A. Reflex stiffness of man's anti-gravity muscles during kneebends while carrying extra weights. **Journal of Biomechanics**, New York, v. 12, n. 12, p. 881-891, 1979.

GRUBER, K. RUDERM H, DENOTH, J. SCHNEIDER, K. A comparative study of impact dynamics: wobbling mass model versus rigid body models. **Journal of Biomechanics**, New York, v. 31, n. 5, p. 439-444, 1998.

GURCHIEK, R. D. McGINNIS, R. S. NEEDLE, A. R. McBRIDE, J. M. VAN WERKHOVEN, H. The use of a single inertial sensor to estimate 3-dimensional ground reaction force during accelerative running tasks. **Journal of Biomechanics**, New York, v. 61, n. 16, p. 263-268, 2017.

HAMILL, J. GRUBER, A. H. DERRICK, T. R. Lower extremity joint stiffness characteristics during running with different footfall patterns. **European Journal of Sport Science**, Abingdon, v. 14, n. 2, p. 130-136, 2014.

JAPIASSÚ, H. MARCONDES, D. **Dicionário Básico de Filosofia**. Jorge Zahar Editor, Brazil, 2001.

KALLRATH, Josef (Ed.). **Modeling languages in mathematical optimization**. Dordrecht: Kluwer Academic Publishers, 2004.

KHAJAH, T, HOU, G. Parameter identification for vertical ground reaction forces on feet while running. **Sports Engineering**, New York, v. 18, n. 4, p. 217-226, 2015.

KLUTE, G. K., BERGE, J. S. Modelling the effect of prosthetic feet and shoes on the heel-ground contact force in amputee gait. **Proceedings of the Institution of Mechanical Engineers, Part H: Journal of Engineering in Medicine**, London, v. 218, n. 3, p. 173-182, 2004.

LEPORACE, G. BATISTA, L. A. NADAL, J. Prediction of 3D ground reaction forces during gait based on accelerometer data. **Research on Biomedical Engineering**, Rio de Janeiro, v. 34, n. 3, p. 211-216, 2018.

LIEBERMAN, D. E. VENKADESAN M. WERBEL, W. A. DAOUD, A. I. D'ANDREA, S. DAVIS, I. S. MANG'ENI, R. O. PITSILADIS, Y. Foot strike patterns and collision forces in habitually barefoot versus shod runners. **Nature**, London, v. 463, n. 7280, p. 531-535, 2010.

LIU, W. NIGG, B. M. A mechanical model to determine the influence of masses and mass distribution on the impact force during running. **Journal of Biomechanics**, New York, v. 33, n. 2, p. 219-224, 2000.

LY, Q. H. ALAOUI, A. ERLICHER, S. BALY, L. Towards a footwear design tool: Influence of shoe midsole properties and ground stiffness on the impact force during running. **Journal of Biomechanics**, New York, v. 43, n. 2, p. 310-317, 2010.

MANLEY, M. T.; SOLOMON, E. The clinical assessment of the normal and abnormal foot during locomotion. **Prosthetics and Orthotics International**, London, v. 3, n. 2, p. 103-110, 1979.

MANN, R. HERMAN, J. Kinematic analysis of Olympic sprint performance: men's 200 meters. **Journal of Applied Biomechanics**, New York, v. 1, n. 2, p. 151-162, 1985.

MCMAHON, T. A. CHENG, G. C. The mechanics of running: how does stiffness couple with speed? **Journal of Biomechanics**, New York, v. 23, n. 1, p. 65-78, 1990.

MCMAHON, T. A. VALIANT, G. FREDERICK, E. C. Groucho running. **Journal of Applied Physiology**, Washington, v. 62, n. 6, p. 2326-2337, 1987.

MEURISSE, G. M. DIERICK, F. SCHEPENS, B. BASTIEN, G. J. Determination of the vertical ground reaction forces acting upon individual limbs during healthy and clinical gait. **Gait & Posture**, Oxford, v. 43, n. 1, p. 245-250, 2016.

MIZRAHI, J. SUSAK, Z. In-vivo elastic and damping response of the human leg to impact forces. **Journal of Biomechanical Engineering**, New York, v. 104, n. 1, p. 63-66, 1982.

MOMBURG, F. **Der Gang des Menschen und die Fussgeschwulst**. Germany: Hirschwald, 1908.

NARAYAN, S. **A Textbook of Matrices**. New Delhi: S. Chand, 1953.

NEDERGAARD, N. J. VERHEUL, J. DRUST, B. ETCHELLS, T. LISBOA, P. ROBINSON, M. A. VANRENTERGHEM, J. The feasibility of predicting ground reaction forces during running from a trunk accelerometry driven mass-spring-damper model. **PeerJ**, Corte Madera, 6:e6105. DOI: 10.7717/peerj.6105.

NIGG, B. M. **Biomechanics of running shoes**. Champaign: Human Kinetics, 1986.

NIGG, B. M. LIU, W. The effect of muscle stiffness and damping on simulated impact force peaks during running. **Journal of Biomechanics**, New York, v. 32, n. 8, p. 849-856, 1999.

NIGG, B. M. BAHLSEN H. A. LUETHI, S. M. STOKES, S. The influence of running velocity and midsole hardness on external impact forces in heel-toe running. **Journal of Biomechanics**, New York, v. 20, n. 10, p. 951-959, 1987.

NIKOOYAN, A. A. ZADPOOR, A. A. A model-based parametric study of soft tissue vibrations during running. *In*: IEEE Benelux EMBS Symposium, 2007, Netherlands. **Proceedings** […] Eidhoven: IEEE-EMBS Benelux Chapter, 2007. p. 49-52.

NIKOOYAN, A. A. ZADPOOR, A. A. Mass–spring–damper modelling of the human body to study running and hopping–an overview. **Proceedings of the institution of mechanical engineers, Journal of engineering in medicine**, London, v. 225, n. 12, p. 1121-1135, 2011.

SATO, K. POCZWARDOWSKI, A. MOKHA, M. B. Relationship between ground reaction force and stability level of the lower extremity in young active adults. In: **ISBS-Conference Proceedings Archive**. China, 2005.

SHAHABPOOR, E. PAVIC, A. Estimation of vertical walking ground reaction force in real-life environments using single IMU sensor. **Journal of Biomechanics**, London, v. 79, n. 5, p. 181-190, 2018.

SINCLAIR, J. ATKINS, S. TAYLOR, P. J. The effects of barefoot and shod running on limb and joint stiffness characteristics in recreational runners. **Journal of Motor Behavior**, Washington, v. 48, n. 1, p. 79-85, 2016.

STERZING, T. SCHWEIGER, V. DING, R. CHEUNG, J. T. BRAUNER, T. Influence of rearfoot and forefoot midsole hardness on biomechanical and perception variables during heel-toe running. **Footwear Science**, Abingdon, v. 5, n. 2, p. 71-79, 2013.

STILES, V. H. DIXON, S. J. The influence of different playing surfaces on the biomechanics of a tennis running forehand foot plant. **Journal of Applied Biomechanics**, New York, v. 22, n. 1, p. 14-24, 2006.

SUTHERLAND, D. H. The evolution of clinical gait analysis part III–kinetics and energy assessment. **Gait & Posture**, Oxford, v. 21, n. 4, p. 447-461, 2005.

TONGEN, A. WUNDERLICH, R. E. Biomechanics of running and walking. In J. Gallian (Ed.), **Mathematics and Sports**, Cambridge, p. 315-328, 2010.

TSE, F. MORSE. I. E. HINKLE, R. T. **Mechanical Vibrations Theory and Applications.** New Delhi: CBS Publishers & Distributors, 1964.

UDOFA, A. B. RYAN, L. J. WEYAND, P. G. Impact forces during running: loaded questions, sensible outcomes. In: INTERNATIONAL CONFERENCE ON WEARABLE AND IMPLANTABLE BODY SENSOR NETWORKS (BSN 2016 IEEE), 13., 2016, San Francisco. **Proceedings** […] San Francisco: IEEE, 2016. p. 371-376.

VAN DER WORP, H. VRIELINK, J. W. BREDEWEG, S. W. Do runners who suffer injuries have higher vertical ground reaction forces than those who remain injury-free? A systematic review and meta-analysis. **British journal of sports medicine**, Loughborough, v. 50, n. 8, p. 450-457, 2016.

VERHEUL, J. NEDERGAARD, N. J. POGSON, M. LISBOA, P. GREGSON, W. VANRENTERGHEM, J. ROBINSON, M. A. Biomechanical loading during running: can a two mass-spring-damper model be used to evaluate ground reaction forces for high-intensity tasks?. **Sports biomechanics**, Abingdon, v. 1, n. 1, p. 1-12, 2019.

WEISBERG, S. **Applied linear regression**. Hoboken: John Wiley & Sons, 2005.

WEYAND, P. G. SMITH, B, R. SCHULTZM N. S. LUDLOW, L. W. Predicting metabolic rate across walking speed: one fit for all body sizes? **Journal of Applied Physiology**, Washington, v. 115, n. 9, p. 1332-1342, 2013.

WEYAND, P. G. BUNDLE, M. W. McGOWAN, C. P. GRABOWSKI, A. BROWN, M. B. KRAM, R. HERR, H. The fastest runner on artificial legs: different limbs, similar function?. **Journal of Applied Physiology**, Washington, v. 107, n. 3, p. 903-911, 2009.

WEYAND, P. G. SANDELL, R. F. PRIME, D. N. L. BUNDLE, M. W. The biological limits to running speed are imposed from the ground up. **Journal of Applied Physiology**, Washington, v. 108, n. 4, p. 950-961, 2010.

WOJTUSCH, J. VON STRYK, O. Humod - a versatile and open database for the investigation, modeling and simulation of human motion dynamics on actuation level. *In*: INTERNATIONAL CONFERENCE ON HUMANOID ROBOTS (HUMANOIDS), 15., 2015, Seoul. Proceedings […] Seoul: IEEE, 2015. p. 74-79.

YAMASHITA, T. KATOH, R. Moving pattern of point of application of vertical resultant force during level walking. **Journal of Biomechanics**, New York, v. 9, n. 2, p. 93-99, 1976.

YUE, Z. MESTER, J. A Modal Analysis of Resonance during the Whole-Body Vibration. **Studies in Applied Mathematics**, Oxford, v. 112, n. 3, p. 293-314, 2004.

YUKAWA, H. TOKIZAWA, A. KAWAMURA, S. Generating two dimensional ground reaction forces with a viscoelastic runner model. **Procedia Engineering**, London, v. 13, n. 1, p. 161-167, 2011.

ZADPOOR, A. A. NIKOOYAN, A. A. Modeling muscle activity to study the effects of footwear on the impact forces and vibrations of the human body during running. **Journal of Biomechanics**, New York, v. 43, n. 2, p. 186-193, 2010.

ZADPOOR, A. A. NIKOOYAN, A. A. ARSHI, A. R. A model-based parametric study of impact force during running. **Journal of biomechanics**, New York, v. 40, n. 9, p. 2012-2021, 2007.

ZENER, C. **Elasticity and anelasticity of metals**. Chicago: University of Chicago press, 1948.

ZILL, D. G. **Engineering Mathematics**. Burlington: Jones & Barlett Pub, 2009.

APPENDIX A – Three-DOF model fit to experimental dataset

In this appendix, the three-DOF LPM with the Zener ground contact model is optimized to fit a ground reaction force dataset to show that the optimizing the model's parameters does not lead to a good GRF fit for the model.

The dataset used for fit is the openly available data provided by Tongen and Wunderlich (2010), with respect to a 77.51 kg male running. The data consists of the average of 10 trials with respect to the measured GRF in *z* axis.

The three-DOF model configuration was presented in Fig. 24. The pattern search algorithm was used in Matlab to optimize k_0, k_{01}, k_1, c_0 and c_1 with a previously defined range. The initial conditions used were defined by Zadpoor *et al*. (2007). The m_1 / m_{total} used is of 0.20 (20%) which represents the best fits obtained and are in agreement with the ratio used by Derrick *et al*. (2000). The mass m_0 is 0.01 kg (needs to be small). The initial displacements are all zero. Table 21 shows the defined parameters and the optimized ones.

Table 21 – three-DOF model parameters and initial conditions including optimized parameters.

masses [kg]	springs [kN/m]	dampers [Ns/m]	touchdown velocities [m/s]
m_0 = 0.010	k_0 = 13.816	c_0 = 83.125	$v_0(0)$ = 0.96
m_1 = 15.502	k_{01} = 42.188	c_1 = 89.625	$v_1(0)$ = 0.96
m_3 = 61.998	k_1 = 29.268		$v_3(0)$ = 2.00

Source: elaborated by the author.

The comparison between the GRF dataset and the fitted model response GRF is shown in Fig. 33 bellow.

Figure 33 - best fit obtained through optimization of the three-DOF mass spring damper model ( )with respect to Tongen and Wunderlich GRF dataset ( ).

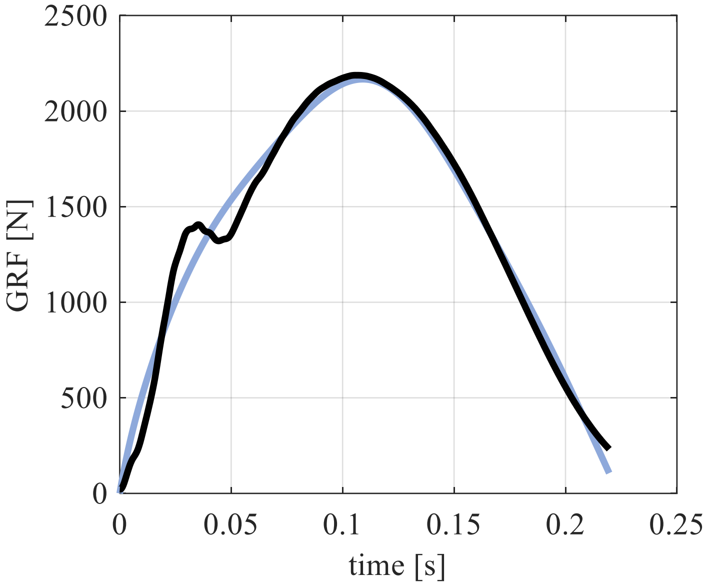

Source: elaborated by the author.

It is clear that the overall fit to the data is good, but the model fails to capture the impact peak (first peak) and the transition to the active peak (second peak), which consists of the deceleration of the lower body mass and acceleration of the upper body mass. Different LPMs were tested to fit different GRF datasets, but similar problems were encountered in their fits.

APPENDIX B – Expanded modal matrices

In this appendix, the damped modal matrices from five-DOF and three-DOF models are presented. The matrices are shown here due to their space requirements and have relevant information about the modes. The damped modal matrix from the five-DOF model modal analysis is shown next.

$$\mathbf{\Phi}_{5D,d}=\begin{bmatrix} 0.0006+j0.0014 & 0.0006-j0.0014 & -0.1447+j0.0754 & -0.1447-j0.0754 & 0.0700-j0.9299 & 0.0700+j0.9299 & -1 & 0.3717 & 0.0148 & -0.0009 \\ 0.03615-j0.0284 & 0.03615+j0.0284 & 0.3724+j0.3126 & 0.3724-j0.3126 & -0.6299+j0.0442 & -0.6299-j0.0442 & 0.0016 & -0.3650 & -0.1410 & 0.0209 \\ -0.0109-j0.4162 & -0.0109+j0.4162 & 0.6540-j0.3460 & 0.6540+j0.3460 & 0.2562+j0.2252 & 0.2562-j0.2252 & 0 & 0.3284 & 1 & -1 \\ 0.2291-j0.5667 & 0.2291+j0.5667 & 0.0287-j0.0011 & 0.0287+j0.0011 & 0.0341+j0.0837 & 0.0341-j0.0837 & 0 & -1 & -0.1364 & -0.7430 \\ 0.2616-j0.7384 & 0.2616+j0.7384 & -0.0061-j0.0107 & -0.0061+j0.0107 & 0.0027-j0.0130 & 0.0027+j0.0130 & 0 & 0.2394 & 0.2321 & 0.0594 \\ 0.0001-j0.00008 & 0.0001j.00008 & 0.0014+j0.0007 & 0.0014-j0.0007 & -0.0020+j0.0027 & -0.0020-j0.0027 & 0.00002 & -0.0021 & -0.0004 & 0.00006 \\ -0.0033-j0.0022 & -0.0033+j0.0022 & 0.0002-j0.0048 & 0.0002+j0.0048 & 0.0020+j0.0011 & 0.0020-j0.0011 & 0 & 0.0020 & 0.0042 & -0.0014 \\ -0.0342+j0.0119 & -0.0342-j0.0119 & -0.0066-j0.0030 & -0.0066+j0.0030 & -0.0004-j0.0012 & -0.0004+j0.0012 & 0 & -0.0018 & -0.0296 & 0.0658 \\ -0.0530-j0.0040 & -0.0530+j0.0040 & -0.0002-j0.0002 & -0.0002+j0.0002 & 0.00005-j0.0003 & 0.00005+j0.0003 & 0 & 0.0056 & 0.0040 & 0.0489 \\ -0.0681-j0.0021 & -0.0681+j0.0021 & -0.00005+j0.0001 & -0.00005-j0.0001 & -0.00003+j0.00003 & -0.00003-j0.00003 & 0 & -0.0013 & -0.0069 & -0.0039 \end{bmatrix} \quad (127)$$

The damped modal matrix obtained in the modal analysis of the three-DOF model is presented below.

$$\mathbf{\Phi}_{3D,d}=\begin{bmatrix} 0.0049-j0.0165 & 0.0049+j0.0165 & 0.1128+j0.8872 & 0.1128-j0.8872 & 1 & 0.0887 \\ -0.2813-j0.0203 & -0.2813+j0.0203 & 0.8690-j0.0011 & 0.8690+j0.0011 & -0.0006 & -1 \\ -0.6711-j0.3289 & -0.6711+j0.3289 & -0.0251-j0.0190 & -0.0251+i0.0190 & 0 & -0.3187 \\ -0.0014-j0.00002 & -0.0014+j0.00002 & 0.0038-j0.0045 & 0.0038+j0.0045 & 0 & -0.0055 \\ 0.0048+j0.0230 & 0.0048-j0.0230 & -0.0038-j0.0042 & -0.0038+j0.0042 & 0 & 0.0616 \\ -0.0111+j0.0613 & -0.0111-j0.0613 & 0.00002+j0.0002 & 0.00002-j0.0002 & 0 & 0.0196 \end{bmatrix} \quad (128)$$